POINT DEFECTS IN LITHIUM GALLATE AND GALLIUM OXIDE

DISSERTATION

Christopher A. Lenyk, Lt Col, USAF

AFIT-ENP-DS-19-S-023

DEPARTMENT OF THE AIR FORCE
AIR UNIVERSITY

AIR FORCE INSTITUTE OF TECHNOLOGY

Wright-Patterson Air Force Base, Ohio

AFIT-ENP-DS-19-S-023

POINT DEFECTS IN LITHIUM GALLATE AND GALLIUM OXIDE

DISSERTATION

Presented to the Faculty

Graduate School of Engineering and Management

Air Force Institute of Technology

Air University

Air Education and Training Command

in Partial Fulfillment of the Requirements for the

Degree of Doctor of Philosophy in Nuclear Engineering

Christopher A. Lenyk, B.S., M.S.

Lt Col, USAF

AFIT-ENP-DS-19-S-023

POINT DEFECTS IN LITHIUM GALLATE AND GALLIUM OXIDE

DISSERTATION

Christopher A. Lenyk, B.S., M.S.
Lt Col, USAF

Committee Membership:

Nancy C. Giles, PhD
Chair

Maj Nicholas Herr, PhD
Member

Maj Tod Laurvick, PhD
Member

John W. McClory, PhD
Member

ADEDEJI B. BADIRU, PhD
Dean, Graduate School of Engineering and Management

AFIT-ENP-DS-19-S-023

Abstract

Electron paramagnetic resonance (EPR), Fourier-Transform Infrared spectroscopy (FTIR), photoluminescence (PL), thermoluminescence (TL), and wavelength-dependent TL are used to identify and characterize point defects in lithium gallate and β-gallium oxide doped with Mg and Fe acceptor impurities single crystals. EPR investigations of $LiGaO_2$ identify fundamental intrinsic cation defects lithium (V_{Li}^{-}) and gallium (V_{Ga}^{2-}) vacancies. The defects' principle g values are found through angular dependence studies and atomic-scale models for these new defects are proposed. Thermoluminescence measurements estimate the activation energy of lithium vacancies at $E_a = 1.05$ eV and gallium vacancies at $E_a > 2$ eV below the conduction band minimum.

Mg and Fe doped β-Ga_2O_3 crystals are investigated with EPR and FTIR and concentrations of Ir^{4+} ions greater than 1×10^{18} cm^3 are observed. The source of the unintentional deep iridium donors is the crucible used to grow the crystal. In the Mg-doped crystals, the Ir^{4+} ions provide compensation for the singly ionized Mg acceptors contributing to the difficulties in producing p-type behavior in bulk single crystals. A large spin-orbit coupling causes Ir^{4+} ions to have a low-spin ($5d^5$, S = 1/2) ground state. The Ir^{4+} ions have an infrared absorption band representing a $d - d$ transition within the t_{2g} orbitals.

Using these same techniques the $Fe^{2+/3+}$ level in Fe-doped β-Ga_2O_3 crystals is determined. With these noncontact spectroscopy methods, a value of 0.83 ± 0.04 eV below the conduction band is obtained for this level. These results clearly establish that the E2 deep level observed in DLTS experiments is due to the thermal release of electrons from Fe^{2+} ions.

Dedicated to my loving and unbelievably patient wife. Thank you for being by my side all these years.

Acknowledgements

I wish to thank my faculty advisor, Dr. Nancy C. Giles, for her advice, encouragement, willingness to take on another student, and the opportunity to be a part of this exciting and fundamental field of research. I would like to thank Dr. Larry Halliburton for the countless hours spent coaching me through the numerous experimental setups, explanations on the nuances of the physics, and for his insistence on critical thinking and always reminding me to be aware of any assumptions made during the exploration process.

Also, I want to thank the members of my committee Majors Nicholas Herr and Tod Laurvick, and Dr. John McClory for agreeing to be part of the endeavor. Last, I want to thank Capt Elizabeth Scherrer for her support on EasySpin codes and posing many questions that made me rethink the way I was approaching my own data sets.

Christopher A. Lenyk

Table of Contents

Page

Page

List of Figures

List of Tables

List of Abbreviations

Abbreviation		Page
PMT	photomultiplier tube	58
ND	neutral density	59
CCD	charge-coupled device	60
TSC	thermally stimulated current	77
STE	self-trapped excitons	81

POINT DEFECTS IN LITHIUM GALLATE AND GALLIUM OXIDE

1. Introduction

1.1 Overview and Motivation

The unique constraints of device operation in the military domain subjects electronic and optical components to environmental extremes. In current and future conflicts, the rise of directed-energy weapons (DEW), the continued threat of operating in areas after detonation of a nuclear weapon, and the heavy reliance on space-based platforms for power projection and routine military operations, indicates that commercial and civilian device characteristics involving as-grown charge states of defects may be seriously degraded or otherwise affected by radiation resulting in adverse performance. There is considerable interest, therefore, in understanding the fundamental physics of point defects and radiation effects in materials that may be used in future electronic systems.

Every material, regardless of growth or manufacturing technique, contains intrinsic, extrinsic, or both types of defects. Small regions within a single crystal may be free of defects, but configurational entropy favors that larger crystals, or even thin films, incorporate a certain concentration of defects to lower the free energy [1]. Impurities are often introduced into a material to tailor it for specific applications. Doping for electronic applications is necessary to create defect states that are close to the respective valence and conduction bands facilitating mobile charge.

Since the presence of defects in a material is unavoidable, their effects on the materials properties must be identified and characterized by careful and accurate

experimental investigation. Point defects in particular play a critical role in virtually all diffusion processes. The presence of defects can result in device degradation in routine commercial or military use, while the absence of certain defects can also inhibit performance. Compensation by intrinsic point defects can limit doping levels. Defects within the band-gap acting as recombination centers can impede carrier collection, or light emission for specific applications. Conversely, defects can also be advantageous such as when acting as a luminescent center at a specific wavelength in wide-band-gap materials, or as an isolated spin center creating an artificial atom that serves as a qubit for quantum information systems [2].

The work covered in this disseration is focused on two materials:$LiGaO_2$ and β-Ga_2O_3. $LiGaO_2$ is an insulating material, typically used as a substrate for growing thin films, but also has potential applications as a semiconductor or a radiation dosimeter. Beta-Ga_2O_3 is a wide band gap semiconductor of increasing interest for power electronics and optical applications. Performance and suitability of Ga_2O_3 for various applications is heavily dependent on the types and concentrations of point defects within a single crystal. For most applications, it is desirable for the material to be capable of being grown with either p- or n-type behavior.

1.2 Previous Research on Ga_2O_3

Recent developments and research into wide bandgap semiconductors have brought considerable interest to β-Ga_2O_3 and its potential for applications in power electronics and solar-blind detectors. Beta-Ga_2O_3 is low symmetry as the crystal is a monoclinic structure and the space group is C2/m. At 273° K the lattice constants are a = 12.214 Å, b = 3.0371 Å, c = 5.7981 Å, and $\beta = 103.83°$ [3,4]. These constants follow the usual convention where the crystallographic b axis is perpendicular to the crystal's mirror plane. This structure contains two inequivalent gallium sites and three

inequivalent oxygen sites in the crystal for this complex binary crystal. This creates a structure where the Ga(I) ions have four oxygen neighbors and the Ga(II) ions have six oxygen neighbors, and then the O(I) and O(II) ions have three gallium neighbors whereas the O(III) ions have four gallium neighbors. A "ball-and-stick" model of the β-Ga_2O_3 crystal is shown in Figure 1.1. Owing to the low symmetry of the crystal, it is convenient to define another set of axes, perpendicular to each of the crystal axes assisting in acquiring and presenting EPR spectra and angular dependence data. The a^* and c^* directions are introduced and defined where a^* is perpendicular to the crystallographic b and c and c^* is perpendicular to the crystallographic a and b. With a

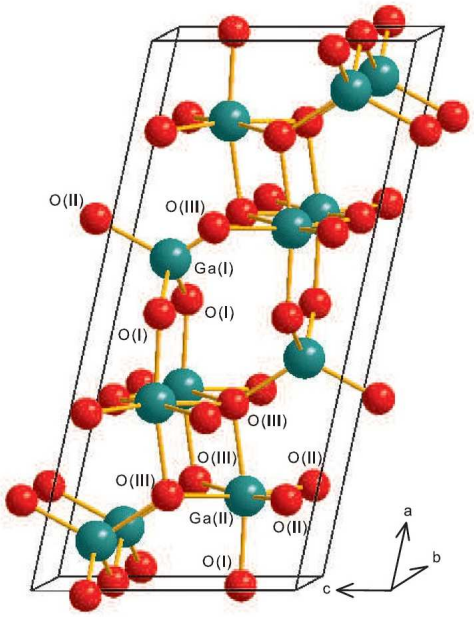

Figure 1.1. Ball-and-stick model of the crystal structure for β-Ga_2O_3 . Gallium ions are shown in green and the oxygen ions in red. There are two inequivalent gallium sites, Ga(I) and Ga(II), and three inequivalent oxygen sites labeled O(I), O(II), and O(III). The Ga(I) sites are tetrahedral (with four oxygen neighbors) and the Ga(II) sites are octahedral (with six oxygen neighbors). Reprinted with permission from [5].

large bandgap of 4.9 eV and a high melting point of 1800°C, β-Ga_2O_3 has potential in power electronics applications. The primary shallow donor in Ga_2O_3 has been

identified as Si^{3+} sitting on Ga^{3+} sites through studies on unitentionally doped samples [6–10]. In fully activated crystals having large concentrations of Si, the shallow donor has been shown to have an activation energy slightly below 20 meV [7, 8, 10]. Studies are currently underway to identify a suitable shallow acceptor for device applications. At present, there is interest in the effects of doping with Mg, but this may be expanded in the future to Li, Cu, and Zn.

While oxygen vacancies are now considered to be a deep donor, holes trapped on oxygen ions adjacent to Ga vacancies or on Mg ions at Ga sites are shallower [5,11,12]. Additionally, at low temperatures, holes can become self-trapped on oxygen ions in an otherwise unperturbed area of the crystal lattice [13]. Ga vacancies were recently identified through their production via neutron irradiation at the Ohio State University nuclear reactor of an unintentionally doped (UID) sample [5]. Irradiation lowered the Fermi level of the crystal through the production of a significant number of Ga vacancies which were then visible during room temperature EPR, shown in Figure 1.2. This EPR spectrum shows a doubly ionized gallium vacancy from the neutron irradiation. A single unpaired spin ($S = \frac{1}{2}$) interacts with two adjacent Ga sites. The partially resolved hyperfine arises from the two isotopes of gallium, ^{69}Ga and ^{71}Ga with nuclear spin of $I = \frac{3}{2}$, and in natural abundances of 60.1% and 39.9%, and magnetic moments of $^{69}\mu = +2.0166\beta_n$ and $^{71}\mu = +2.5623\beta_n$. The resolved hyperfine spectrum shown results from three different combinations of two Ga isotopes (i) two ^{69}Ga nuclei, (ii) one ^{69}Ga and one ^{71}Ga nuclei, and (iii) two ^{71}Ga nuclei, in relative abundances of 36.1%, 48%, and 15.9%. If the unpaired spin interacts equally with either two isotopes of ^{69}Ga or ^{71}Ga, a spectrum of seven lines arises (relative intensities of 1:2:3:4:3:2:1), whereas if the spin interacts with ^{69}Ga and ^{71}Ga at a gallium vacancy, a spectrum of 16 equally intense lines is produced.

The role and EPR spectrum of neutral Mg acceptors has also been studied. Mg-

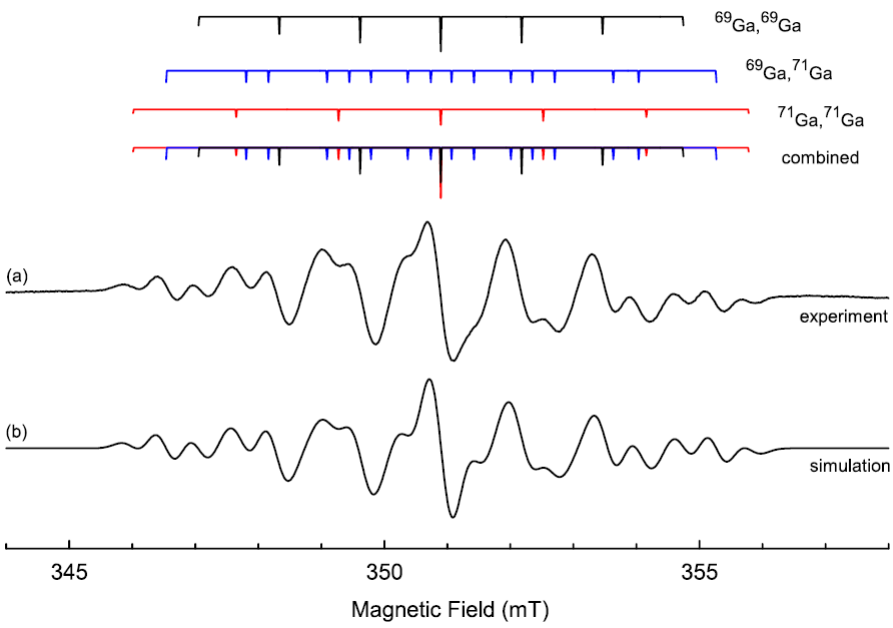

Figure 1.2. **(a) Doubly ionized gallium vacancy β-Ga_2O_3 EPR spectrum with $S = \frac{1}{2}$. This spectrum was taken at room temperature with the magnetic field along the a direction in the crystal, and a microwave frequency of 9.4 GHz. (b) Simulation of the gallium vacancy EPR spectrum using the Bruker SimFonia program. Reprinted with permission from [5].**

doped β-Ga_2O_3 was irradiated at 77 K with 60 kV x-rays and transferred to the EPR spectrometer without significant warming [12]. The x-rays generate large numbers of electrons and holes in the conduction and valence bands. While many of these electrons and holes combine immediately, Mg trapped appreciable concentrations of holes, while the UID of Fe^{3+} and Cr^{3+} trapped electrons. A spectrum of the Mg acceptor is shown in Figure 1.3. A comprehensive analysis of the neutral Mg acceptor is detailed in Kananen *et al*. [12]. An important finding was that the hole trapped on the Mg becomes thermally unstable between 250 K and 300 K. The prevailing explanation is that around this temperature, the holes "move" away from the Mg through the small polaron-hopping process; however, present research results cannot rule out that another unidentified defect releases an electron that recombines on a neutral Mg site.

Another important instrinsic characteristic of β-Ga_2O_3 is the experimental discovery of self-trapped holes (STH) by Kananen *et al* [13]. The details of STH are discussed in their work, but the most relevant to current work is the thermal stability of STH. Through a series of isochronal anneals, the thermal stability of the STH was determined to be between 80-110 K. In their work, STH are observed by using a sample with a sufficiently low Fermi level, and irradiating with x-rays at 77 K and transferring the sample to the EPR spectrometer without significant warming. Additionally, it was determined that STH do not decay through the migration of an electron through the lattice, but rather through the hole becoming unstable in the temperature range and traveling through the lattice by hopping from oxygen to oxygen. This indicates that STH are a fundamental characteristic of the material and represent an intrinsic energy barrier (i.e., an energy penalty that must be overcome each time a hole attempts to move from one oxygen to another) to effective hole conduction. STHs do not dependent on the specific ions trapping electrons, and

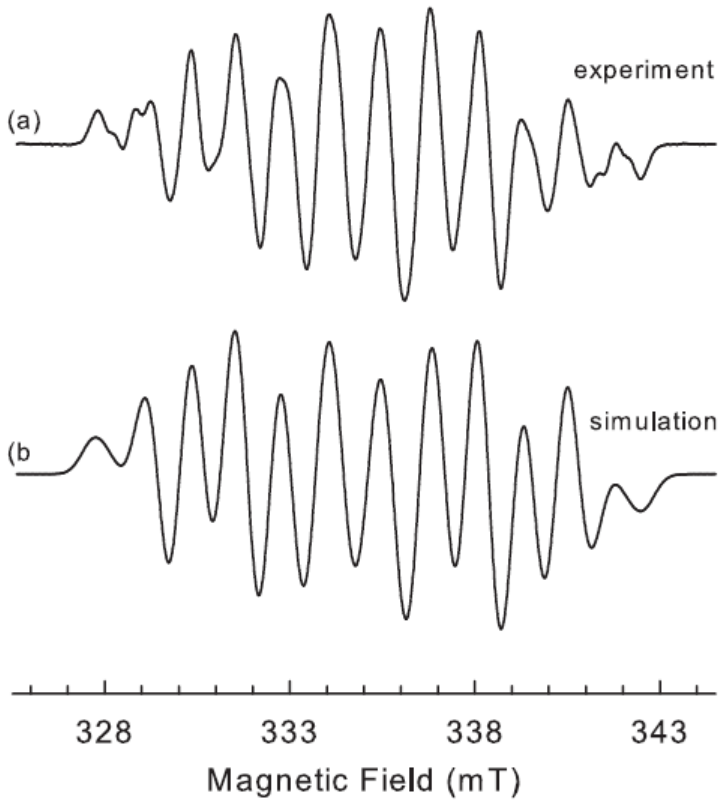

Figure 1.3. (a) EPR spectrum from the $S = \frac{1}{2}$ neutral magnesium acceptor in Mg-doped β-Ga_2O_3. The magnetic field was along the crystallographic a direction with a microwave frequency of 9.3979 GHz. (b) EPR simulated spectrum produced using EasySpin. Reprinted with permssion from [12].

therefore are a serious impediment to developing usable p-type material.

1.3 Previous Research on $LiGaO_2$

In contrast in β-Ga_2O_3, very few studies have been conducted on the fundamental point defects of $LiGaO_2$. $LiGaO_2$ is a wide bandgap semiconductor with a direct bandgap of 5.3 eV, a melting point of 1585°C and a near wurtzite-like crystal structure [14,15]. $LiGaO_2$ has a higher symmetry than β-Ga_2O_3; the crystal has an orthorhomic structure and the space group is $Pna2_1$. At 273 K the lattice constants are a = 5.402 Å, b = 6.372 Å, c = 5.007 Å. A schematic "ball-and-stick" model is shown in Chapter 4 in Figure 4.1.

The $LiGaO_2$ structure is very similar to GaN, with each anion having four cation neighbors (three are located in the basal plane and one along the c axis). In the ideal $LiGaO_2$ crystal structure, each oxygen ion has two gallium and two lithium neighbors, and every gallium ion and lithium ion has four oxygen neighbors. All the Li^+ sites are equivalent and all the Ga^{3+} sites are equivalent. However, the oxygen ions have two slightly inequivalent sites crystallographically, which are label O_I and O_{II}. The oxygen sites are distinguishable by their c axis nearest neighbor, with the O_I sites having an adjacent lithium ion, and the O_{II} having an adjacent gallium ion.

$LiGaO_2$ has a variety of applications. Band-gap engineering can be accomplished by alloying $LiGaO_2$ with ZnO (ZnO has a direct bandgap of 3.37 eV) [15–18]. While yet to be identified, suitable donor/acceptor identification for $LiGaO_2 - ZnO$ materials opens fabrication of photodetectors and laser diodes capable of operating across most of the ultraviolet (UV). Primarily, $LiGaO_2$ has been used as a lattice-matched substrate for GaN and ZnO thin film growths [19–21]. Recently, Cu-doped $LiGaO_2$ has been shown to have immediate application as a radiation detection material and phosphor. Cu-doped $LiGaO_2$ was identified to have well suited characteristics for

optically stimulated luminescence (OSL) and TL dosimetry [14].

1.4 Organization of the Dissertation

Chapters 2 and 3 provide an overview of the experimental principles and instrument setup starting with crystal field theory which treats the material as an ionic solid. The merits and limits of this treatment are discussed, as well as its application to the experimental techniques of electron paramagnetic resonance and optical absorption. The complete expression for the spin Hamiltonian is described and the relevance of each term to unpaired spin for measurements is detailed. A brief overview of optical absorption is presented for $d - d$ transitions. Chapter 2 concludes following discussions on the various kinetic order models for thermoluminescence. Each instrument used in the collection of experimental data and its operation is described in chapter 3.

Chapters 4 through 6 are prepared as publishable work according the standards of the Journal of Applied Physics in accordance with the Style Guide for AFIT Dissertations, Thesis, and Graduate Research Papers. Chapters 4 and 5 are already published in the Journal of Applied Physics. Chapter 4 is the first published work identifying and characterizing intrinsic cation vacancies in $LiGaO_2$ and represents the classic description of solids provided by crystal field theory. Chapter 5 identifies the unintentional incorporation of iridium ions in large concentrations due to crystal growth in iridium crucibles. This defect is electrically active and acts as a deep donor in β-Ga_2O_3. Its spin configuration, which leaves a single unpaired electron in the $5d$ orbital with a large degree of covalency, represents the limitations of crystal field theory. Chapter 6 is a drafted submission for Journal of Applied Physics from work presented as a poster at the Materials Research Society's 61st Electronic Materials Conference. This chapter covers the implementation of a novel non-contact method

for estimating the activation energy of deep acceptors in β-Ga_2O_3 using general order kinetics from thermal decay measurements.

The written document concludes with a summary of research results and suggestions on future experiments for β-Ga_2O_3 and $LiGaO_2$. The results and the materials investigated are discussed in the broader context of several emerging materials for laser applications at wavelengths greater than 6 microns.

1.5 Research Support, Interest, and Limits

Research on Ga_2O_3 is supported by the Air Force Office of Scientific Research (AFOSR) with samples supplied by Synoptics in Charlotte, NC, and Kyma Technologies in Raleigh, NC, and additional support from the Air Force Research Laboratory (AFRL). Single crystals of Ga_2O_3, both UID and doped, are also grown at AFRL. $LiGaO_2$ was purchased from the commercial third party vendor MTI Corporation.

The primary interest in Ga_2O_3 is for power electronics. Ga_2O_3 is a wide bandgap semiconductor with a direct bandgap of 4.85 eV. Single crystals of β-Ga_2O_3 are primarily n-type due to the presence of Si^{3+}. Finding a suitable shallow acceptor will allow device construction from a single material. The large bandgap of Ga_2O_3 has also generated interest for ultraviolet applications including lasers and detection.

$LiGaO_2$ is a wide bandgap semiconductor with a direct bandgap of 5.3 eV. Few fundamental point defect studies have been done on $LiGaO_2$. Recent literature has focused on alloying $LiGaO_2$ with ZnO for bandgap engineering [15–17], and other studies have highlighted dosimetry applications through Cu doping [14]. With two crystallographically different cation sites (one monovalent and the other trivalent), $LiGaO_2$ has a large range of doping possibilities for applications.

2. Experimental Principles

This chapter describes several of the principles of the instrumentation and results from investigations of the radiation effects in various materials. The chapter begins with a discussion of the ionic treatment of solids called crystal field theory. This theory lays the foundation for describing the orbital splitting of d electrons in transition metal ions. The merits of the theory also provide the framework for understanding subsequent sections on the instrument principles of electron paramagnetic resonance, optical spectroscopy, and thermoluminscence. The chapter concludes with a brief discussion of a special case for a Ir^{+4} defect.

2.1 Crystal Field Theory

A pursuit of the description of the bonding in solids has led to several approaches over the past century. Developed by Bethe and Van Vleck [22–25], crystal field theory (CFT) was developed alongside Pauling's valence bond (VB) theory [26]. Both CFT and VB are considered specialized cases of the more general molecular orbital (MO) theory. CFT's foundation is based on arguments presented in the more restrictive ionic model [27]. The theory is advantageous in that it provides a relatively simple model describing the coordinate chemistry. It also successfully explains the origins of absorption spectra in the visible and related color regions, and many observed optical and electrical properties, and electron paramagnetic resonance spectra [27, 28]. The energetics and predictions from CFT are similar to the more complex MO theory, and the symmetry arguments for both CFT and MO are identical. For these reasons, CFT is used to describe the local environment of d-shell impurities (i.e., transition metals) in this work [22].

Transition-metal ions account for approximately one-third of all the known el-

ements, spanning 10 of the 18 groups and 4 of the 7 periods. In total, transition metals make up 38 elements when transactinides are included, beginning with scandium and ending with copernicium [22].[1] This broad range of group and periodicity makes transition metal ions important in materials development either as a primary constituent or as an extrinsic defect. While there is no unique way to represent

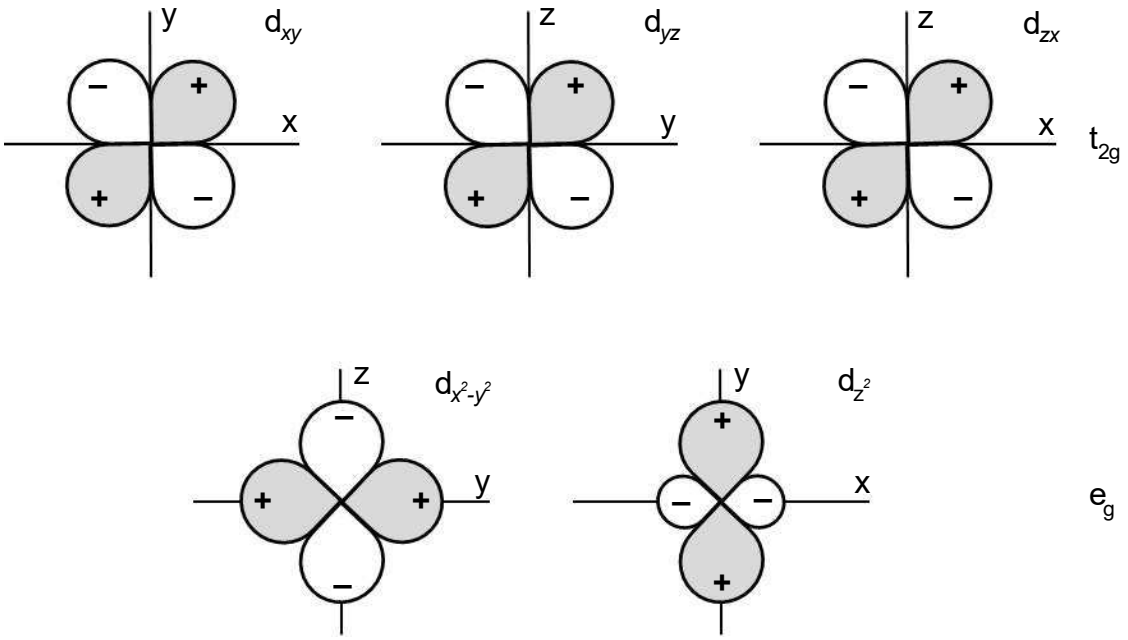

Figure 2.1. Illustration of the d orbitals spatial arrangement. The splitting of the orbitals into the t_{2g} and e_g levels results from a transition metal ion in the presence of an external electric field.

d orbitals, a common representation is shown in Figure 2.1. In total, there are six ground state wave functions that can comprise the typical four-lobed forms; however, physical reality dictates there are only five d orbitals. Two of the orbitals are linear combinations of the others. Common convention from group theory distinguishes these ground states into two groups referred to as the triplet and doublet states, t_{2g} and e_g respectively [22, 28].

The splitting of the five orbitals in an octahedral environment also modifies the

[1]The total number of transition metal ions can vary from 38 to 40 depending on the inclusion of lanthanum and actinium.

bonding with the surrounding ligand ions. A single electron in the triplet state ($t_{2g} \rightarrow d\epsilon$) partakes in the lower energy π-bonding, and in the doublet state ($e_g \rightarrow d\gamma$) higher energy σ-bonding. The nomenclature of $d\epsilon$ and $d\gamma$ refers to an electron purely in the d state, but the augmented states formed through the admixing of ligand ion orbitals retain the more general notation and classification of t_{2g} and e_g [29].

A strict view of CFT assumes a purely ionic interaction between the metal ion and surrounding ligands. In an isolated, gaseous environment, the five d orbitals are energetically degenerate. In highly symmetric crystal geometries, such as cubic materials, or lower symmetry materials having differing crystal sites such as tetrahedral or octahedral, spherical symmetry is broken by partially lifting the degeneracy of levels. An octahedral local environment with six filled ligands on the axes of the system will create two different interactions between the metal ion and ligands. Ligand ions will interact strongly with the e_g orbitals as they approach on the x, y, and z axes raising the energy of the d_{z^2} and $d_{x^2-y^2}$ orbitals [22]. Since this interaction is directed along the bond axis, higher energy σ-bonding occurs with the wave function symmetric about the bonding axis and the orbitals typically of $s - p$ hybridization. The t_{2g} orbitals (d_{xy}, d_{yz}, d_{xz}) are repelled to some extent being directed normal to the approaching ligand bond axis and lowering their overall energy through π-bonding [29]. The separation of the orbitals from the barycenter,[2] called the crystal or ligand field splitting, is represented in energy by the quantity 10Dq = Δ, where D is the magnitude of the splitting and q is the charge of an electron.[3] Due to conservation of energy, the e_g orbitals are raised 6 Dq above the barycenter and the t_{2g} lowered by 4Dq [22].

[2]The barycenter is likened to a center of gravity, and represents an average energy about which the orbitals maintain degeneracy

[3]Values of Δ are often measured through optical absorption techniques and are represented in wavenumbers [30].

2.1.1 The weak field approximation

As electrons fill their respective orbits, the energy relative to the barycenter of the unperturbed d orbitals is known as the crystal field stabilization energy (CFSE) [22]. When the ligand field is not strong, the influence of its field can be taken as a perturbation of the atomic terms, and the atomic terms are classified according to quantum number and angular momentum L [28]. Electrons typically fill the d shells following Hund's rule assuming the lowest possible energy configuration, unpaired and entering different degenerate orbitals. The t_{2g} level fills to the d^3 configuration without pairing. However, two possibilities exist for the d^4 configuration: one with electron pairing and one without. In the weak field approximation, the energy required for pairing electrons in a single orbital is greater than the crystal field splitting, as shown in Figure 2.2a. The electron is placed in the e_g orbital and the electronic configuration is referred to as a "high spin" system. The CFSE can be calculated if the crystal field splitting is known by,

$$CFSE = \left(n_{t_{2g}} \times -\frac{2}{5}\Delta\right) + \left(n_{e_g} \times \frac{3}{5}\Delta\right) + \Pi \tag{2.1}$$

where $\mathrm{n_{t_{2g}}}$ and $\mathrm{n_{e_g}}$ are the number of electrons in their respective orbits and Π (sometimes shown as P) is the pairing energy; for the weak field case $\Pi = 0$. The CFSE is zero in d^5 and d^{10} configurations where the energy of two electrons in e_g level exactly balances the energy of the three electrons in t_{2g} level, indicating no further stabilization can occur from application of an external field [22]. Any ground state configuration can be constructed by applying two rules: 1) minimize the crystal field stabilization energy, and 2) apply the restrictions imposed by the exclusion principle. Spin values for a "high spin" have a range of $\frac{1}{2} \leq \mathrm{S} \leq \frac{5}{2}$ and have electronic configurations as shown in Figure 2.3a [22, 31]. The number of ways in which the

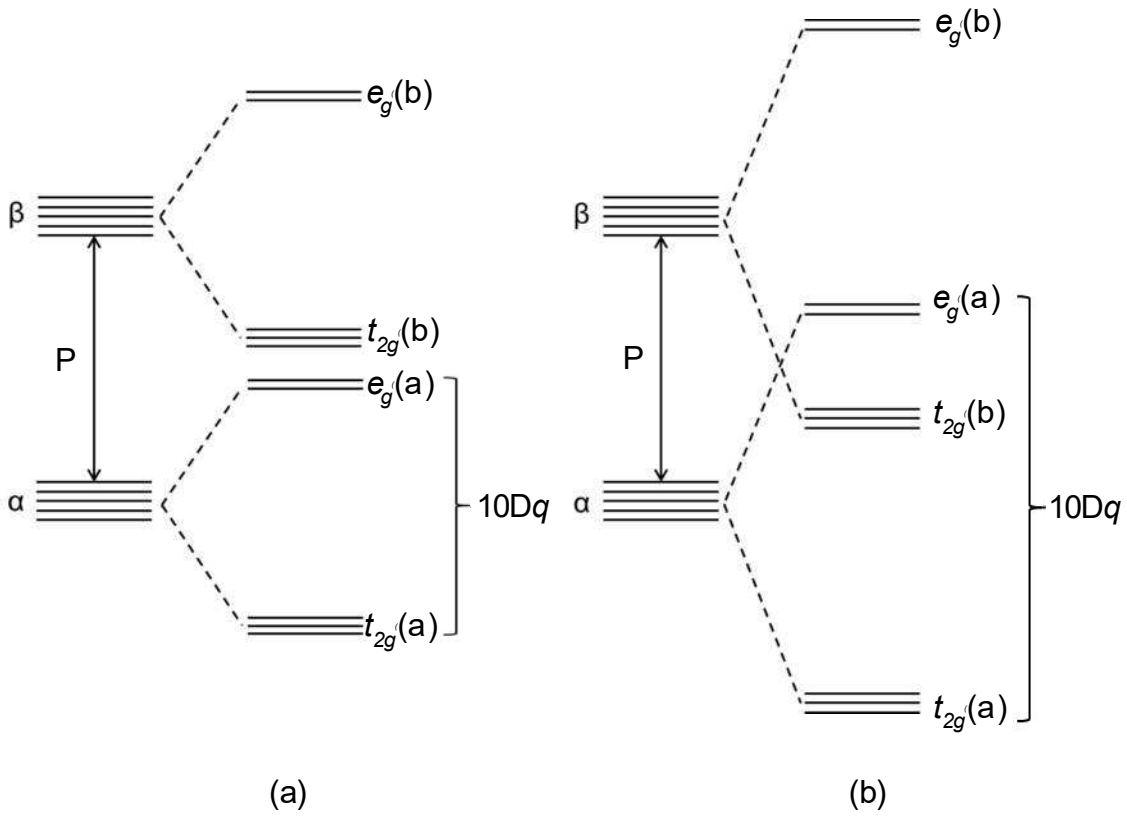

Figure 2.2. Comparison of the crystal field splittings for the a) strong field approximation and b) weak field approximation. The pairing energy, P, has the more formal mathematical notation, Π and the crystal field splitting, 10Dq = Δ. Each line represents the one electron wave function including spin denoted by α and β.

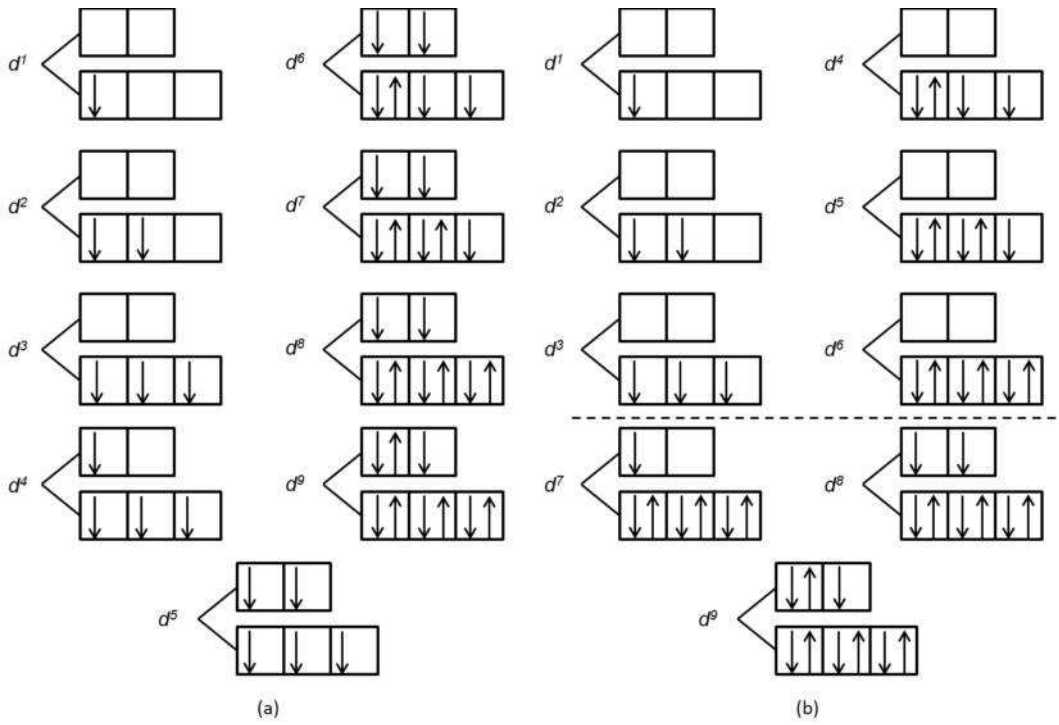

Figure 2.3. Construction of the ground states for d-configurations of a) high and b) low spin systems in an octahedral field. The S values and orbital multiplicity for individual ground states are given in Table 2.1. After Abragam and Bleaney [29].

electrons can be arranged in orbitals of the same degenerate energy for any ground state configuration is called the orbital multiplicity. Table 2.1 shows the relationship of electronic ground state configuration, spin values, and orbital multiplicity.

Table 2.1. Ground state construction in an octahedral field of the d-configurations for high and low spin systems. High spin configurations are suitable for the weak and intermediate crystal field approximation when spin coupling is stronger than the crystal field energy. The low spin configuration is appropriate in the strong field approach when the spin coupling is weaker than the crystal field energy.

High Spin			Low Spin		
	S	orbital multiplicity		S	orbital multiplicity
d^1	$\frac{1}{2}$	triplet	d^1	$\frac{1}{2}$	triplet
d^2	1	triplet	d^2	1	triplet
d^3	$\frac{3}{2}$	singlet	d^3	$\frac{3}{2}$	singlet
d^4	2	doublet	d^4	1	triplet
d^5	$\frac{5}{2}$	singlet	d^5	$\frac{1}{2}$	triplet
d^6	2	triplet	d^6	0	singlet
d^7	$\frac{3}{2}$	triplet	d^7	$\frac{1}{2}$	doublet
d^8	1	singlet	d^8	1	singlet
d^9	$\frac{1}{2}$	doublet	d^9	$\frac{1}{2}$	doublet

2.1.2 The intermediate field approximation

In between the limiting cases of the strong and weak field approximations, the ligand field and the electron interactions must be considered simultaneously. The intermediate field conditions exist when the ligand field is larger than the spin-orbit coupling but remains smaller than the interelectron interactions. Relatively close energetic terms interact resulting in a divergence of the energy levels. This is called the nonintersection rule which states that terms of the same wave function symmetry do not intersect. The resultant splitting of energy levels, Δ, depends on both the

strength of the ligand field and the initial energy spacing of the atomic terms. Tanabe-Sugano diagrams detail the most complete description of the electronic structure and account for the ground state changes predicting the transition from low to high spin systems [27–29].

2.1.3 The strong field approximation

The strong field approximation occurs if the splitting of the d orbitals is large with respect to the pairing energy (i.e. $\Pi > \Delta$). In this case, the effect of the ligand field surpasses the electrostatic interaction between the electrons and the orbital coupling between electrons is broken, causing states with definitive total angular momentum quantum numbers to cease existing [28]. Electrons in the strong field case occupy the energetically lower t_{2g} orbitals, remaining unpaired up to d^3 illustrated in Figure 2.3b. The e_g level is strongly unfavorable for the fourth electron and rather than entering, the electron forms a pair in the t_{2g}. This increases the CFSE, Equation 2.1, over values seen in the weak field approximation. Electron pairing in the strong field case results in systems that are referred to as "low spin" having spin values ranging from $\frac{1}{2} \leq \mathrm{S} \leq \frac{3}{2}$. The complete filling of the d subshells for high and low spin systems is shown in Figure 2.3 [22, 31].

2.1.4 Pairing energies

Weak and strong field approaches are the main focus of this dissertation in Chapter 5 and are distinguished from each other based on the pairing energy which is composed of two terms. The inherent repulsion from placing two electrons in the same orbit is mostly constant for transition metal ions. Larger more diffuse orbits from the $5d$ configuration more readily accommodate two negative charge than the smaller $3d$ configuration, but the differences are small [22]. This important result from the elec-

trostatic repulsion is sometimes called the "nephelauxetic effect" (meaning clouding expanding) or an "orbital reduction factor", k, from the apparent expansion of the d orbitals. This effect is the natural result of lowering the effective charge for transition metal ions through partially covalent bonding from delocalization of the d electrons onto the surrounding ions [27, 29]. The loss of the exchange energy when electrons with parallel spins are forced to pair having antiparallel spins is the second factor. Pairing of the d^5 configuration results in the greatest loss of exchange energy.

Transition from a high to low spin complex is determined by the relative strength of Δ to Π. When $\Delta < \Pi$ the weak field approximation is appropriate, while for $\Delta > \Pi$ the strong field approximation can be used [22, 28]. On either side of the crossover point related by $\Delta = \Pi$, both species continue to exist in thermal equilibrium with distributions determined by Boltzmann statistics. This temperature dependence causes changes in the average magnetic susceptibility of the two species (high and low spin). This changing magnetic susceptibility has shown that an ion can have different spin complexes in the same material at different temperatures [22].

2.1.5 Factors affecting magnitude of Δ

There are four primary factors affecting the magnitude of the crystal field splitting. The oxidation state of the transition metal ion directly affects the magnitude of Δ. From the electrostatic model, increasing the charge on a metallic ion decreases its distance from the ligands drawing them closer and causing a greater perturbation of the d orbitals. The number and geometry of the ligands also affects the splitting. An octahedral field is approximately twice as strong as a tetrahedral field from the same transition metal ion and ligands. Reducing the number of ligands decreases the electrostatic field at the impurity ion. Additionally, the shift from octahedral to tetrahedral less efficiently directs the ligands towards to d orbitals, exerting less

influence on t_{2g} and e_g. An octahedral configuration exerts maximum influence on the e_g level and minimizes its influence on t_{2g} levels [22,28]. The nature of the surrounding ligands affects the splitting due to the extent of electron-electron repulsion in the ground or excited state. While the increasing field strength in a spectrochemical series provides some basis for increased splitting, the splitting of d orbitals is not purely ionic and cannot be simplified to point charges of ions or dipoles. This is shown by the fact that anionic ligands lie at the lower energy end of the spectrochemical series causing small effects, whereas a strictly ionic interpretation from electrostatics predicts anionic ligands to exert the largest effects. A final factor affecting the magnitude of splitting is the nature of the involved metallic ion. Within a transition series, there is little effect on the splitting. However, changes occur between congeners progressing from $3d \rightarrow 4d \rightarrow 5d$. The result of this is the second and third transition series are almost exclusively low spin compared to the first transition series containing both high and low spin complexes [22].

2.2 Electron Paramagnetic Resonance (EPR)

The wave particle duality of an electron allows application of the concepts of classical angular momentum that can be represented by the spin angular momentum operator $\hat{\mathbf{S}}$ [32]. In the classical analog, the angular momentum arises from the spin of a sphere about its central axis. However, the quantum mechanical interpretation differs because the electron can be treated as elementary point particle, a fermion, lacking an inherent internal structure. Spin of the electron is solely quantum mechanical in nature, and has a related spin-induced magnetic moment

$$\hat{\mu} = g\gamma\hat{\mathbf{S}} \tag{2.2}$$

where the proportionality constant $\gamma = q/2m$ is referred to as the gyromagnetic (or magnetogyric) ratio having units of $\mathrm{C\,kg^{-1}} = \mathrm{s^{-1}\,T^{-1}}$. While the gyromagnetic ratio converts angular momentum to magnetic moment, g is a dimensionless quantity, often called the Zeeman correction factor. A classical analog of the orbital magnetic point dipole is a circulating electrical current i in a magnetic field. The field produced by this circulating current is equivalent to the dipole. The two quantities are shown to be equivalent by pointing the magnetic dipole in the z direction, perpendicular to the xy plane of the circle with area A,

$$\mu_z = iA = \pm\frac{qv\pi r^2}{2\pi r} = \pm\frac{q}{2m}mvr = \frac{q}{2m}L_z \tag{2.3}$$

where L_z is the orbital angular momentum about the axis z of a particle with mass m and velocity v. The direction of rotation determines the choice of sign in equation 2.3. From quantum mechanics, free particles having orbital angular momenta that are integral multiples of $\hbar$ have an associated orbital magnetic moment $\beta = |q|\hbar/2m = |\gamma\hbar/g|$. In the case where the electron is free, $g = g_e = 2.0023193$. However, in the presence of an electric field, the values of g depend on the relative contributions of the orbital angular momentum $\mathbf{L}$ of the electron in its orbit about the nucleus and the total spin $\mathbf{S}$ of the electron's total angular momentum [31, 33].

When subjected to an external magnetic field, the electron can be treated as a magnetic dipole owing to its magnetic moment shown in Figure 2.4. Taking the magnetic field $\mathbf{B}$ to be in the z direction, the energy of this interaction is defined by a scalar product

$$E = -\mu^{\mathbf{T}} \cdot \mathbf{B} = -\mathbf{B}^{\mathbf{T}} \cdot \mu = -|\mu\mathbf{B}|\cos(\theta) \tag{2.4}$$

where θ is the angle between the μ and $\mathbf{B}$. Equation 2.4 contains an important result. When the magnetic field lies parallel to the unpaired electron's magnetic moment,

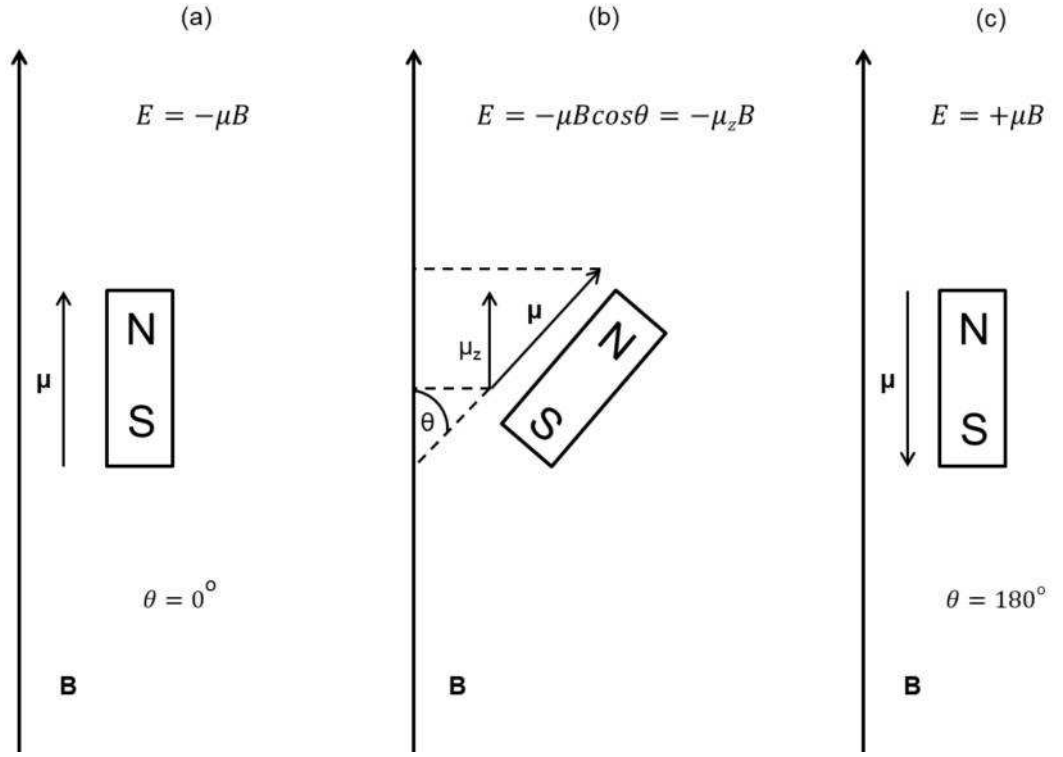

Figure 2.4. Energy of a classical magnetic dipole in a magnetic field as a function of the angles between the magnetic field and the axis of the dipole: (a) $\theta = 0$ is the minimum energy configuration; (b) an intermediate energy for an arbitrary angle of θ; and (c) $\theta = 180^\circ$ is the maximum energy configuration. After Weil [33].

the energy is minimized; but the energy is maximized when the field is antiparallel. For angles of θ between these extremes, U is at intermediate values. Applying U to a "spin only" system and substituting $\mu = -g\beta_e M_s$ results in

$$E = g\beta_e B M_s \tag{2.5}$$

where β_e is the Bohr magneton and $M_s = \pm\frac{1}{2}$ for a single unpaired electron, or $M_s = \pm S$ when S $> \frac{1}{2}$. The range of U values from different M_s values is sometimes referred to as the electronic Zeeman energies [33]. While classical analogues allow for a continuous range of energies, quantum mechanics dictates discrete energy values from the magnitude of the spin vector

$$\mathbf{S}^2 = \hbar^2 \left[S\left(S+1\right)\right] \tag{2.6}$$

The magnitude of the spin vector is shown in Figure 2.5. For a single unpaired

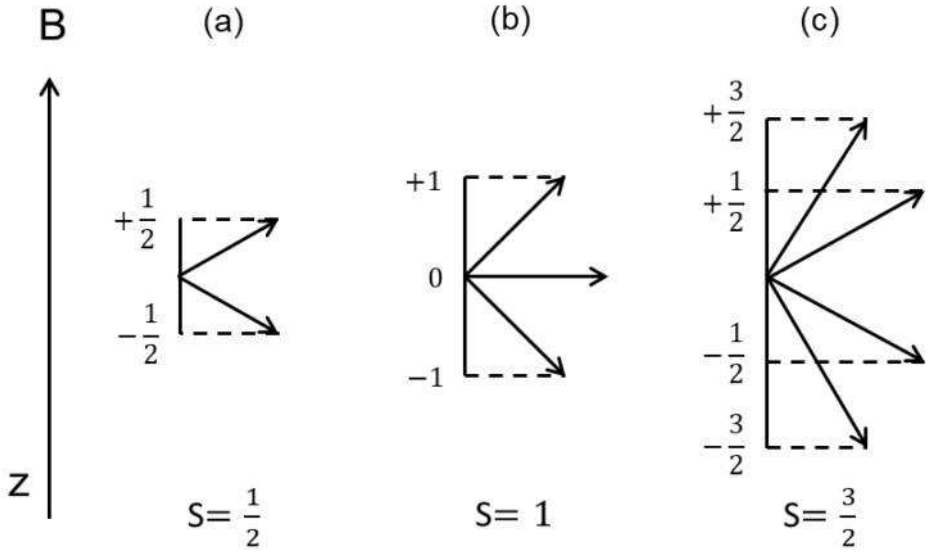

Figure 2.5. Allowed energy levels for Zeeman splitting with a static magnetic field parallel to the z-axis for (a) S = $\frac{1}{2}$, (b) S = 1, and (c) S = $\frac{3}{2}$. The quantity $\mathbf{S^2}$ is the magnitude squared of the spin vector. After Weil [33].

electron, values of $\mathrm{E} = \pm\frac{1}{2}g_e\beta_e B$ and an energy difference between the different M_s values can be represented as

$$\Delta E = E_{upper} - E_{lower} = \mu_B B = g\beta_e B \tag{2.7}$$

and is shown in Figure 2.6.

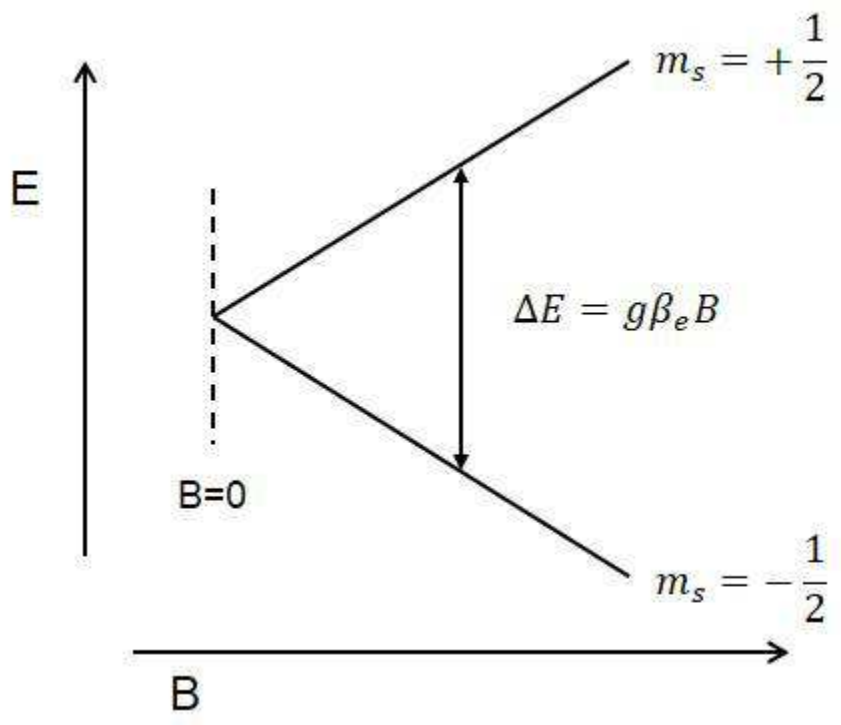

Figure 2.6. A single unpaired electron with $\mathbf{S} = \frac{1}{2}$ has the energy level(s) shown as a function of the applied magnetic field. This splitting is referred to as Zeeman splitting or the Zeeman energies. After Weil [33].

Spectroscopy in EPR results from an oscillating electromagnetic field, $\mathbf{B_1}$ inducing an electron's spin transition (i.e., flipping spin) between two differing electronic Zeeman levels. Generally, $\mathbf{B_1}$ is taken to be perpendicular to the static magnetic field, $\mathbf{B}$. The oscillating electromagnetic field is supplied by microwaves of frequency ν, and $\mathbf{B_1}$ is referred to as the microwave magnetic field.[4] When the microwave magnetic

[4]Dual mode EPR cavities do exist and are sometimes used in experiments. The dual mode cavities allow $\mathbf{B_1}$ to be either parallel or perpendicular to $\mathbf{B}$. This change in $\mathbf{B_1}$ causes ν to be

field supplies photons having energy $h\nu$ matching the spin separation energy, there is a resonant absorption by the electron from transitioning between two electronic Zeeman levels [31, 33].

$$\Delta E = h\nu = g\beta_e B \tag{2.8}$$

Since the energy between the spin states varies with magnetic field, there are two ways to provide energy for an absorptive transition: a) varying the microwave frequency at a fixed magnetic field or b) adjusting the magnetic field with a fixed microwave frequency. Most commercially available EPR spectrometers use a microwave source at a fixed frequency.

Fundamentally, an EPR spectrometer measures the small reflection of energy resulting from an impedance mismatch caused by the absorption of microwave energy from unpaired electrons. Due to the small signal strength of the impedance mismatch from these absorptive transitions, modulation coils operating around 100 kHz vary the static magnetic field improving the signal-to-noise ratio. This modulation frequently results in the plotting of EPR absorption spectrums in their first derivatives. The details of an EPR spectrometer are discussed further in Chapter 3.

2.3 Spin Hamiltonian

Electron paramagnetic resonance helps identify paramagnetic point defects within a crystal and assigns charge states. In the preceding section only the electron Zeeman term was considered. If this were the only energy contribution, all EPR spectra would appear as uniformly shaped lines varying in number based only on differing **S** values. However, in the crystal lattice, there are multiple contributions to the Hamiltonian. Solutions to the Schrodinger equation yield a complete set of interactions between

slightly different between the parallel and perpendicular modes of operation and also drive different electronic transitions.

the unpaired electron spin and the external environment describing the quantum mechanical system of a defect by its Hamiltonian identifying all possible energy levels. However, it is the spin portion of the Hamiltonian that is the basic foundation of EPR [31, 33]. Including all the various spin components, the spin Hamiltonian has the form,

$$H = \beta_e \mathbf{S} \cdot \mathbf{g} \cdot \mathbf{B} + \mathbf{S} \cdot \mathbf{D} \cdot \mathbf{S} + \mathbf{I} \cdot \mathbf{A} \cdot \mathbf{S} + \mathbf{I} \cdot \mathbf{Q} \cdot \mathbf{I} - g_n \beta_n \mathbf{I} \cdot \mathbf{B} \tag{2.9}$$

where β_e is the Bohr magneton, $\mathbf{S}$ is the spin operator, $\mathbf{g}$ is the g matrix, $\mathbf{B}$ is the magnetic field, $\mathbf{I}$ is the nuclear spin operator, $\mathbf{A}$ is the hyperfine matrix, $\mathbf{D}$ is the fine structure matrix, $\mathbf{Q}$ is the nuclear electric quadrapole matrix, $\mathrm{g_n}$ is the nuclear g factor, and β_n is the nuclear magneton. The spin portions of the Hamiltonian highlight the interaction of the spin operators, $\mathbf{S}$ and $\mathbf{I}$, with the magnetic field. Without the presence of a magnetic field, many of the energy levels are degenerate and thereby indistinguishable. Using a static magnetic field, it is possible to split these energy levels, thus reducing or eliminating the degeneracy [33].

2.3.1 Fine structure interactions: S·D·S

For paramagnetic defects with $S > \frac{1}{2}$, fine structure splitting arises due to the influence of crystal electric field on the electrons through spin-orbit coupling and the magnetic dipole-dipole interactions. Even when the magnetic field $\mathbf{B}$ is equal to zero, these levels have splitting equal in energy to $\mathbf{D}$. This splitting is often called "zero-field splitting" or "crystal-field splitting".[5] Fine structure interactions are of considerable interest and importance in transition metal ions. The pairing of d shell electrons can yield a wide variety of EPR spectra owing to the differences between high and low

[5] Although these two terms are often used interchangably in the literature, they are not the same [34].

spin systems and the interactions of the defect with surrounding ligands [31, 35, 36]. Appendix A details the fine structure interactions of the spin Hamiltonian of Cr^{3+} ($3d^3$), a high spin system in β-Ga_2O_3.

2.3.2 Hyperfine interactions: I·A·S

The magnetic interaction between an unpaired electron's magnetic moment and the magnetic moment of the nucleus is the hyperfine interaction. For each level resulting from the electronic Zeeman splitting in a magnetic field, the nucleus can also assume any of its nuclear Zeeman levels when I > 0. The number of hyperfine lines observed is dependent on the nuclear spin, I, and follows a similar pattern to the electron spin with, 2I + 1 for the total number of hyperfine transitions. The selection rule for allowed hyperfine transitions is:

$$\Delta m_s = \pm 1; \quad \Delta m_I = 0 \tag{2.10}$$

Under certain conditions rare cases of forbidden hyperfine transitions have been observed in EPR spectra, mostly in transition metal ions. Figure 2.7 details the hyperfine iteractions for a single unpaired electron in deuterium. Without the hyperfine iteractions (i.e., if I = 0), a single transition would be observed, as shown on the left. Deuterium, has I = 1 from the combined spin of an unpaired proton and neutron. The resulting allowed transitions are three absorptions of microwave energy equally spaced in the magnetic field by a distance $\Delta B = a_0$. In the example of deuterium, the total S value is 1/2. EPR spectra with S > $\frac{1}{2}$ such as weakly coupled systems of S = $\frac{1}{2}$ defects [5] or transition metal ions result in a greater number of possible hyperfine lines. The total number of observable EPR lines for a point defect

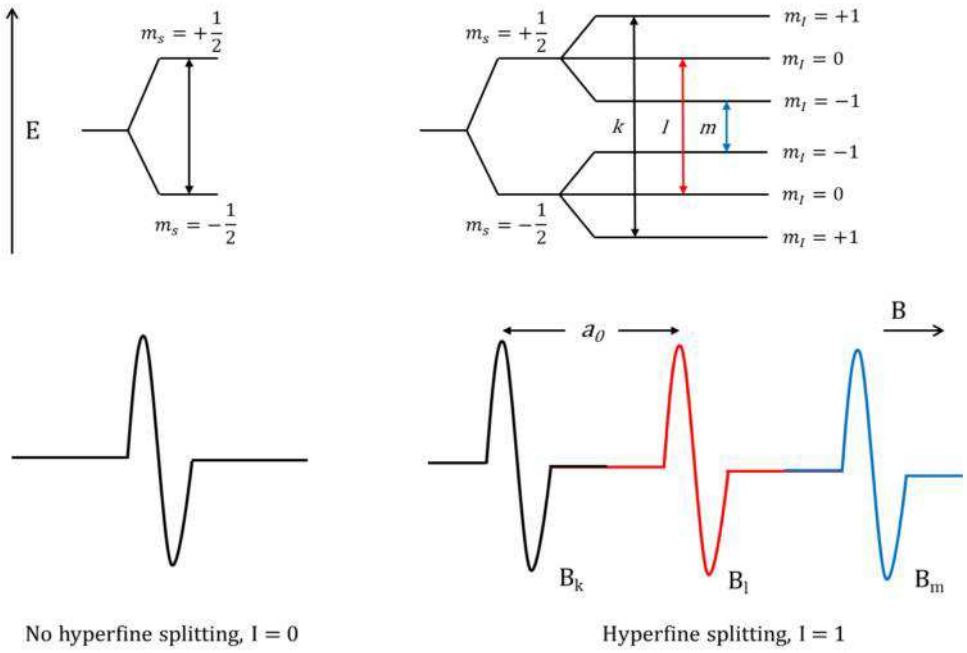

Figure 2.7. Energy levels for a deuterium atom with S = $\frac{1}{2}$ and I = 1 for a fixed magnetic field, B. The hyperfine splitting constant, a_0 is the difference in magnetic field between the various EPR transitions. After Weil [33].

in a material, along high symmetry directions in the crystal, then is given by,

$$\#\text{ of lines} = 2S\,(2I+1) \tag{2.11}$$

A common transition-metal ion impurity such as Mn^{2+} with S = $\frac{5}{2}$ and I = $\frac{5}{2}$ has a total of 30 lines that can be observed [33].

2.3.3 Nuclear quadrapole interactions: I·Q·I

Nuclear quadrapole interactions occur when nuclei have I > $\frac{1}{2}$. This term characterizes the electrical charge interactions with the nucleus and is usually the subject of study for electron-nuclear double resonance (ENDOR). In cases where EPR spectra have multiple or duplicate interpretations, study of this iteraction with ENDOR provides a definitive identification of the defect spectrum. Additionally, a defect

possessing isotopes with strong nuclear quadrapole moments and in the presence of strong electric field gradients can give rise to forbidden transitions that are observed as weak intensity lines between the defect's associated hyperfine lines.

2.3.4 Nuclear Zeeman interactions: $g_n\beta_n\mathbf{I}\cdot\mathbf{B}$

When the nucleus has I > 0 resulting from unpaired spins of the nucleons, the interaction between the unpaired electrons and nuclei can result in further splitting of the electron energy levels. The physics of nuclear Zeeman splitting of energy levels is the same as for the electrons, except the energy involved is on the order of MHz versus GHz. For comparable magnetic field values, the difference in energy is proportional to μ_n and related by $\mu_n \approx \mu_e/1836$ [31, 33].

2.4 The g Matrix

For defects observed in EPR spectra, the **g** matrix is a set of parameters used to describe the defect for different orientations of the magnetic field. The actual field for each defect's spin is not solely the external magnetic field $\mathbf{B_{ext}}$ applied to the crystal. Local fields add vectorially to the external field producing a total effective field $\mathbf{B_{eff}}$ for the unpaired electron.

$$\mathbf{B_{eff}} = \mathbf{B} + \mathbf{B_{local}} \tag{2.12}$$

Two local fields exist, those that are: a) permanent and independent of **B** except in orientation; and b) having a magnitude dependent on **B** because they are induced by **B** [33]. The matrix contains isotropic and anisotropic terms. When a defect has hyperfine iteractions, the center of the spectrum is taken for a g value. A simple relationship between the spectrum's center along the high symmetry direction and magnetic field,

$$g = \frac{h\nu}{\beta_e B_{ext}} \tag{2.13}$$

can often give an indication of whether a defect is an electron or hole trap. A very loosely applied rule is that g values > 2.0023 indicate hole traps, while g < 2.0023 indicates electron traps [37]. Here g $= 2.0023$ is the free-electron g value, g_e.

Defects that are truly isotropic are quite rare and typically found in cubic materials possessing no distortion of the crystal lattice, or in certain liquid samples. More frequently, the spin-orbit iterations and $\mathbf{L} \cdot \mathbf{S}$ coupling with the magnetic field produce line splittings and shifts due to orientations in the magnetic field. A defect's EPR spectrum that is shifted in magnetic field, and therefore g values, from the interactions with the surrounding ligands but produces the same hyperfine pattern along high-symmetry directions of the crystal is referred to as "crystallographically equivalent". The shift in magnetic field, and g, values results from the direction and $\mathbf{L} \cdot \mathbf{S}$ coupling of the unpaired spin in its orbital. Splitting of a defect's EPR spectrum when rotated off high-symmetry axes can occur due to interactions with the surrounding ligands. This effect is referred to as "magnetically inequivalent" whereas a lack of splitting is "magnetically equivalent" for orientations of the defect [33, 38].

Several general characteristics of a defect's g values can be mentioned. Unpaired spins localized primarily in hydrogenic-like s orbitals exhibit very little angular dependence, and little deviation in g from g_e when the crystal is rotated in the magnetic field. Defects having unpaired spins in p orbitals generally have angular dependencies resulting in g shifts less than several hundredths from g_e. Transition metals can have widely varying g values that increase in deviation from g_e as $\mathbf{L} \cdot \mathbf{S}$ coupling increases.

Anisotropy of the g matrix can be defined with six parameters. A physical system possessing three mutually perpendicular inherent directions (i.e., principle axes) combined with results (principle values of the defect) measured along these directions completely describe the anisotropy contributions [31, 33]. Equation 2.13 is only sufficient to describe systems that are isotropic. Resonant field values are actually a

function of field orientation relative to the crystal axes.

The g matrix describes the ground state interaction of the defect for different orientations of the magnetic field. The spin-orbit interactions admixes the "pure" ground state with the excited states causing a small amount of orbital angular momentum to manifest in the observed ground state. This circulation produces a local field, $\mathbf{B_{local}}$ mentioned in equation 2.12 that contributes vectorially to the external magnetic field, $\mathbf{B}$. This interaction results in changes to the g factor and is inversely proportional to the energy separation of the basis states [33].

The electron's magnetic moment described in Section 2.2 is a magnetic moment operator that is a vector sum of the spin and orbital angular momenta,

$$\hat{\mu}(\mathbf{r}) = -\beta_e \left(\hat{\mathbf{L}} + g_e \hat{\mathbf{S}} \right). \tag{2.14}$$

The total electronic orbital angular-momentum operator for the ground state configuration of the defect is represented by $\hat{\mathbf{L}}$. Combining spin and orbital angular momenta with the electron Zeeman terms, the Hamiltonian describing the system becomes

$$\hat{H}(\mathbf{r}) = \beta_e \mathbf{B}^T \cdot \left(\hat{\mathbf{L}} + g_e \hat{\mathbf{S}} \right) + \lambda \hat{\mathbf{L}}^T \cdot \hat{\mathbf{S}}. \tag{2.15}$$

First and second order time-independent perturbation theory detail the contributions from the admixing of states through summation over all the states. A 'spin only' Hamiltonian results,

$$\hat{H} = \beta_e \mathbf{B^T} \cdot \mathbf{g} \cdot \hat{\mathbf{S}} + \hat{\mathbf{S}}^T \cdot \hat{\mathbf{D}} \cdot \hat{\mathbf{S}}. \tag{2.16}$$

The g matrix can be shown to have the form,

$$\mathbf{g} = g_e \mathbf{l}_3 + 2\lambda \mathbf{\Lambda} \tag{2.17}$$

where $\mathbf{1}$ is a 3×3 unit matrix and Λ is the outer product from second order perturbations. In the absence of off-diagonal terms, the g matrix has principle values of

$$g_1 = g_e, \quad g_2 = g_e - \frac{2\lambda}{E_2 - E_1}, \quad g_3 = g_e - \frac{2\lambda}{E_3 - E_1}. \tag{2.18}$$

These values are presented in the literature [38] for EPR spectra that are both crystallographically and magnetically equivalent.

2.5 Optical Spectroscopy

The optical spectral regions of interest in this dissertation span from the ultraviolet (UV) to the infrared (IR) wavelengths. The foundations of optical spectra including photoluminescence (PL) and IR active spectra are discussed, while thermoluminescence is discussed separately in section 2.6. Molecular electronic states can be arranged in increasing order of energy with highest filled energy level referred to as the highest occupied molecular orbital (HOMO). The first available level above HOMO is the lowest unoccupied molecular orbital (LUMO). Separation of energy into HOMO and LUMO levels and spin pairing between the ground and excited state form the singlet and triplet states. Since photons possess no inherent spin, they can only couple to transitions of the same spin [39]. The relaxation and de-excitation process between singlet and triplet states occur on different time scales and gives rise to fluorescence and phosphorescence discussed in section 2.6 [40]. The molecular electronic transitions can also change the vibrational state; therefore the optical transitions are considered vibronic, a combination of changes in the electronic and vibrational state. The electronic transitions arising from the average electric field gradients of the crystal field supplied by the surrounding lattice ions are referred to as a *static* perturbation. Since individual ions vibrate about their lattice position, discrete vibrational levels are associated with each molecular electronic state. These vibrations are referred to

as a *dynamic* perturbation and have an associated temperature dependence [41].

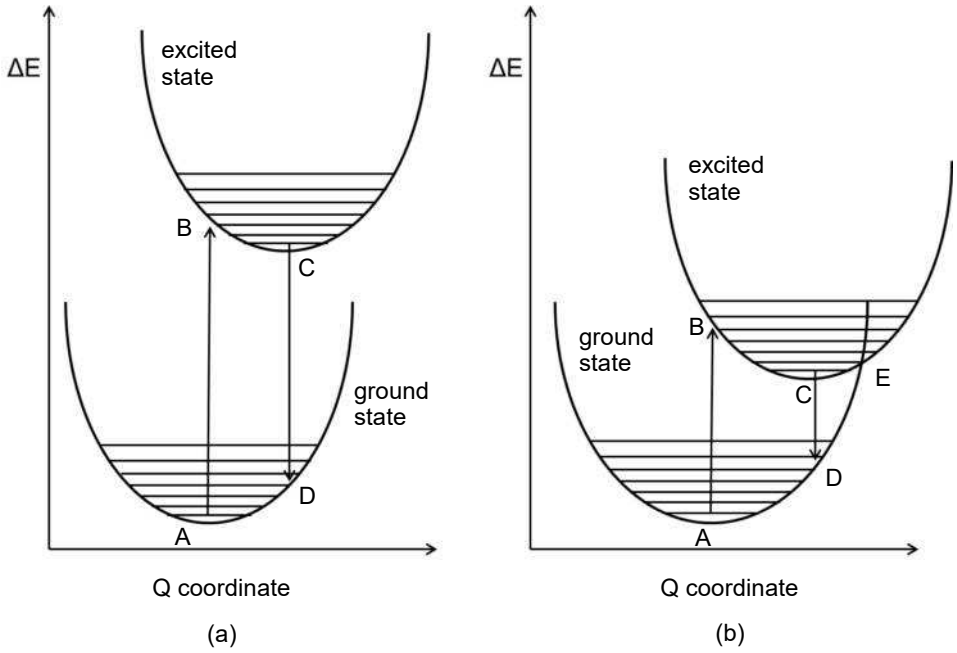

Figure 2.8. Configuration coordinate diagram for a) radiative and b) non-radiative processes. The Frank-Condon principle is illustrated by the transitions $\overrightarrow{AB}$ and $\overrightarrow{CD}$ in radiative transitions. The horizontal lines represent local vibrational modes. Non-radiative recombination occurs when strongly coupled vibrational modes are available to excited electrons at higher energies E than radiative transitions $\overrightarrow{CD}$.

In contrast, impurity ions (i.e. isolated point defects) incorporated into crystals strongly couple to the vibrational modes of lattice through electron-phonon coupling which creates continuous vibronic bands. The relatively low concentration of the defects creates an interaction which strongly affects the optical spectra. The coupling of electronic states to a near continuous spectrum of vibrational modes is governed by the density of states of the vibrational modes in dispersion curves. The absorption of an allowed photon transition for a point defect is shown as $\overrightarrow{AB}$ in Figure 2.8a, with energy

$$\hbar\omega_a = (E_2 - E_1) + n\hbar\Omega_2 \tag{2.19}$$

where $\hbar\omega_a$ is energy of the absorbed photon, Ω_2 is the phonon angular frequency in the excited state and n is an integer. Equation 2.19 dictates that absorption by a point

defect is possible for a band of energies determined by $(E_2 - E_1)$ up to a maximum allowed by the electron-phonon coupling. Absorption transitions leave the ion in an excited state and the excess energy is dissipated in a radiationless relaxation process by exciting phonons which transfer their energy as heat to the crystal. Emission of a photon at the bottom of the excited state in Figure 2.8a is shown by $\overrightarrow{CD}$ with energy

$$\hbar\omega_e = (E_2 - n'\hbar\Omega_1) - n\hbar\Omega_1 \tag{2.20}$$

where Ω_1 is the phonon angular frequency in the ground state and n' is an integer.

The difference in energy between emission and absorption is the Stokes shift. The photon-induced change in electronic energy is represented as ΔE while the change due to coupling with a vibrational mode is represented by a change in Q in Figure 2.8. The difference in minima between the ground and excited states defined by the Q coordinate is quantified by the Huang-Rhys parameter for the transition. This process of energy absorption, emission, and vibrational rapid relaxation in often described as the Frank-Condon principle and represented on the configuration coordinate diagram by vertical arrows. The overlap of vibrational modes (called the Frank-Condon factor) and electronic orbitals that allow for these transitions to occur is something not well accounted for in CFT and one of its main limitations in accurately predicting optical absorption spectra [39].

Non-radiative decay can also occur after the absorption of a photon via the process shown in Figure 2.8b. For transition metal defect ions that strongly couple to the crystal lattice, there is a strong dependence on vibronic modes and temperature. A photon is absorbed, $\overrightarrow{AB}$, but the strong coupling of defect and host lattice have an energy shown as point E that is higher than the minimum of the excited state transition $\overrightarrow{CD}$. The excited electron can transfer the excess energy as phonons and return to the ground state without emitting a photon. When this occurs, a defect

is termed a 'nonradiative center' and this process is called 'quenching' or 'thermal quenching'. [39, 40].

2.5.1 Photoluminescence and photoluminescence excitation

Photoluminescence (PL) and photoluminescence excitation (PLE) are measurement techniques that characterize and identify luminescent defects in single crystals. These techniques focus on the Stokes shift. PL measures the emission of a defect and PLE measures the absorption.

2.5.2 IR absorption due to a change in dipole moment

Vibrational modes between ions that are IR active are more commonly reported as absorptions resulting in a coupling to the dipole moment. However, transition metal ion point defects with partially filled d shells provide an additional pathway for coupling to the dipole moment. The splitting of the electronic orbitals into the t_{2g} and e_g states allows for energy absorption promoting electronic transitions between these levels. This is referred to as a $d-d$ transition. On an octahedral site, CFT has shown that these orbitals point towards or between anions. The absorption of energy can excite an unpaired electron in $d-d$ transitions that results in coupling to the dipole moment.

Combined with EPR measurements, IR absorption spectroscopy can provide information about the oscillator strength of a transition for a defect's transition. The relationship is provided from Smakula's formula for a Lorentzian line shape

$$Nf = \left(1.29 \times 10^{17}\right) \frac{n}{(n^2+2)^2} \alpha_{max} W \tag{2.21}$$

where N is the defect concentration (can be measured by EPR) in units of [cm^{-3}], f is the oscillator strength, n the index of refraction for the material, α_{max} the

absorption coefficient at the peak with units [cm^{-1}], and W the FWHM measured in meV [36, 42, 43].

2.6 Thermoluminescence (TL)

The underlying principles of thermoluminescence (TL) were developed to describe a subset of luminescence behaviors. There are many broad categories of luminescence phenomena classified according to the type of absorbed radiation exciting emission including photoluminescence (light), radioluminescence (x rays), and cathodoluminescence (electrons), among others. Light emission that takes place after the absorption of radiation can be subdivided based on a characteristic time τ_c. Fluorescence has $\tau_c \leq 10^{-8}$ s and phosphorescence has $\tau_c \geq 10^{-8}$ s. Phosphorescence is further distinguished from fluorescence by its dependence on temperature and characterized by the time delay between radiation absorption and the time it takes to reach full intensity. Thermoluminescence is a specialized type of phosphorescence with $\tau_c \geq 10^{-4}$ s.

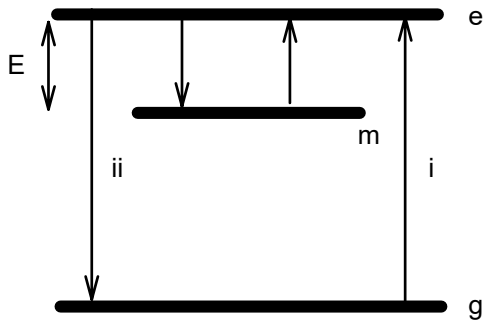

Figure 2.9. Energy transition involved in the process of phosphorescence. States g, m, and e represent the ground, metastable, and excited states for a defect in a material. After McKeever [40].

Figure 2.9 depicts a simplified explanation of phosphorescence. An electron is excited from the ground state g (transition (i)), to an excited state e, and then becomes trapped at a metastable state m in the forbidden energy gap between e and g. It remains at state m until enough energy E is provided to lift it from this state,

returning to e and then de-exciting (transition (ii) back to g. The amount of time spent in the trapped state m is shown from thermodynamics arguments to be,

$$\tau = s^{-1} \times e^{-\frac{E}{k_B T}} \tag{2.22}$$

where s is a constant that will later be shown as the "attempt-to-escape" frequency with units [s^{-1}], E is the energy difference between m and e, k_B is the Boltzmann constant, and T the temperature in kelvin [40].

The decay to the ground state after the electron is freed from trap m has been the subject of several different formalisms based on probabilities. If the probability once the electron is freed from state m of returning to state m is much less than the probability of returning to g, the process is considered first order. This type of decay is exponential [40, 44, 45]. However, if the probability of returning to state m is greater than the probability of returning to the ground state, the process is considered second order. This type of decay is not exponential [40, 46]. These two cases represent the extremes of decay behavior. Other models are based on a linear combination of the first and second order, or on empirical fitting attempt to describe observed decay behaviors between these two extremes [47–49]. There remains debate on which model, mixing of first and second order (i.e., mixed order) or the empirical fitting (i.e., general order), yields a more accurate and physical understanding of the decay processes between the extremes [40, 47, 50, 51].

The simple illustration shown in Figure 2.9 does not completely capture the fundamental principles of thermoluminescence applied to solids. The formation of the valence and conduction bands creates a "forbidden" energy gap, E_g. The perfect crystal lattice contains no states within the energy gap, but various intrinsic and extrinsic defect states do provide levels within E_g. In thermal equilibrium, occupation of the states is governed by the Fermi-Dirac distribution, leading to the concept of

the Fermi level, E_f of the material. A high E_f indicates that most of the available states below the conduction band are filled and a low E_f denotes states close to and immediately above the uppermost-valence band are filled.

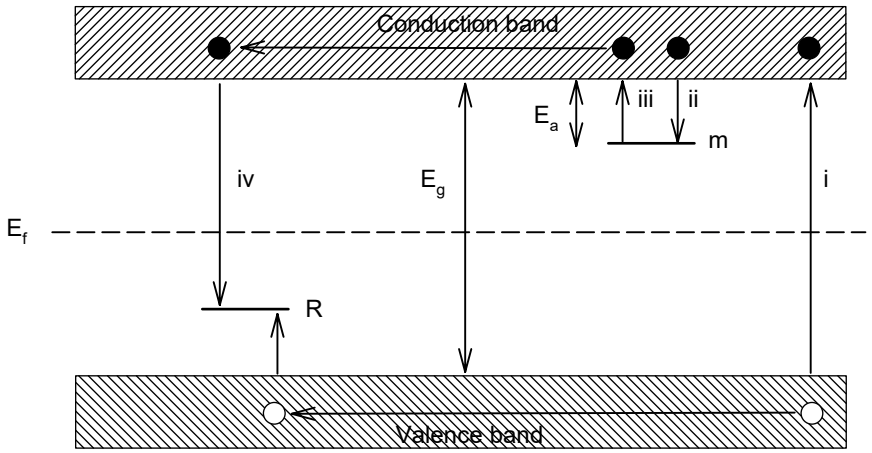

Figure 2.10. Simplified diagram of a one trap-one recombination energy band model showing notional electronic transitions in a TL material. (i) Electron-hole pair generation, (ii) electron and hole trap at a given energy level or defect site in the material, (iii) releasing of trapped charge by heat, (iv) and recombination resulting in luminescence. Electrons are represented by solid circles, and holes are shown as open circles. R is the recombination defect site's level, E_g is the band gap energy, E_a represents the depth of the trap, and E_f is the Fermi level. After Holston and Bos [52, 53].

When an electron is given enough energy (e.g., from lasers of x rays), it can be promoted from the valence band or one of the filled defect states into the conduction band shown in Figure 2.10 by transition (i). The electron becomes trapped (shown by transition (ii)) at defect site m that lies below the bottom of the conduction band. The original state the electron filled is now vacant and the absence of charge travels through the valence band until arriving at a separate defect site R and is now considered a trapped hole above the valence band.[6] The energy required to free the electron from its trapped state is called the activation energy E_a or trap depth. "Shallow" traps require small fractions of E_g to release trapped charge and "deep" traps need larger energies. In thermoluminescence, the energy required to liberate

[6]It is possible in rare cases for the same defect to act simultaneously as an electron and hole trap. This type of defect is referred to as amphoteric.

the trapped charge (transition iii) is supplied by heating. The trapped charge can be stable or semi-stable depending on the depth of the trap. Charge traps can be stable for years if held sufficiently below the critical release temperature.

Supplying the trapped electron with enough thermal energy allows the electron to overcome the potential energy barrier, shown as transition (iii). Once the escaped electron becomes mobile, it will travel in the conduction band until recombining with a trapped hole, shown by the transition (iv). This simple model assumes a single electron-hole trap (i.e., a single recombination center). Using this model, if the recombination center enters an excited state and is also a luminescent center, light emission occurs as it returns to the ground state. The amount of trapped charge in these states that is released by increasing temperature is directly proportional to the light emitted from recombination. When applied to dosimeter materials, the measurement of emitted light then provides a direct measurement of the radiation dose the material received [40].

While TL measurements can provide direct radiation dose measurements, the simplified single electron-hole model neglects several important considerations. Materials often have more than a single defect, resulting in traps at various depths in the band gap. The temperature at which an electron is freed from its trap does not prevent it from being retrapped elsewhere in the gap (i.e., a kinetic order > 1) before eventually recombining and returning to the ground state. Electrons can combine radiatively or non-radiatively (i.e., thermal quenching) as shown in Figure 2.8. Additionally, trapped holes are also released by the same processes and can recombine at a trapped electron site [40, 51]. The single electron-hole trap model (also referred to as the two-level model) forms the foundation for describing TL kinetics. Thermoluminescence analysis enables extraction of key parameters describing a defect and the charge transfer process. Key parameters in TL include the activation energy E_a (usually given in

units of eV) and the frequency factor s (the attempt-to-escape frequency and reported in units of s^{-1}). When the key parameters are combined with a known heating rate, (β) and EPR data are available to estimate the total concentration trapped charge [cm^{-3}], (n), a TL "glow curve" (the radiative recombination intensity as a function of temperature) can be predicted [40].

2.6.1 First order kinetics

In first order kinetics described by Randall and Wilkins [44,45], the process of trap emptying in the two level system is given strict limitations. Specifically, their analysis imposed the restriction that there is a negligible probability of retrapping compared to the probability of recombination regardless of defect concentration. Mathematically, the measured TL intensity follows the exponential expression,

$$I(t) = -\frac{\mathrm{d}n}{\mathrm{d}t} = n\, s\, e^{-\frac{E_a}{k_B T}} \tag{2.23}$$

and when integrated from $t = t_0$ with the assumption of a linear heating rate, yields the expression

$$I(T) = n_0\, s \exp\left(-\frac{E}{k_B T}\right) \exp\left[-\frac{s}{\beta}\int_{T_0}^{T} \exp\left(\frac{E_a}{k_B T}\right) \mathrm{d}T\right] \tag{2.24}$$

Adjusting each of the key parameters (E_a and s) and β separately highlights their effect on the intensity and peak position.

The activation energy E_a is a defining characteristic for defects in the process of electronic device development and radiation dosimetry. The effect of E_a on TL peak position for three different values is shown in Figure 2.11 where $n_0 = 1$ (set for illustrative purposes), $\beta = 1.0$, and $s = 10^{10}$. As the trap depth increases, charge is held until much higher temperatures. Traps that are too deep inhibit the release of elec-

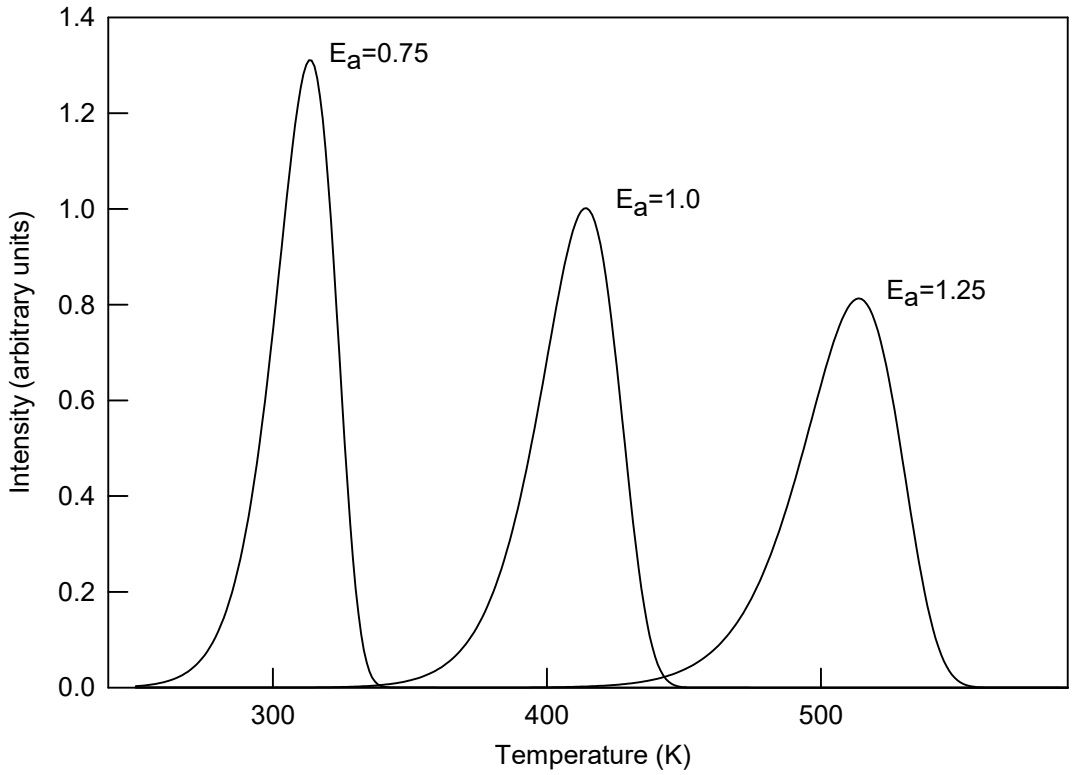

Figure 2.11. Simulation of the effect of activation energy, E_a eV on a first-order kinetics TL peak position for three different energies. For each simulation curve, values of $n_0 = 1$ cm^{-3}, $\beta = 1.0$, and $s = 10^{10}$ s^{-1}. After McKeever and Chen [40, 51].

trical charge making them unsuitable for device application. Conversely, traps that are too shallow are problematic for radiation dosimetry because they are subject to thermal fading, a process where charge is slowly released over time, skewing accurate dose calculations. The characteristic shape of the first order TL glow curve results from the probability of trap emptying at lower temperatures and lack of retrapping. Since the probability of recombination greatly exceeds the probability to retrap, the linear heating rate empties all trapped charge and after E_a is surpassed, luminescence is truncated.

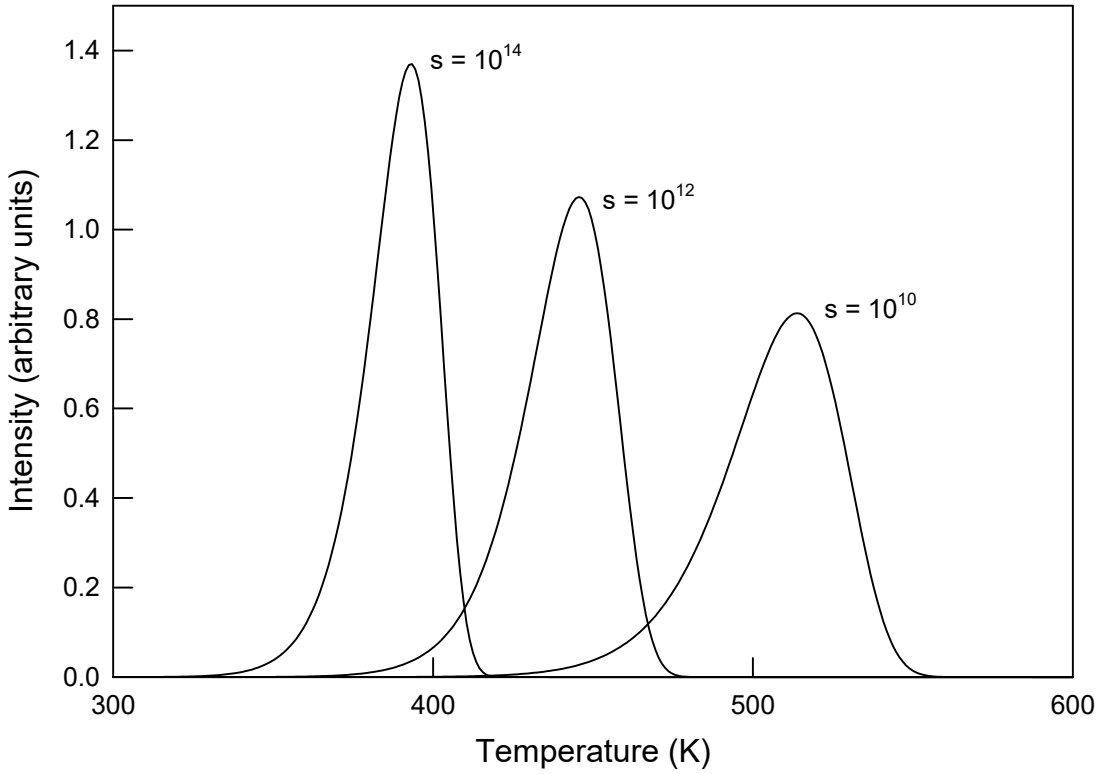

Figure 2.12. Simulation of the effect of varying s s^{-1} on a first-order kinetics TL peak position for three different values of s. For each simulation, the parameters are held constant at values of $n_0 = 1$ cm^{-3}, $\beta = 1.0$, and $E_a = 1.0$ eV. After McKeever and Chen [40, 51].

The effect of varying the frequency factor s on TL peak position and shape for three different values is shown in Figure 2.12 with $n_0 = 1$ cm^{-3}, $\beta = 1.0$, and $E_a = 1.0$

eV held constant. As the attempt-to-escape frequency increases, there is a greater probability of release at lower temperatures. This results in the TL peak narrowing its full width at half maximum (FWHM) and shifting to lower temperatures. The characteristic TL shape dependence on E_a and s for differing values does not alter the total area (i.e. luminescence) under the curve when all other parameters are held constant.

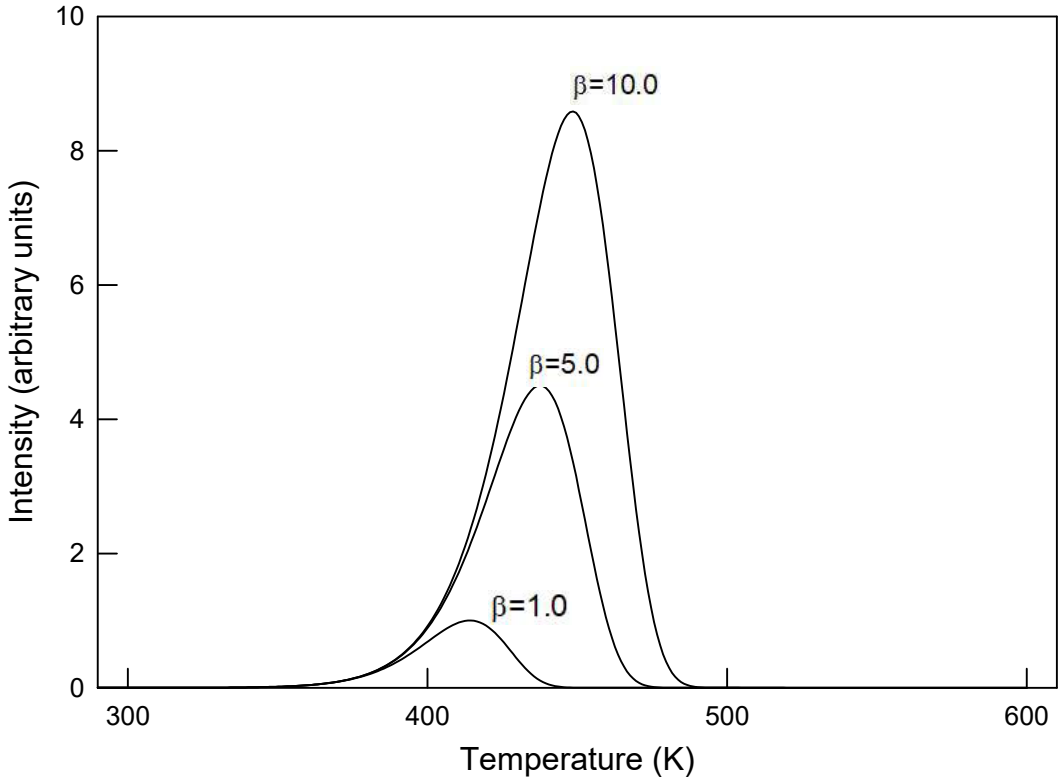

Figure 2.13. Simulation of the effect of heating rate, β on a first-order kinetics TL peak position for three different rates. For each simulation, the parameters are held constant at values of $\mathbf{n_0 = 1\ cm^{-3}}$, $\mathbf{E_a = 1.0\ eV}$, and $\mathbf{s = 10^{10}\ s^{-1}}$. After McKeever and Chen [40, 51].

Finally, changing the heating rate can have a large effect on the intensity as function of temperature and peak position. Shown in Figure 2.13 are the TL peaks for three different heating rates with $n_0 = 1\ \mathrm{cm}^{-3}$, $s = 10^{10}\ \mathrm{s}^{-1}$, and $E_a = 1.0$ eV held constant. As the heating rate increases, the TL peak shifts to higher temperature and

increases in intensity. On a temperature axis, the peak area scales with increasing β, but if the luminescence were plotted as a function of time the total peak areas remain the same for differing values of β. To avoid this effect, all heating rates used in this dissertation are held constant at $\beta = 1.0$.

2.6.2 Second order kinetics

In second order kinetics described by Garlick and Gibson [46], the process of trap emptying in the two level system is also given a strict limitation: there is a negligible probability of recombination compared to the probability of retrapping. The mathematical expression for TL intensity of second order kinetics has the form,

$$I(t) = -\frac{\mathrm{d}n}{\mathrm{d}t} = n^2\, s'\, e^{-\frac{E_a}{k_B T}} \tag{2.25}$$

where $s' = s/RN$ and $R = 1$ for cases of interest, and N the total number of trapping sites. When the above expression is integrated from $t = t_0$ with the same assumption of a linear heating rate, it yields the expression

$$I(T) = n_0^2\, s' \exp\left(-\frac{E}{k_B T}\right)\left[1 + -\frac{n_0 s}{\beta}\int_{T_0}^{T} \exp\left(\frac{E_a}{k_B T}\right)\mathrm{d}T\right] \tag{2.26}$$

Compared to the first order expression, the TL peak grows nearly proportional to n_0 and is shifted to lower temperature [40,51]. The dependence on an attempt-to-escape factor carries an additional condition biased by N and is called the "effective" pre-exponential factor, $s' = s/N$ with units ($\mathrm{s}^{-1}\mathrm{m}^3$). The key parameters of s, E_a, and β have a similar effect on peak position, but are now biased towards increasing the TL peak's tail on the higher temperature side. Physically the process of rapid retrapping delays the onset of luminescence. The TL band appears more symmetric in shape.

2.6.3 General order kinetics

Observed TL peaks are rarely purely first or second order in shape [40, 47–49, 51]. In non-ideal (i.e. real) solid materials, starting powder purity and the crystal growth process contribute to a wide range of intrinsic and extrinsic defects, differing in defect concentration, trap depth, and spatial separation. This range of available states complicates and potentially distorts the recombination process. May and Partridge [48] noted these deviations from pure first or second order decay, and generalized the intensity expression empirically,

$$I(t) = n^b \, s' \, e^{-\frac{E_a}{k_B T}} \tag{2.27}$$

where s now has the dimensions $\mathrm{m}^{3(b-1)}\mathrm{s}^{-1}$ and b is general-order parameter with $1 < b < 2$. Integration yields a temperature dependent intensity of the form,

$$I(T) = n_0^2 \, s'' \exp\left(-\frac{E}{k_B T}\right)\left[1 + -\left((b-1)\frac{n_0 s'}{\beta}\right)\int_{T_0}^{T} \exp\left(\frac{E_a}{k_B T}\right) \mathrm{d}T\right]^{-\frac{b}{b-1}} \tag{2.28}$$

The parameter $s'' = s' n_0^{b-1}$ in the final expression causes concern due to its dependence on the changing units of s and was later refined by Rasheedy [54] to eliminate this factor by,

$$n^b s' = \left(\frac{n^b}{N^{b-1}}\right) s \tag{2.29}$$

When compared to TL peaks with all other parameters held constant, the difference in peak shape between orders of kinetics can be distinguished on the high temperature side shown in Figure 2.14.

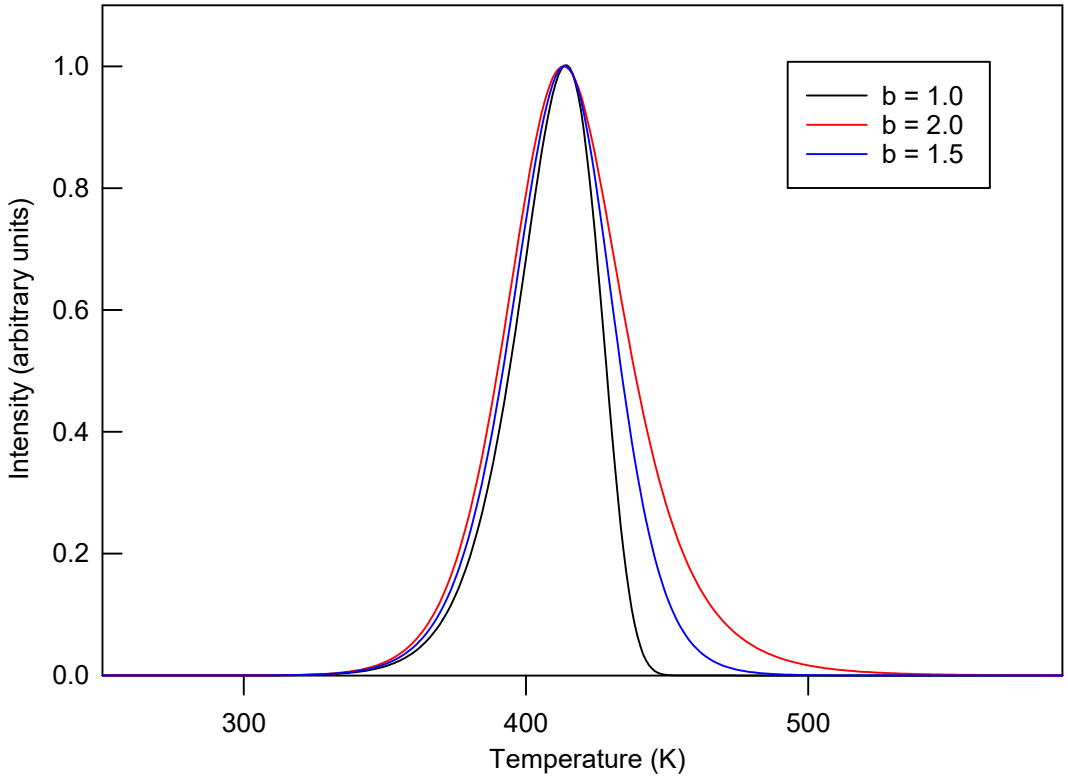

Figure 2.14. Simulation of the effect of kinetic order b on TL peak shape for three different values of b. For each simulation, the parameters are held constant at values of $n_0 = 1$ cm^{-3}, $\beta = 1.0$, $E_a = 1.0$ eV, and $s = 10^{10}$ s^{-1}. After McKeever and Chen [40, 51].

2.7 Ir^{4+} d^5 in a Strong Octahedral Field S= $\frac{1}{2}$

Transition metal ions have been a subject of deep interest [31]. In particular, iridium has received renewed interest in iridate compounds for its unusual electric and magnetic properties [55–58]. Iridium in the 4+ charge state has a $[\mathrm{Xe}]\,4f^{14}5d^5$ electronic configuration. This is a low spin complex with $\mathrm{S} = \frac{1}{2}$ for the reasons stated in the preceding section 2.1. Early work on iridium compounds such as $[\mathrm{IrCl_6}]^{2-}$ and $[\mathrm{IrBr_6}]^{2-}$ was conducted by Griffiths and Owen [59–61]. This experimental work confirmed predictions from CFT on the diffuse nature of the d orbitals. Measurements calculated an orbital reduction factor, $k = 0.83$, indicating 17% of the electronic orbitals spread onto the surrounding ligands [61].[7] Inclusion of the admixtures from excited states considerably affects analysis of experimental results, and the theory of $[\mathrm{IrX_6}]^{2-}$ was extended further by Thornley [62]. The results highlighted the larger nature of covalent bonding than previously assumed.

The degree of covalent bonding from defects having $5d$ electrons such as Ir highlights the shortcomings of the ionic treatment of solids from CFT. While CFT provides a framework for successfully understanding the fundamental nature of the bonding involved, inclusion of the admixing orbitals is necessary to accurately predict optical effects [27]. A complete discussion on the role of iridium in β-$\mathrm{Ga_2O_3}$ is discussed in Chapter 5.

[7] A value of k = 1.0 indicates no reduction or diffusion of the d orbitals onto the surrounding ligand ions.

3. Experimental Setup

3.1 Electron Paramagnetic Resonance Spectrometer

EPR spectroscopy is a technique by which insulating and semiconducting materials and point defects are studied by using a fixed microwave frequency source, and varying the static applied magnetic field. EPR measures the changes in absorbed microwave power. EPR is only effective for characterizing materials and defects when $S > 0$ because at least one unpaired electron is required to allow transitions between the available energy levels dictated by the spin Hamiltonian. EPR flips electron spins in the applied magnetic field, and therefore the difference in electron populations of the energy levels is important in determining observable transitions. For electrons to flip spin and generate an EPR signal, there must be a population imbalance. If the populations are equal, then the total difference between spin up and spin down is zero, and no signal is generated. Conversely, if there is a population imbalance, then there are unpaired spins and available energy states for an electron transition through flipping spin (either $\uparrow$ to $\downarrow$ or opposite).

Utilizing knowledge of the energy levels and spin, EPR spectroscopy can identify defects within a material. The EPR spectrometer has several key components including the microwave source, resonant cavity, and magnet. For the block diagram shown in Figure 3.1, the microwave source is in the bridge, the sample is located in the cavity resonator, the electronics that enhance phase sensitive detection are contained in the block "signal channel", and the "field controller" is the electronic adjusting current of the applied static magnetic field. Not shown in Figure 3.1 are the pumps circulating water to cool the magnetic coils. Without these pumps, the coils overheat and the spectrometer ceases functioning.

The experimental configuration of an EPR spectrometer equipped with cryogenic

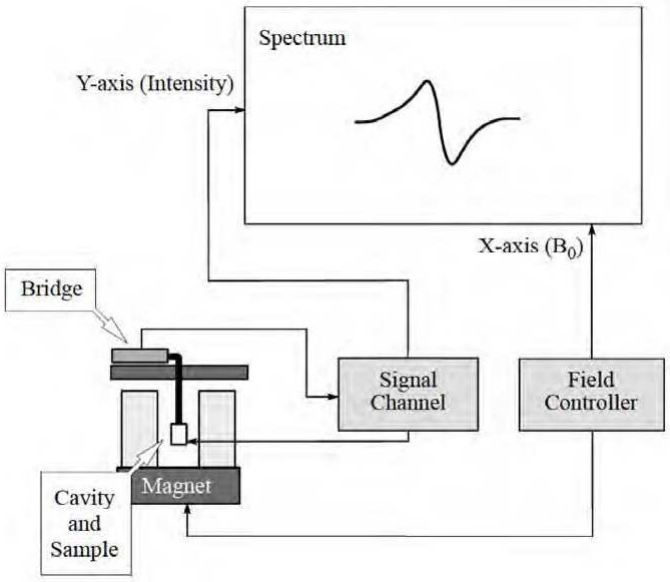

Figure 3.1. An EPR spectrometer block diagram of operation.

Figure 3.2. Experimental configuration of an EPR spectrometer for operation with liquid He.

components operating with liquid helium is shown in Figure 3.2. Liquid helium temperatures assist EPR measurements in several ways. Large concentrations of electrons in the conduction band absorb microwave energy and do not allow the microwaves to penetrate into the crystal. For materials that are n-type, absent from competing external energy sources (i.e., laser or ambient light), lowering the temperature freezes electrons out of the conduction band, returning them to the original defect site. Second, lowering the temperature lengthens the spin-lattice relaxation times for all defects assisting in creating the necessary population inversions. A Bruker EMX EPR spectrometer is used in this dissertation, and several of the key components shown in Figures 3.1 and 3.2 are detailed below. A complete explanation of all the components and spectrometer operation are available in other resources [33, 63, 64].

The microwave source is a Bruker EMX bridge diode (a Gunn diode), operating in the X-band, typically around 9.4 GHz, shown in Figure 3.3 as point A. Energy travels from the Gunn diode, through an attenuator at point B, down the waveguide and into the resonant cavity. The attenuator allows precise control of the microwave power. For weak signals, higher power can be used to lift signals above the noise, while for strong signals power settings are adjustable to minimize saturation effects from spin-lattice relaxation and keep signals on scale. Microwave energy enters the circulator C, through an initial port 1, travel down towards the sample through port 2. Reflected energy from the sample cavity D, returns through the waveguide and into the circulator exiting through port 3, towards the detector shown as E. The most common detector is a Schottky diode crystal. Microwave energy leaving from the Gunn diode is also sent through the reference arm F, acting as bias on the detector. The reference arm enables the reference and reflected signals to be in-phase when combining on the detector to minimize noise [33]. Improving signal-to-noise is a key factor in detection of EPR signals.

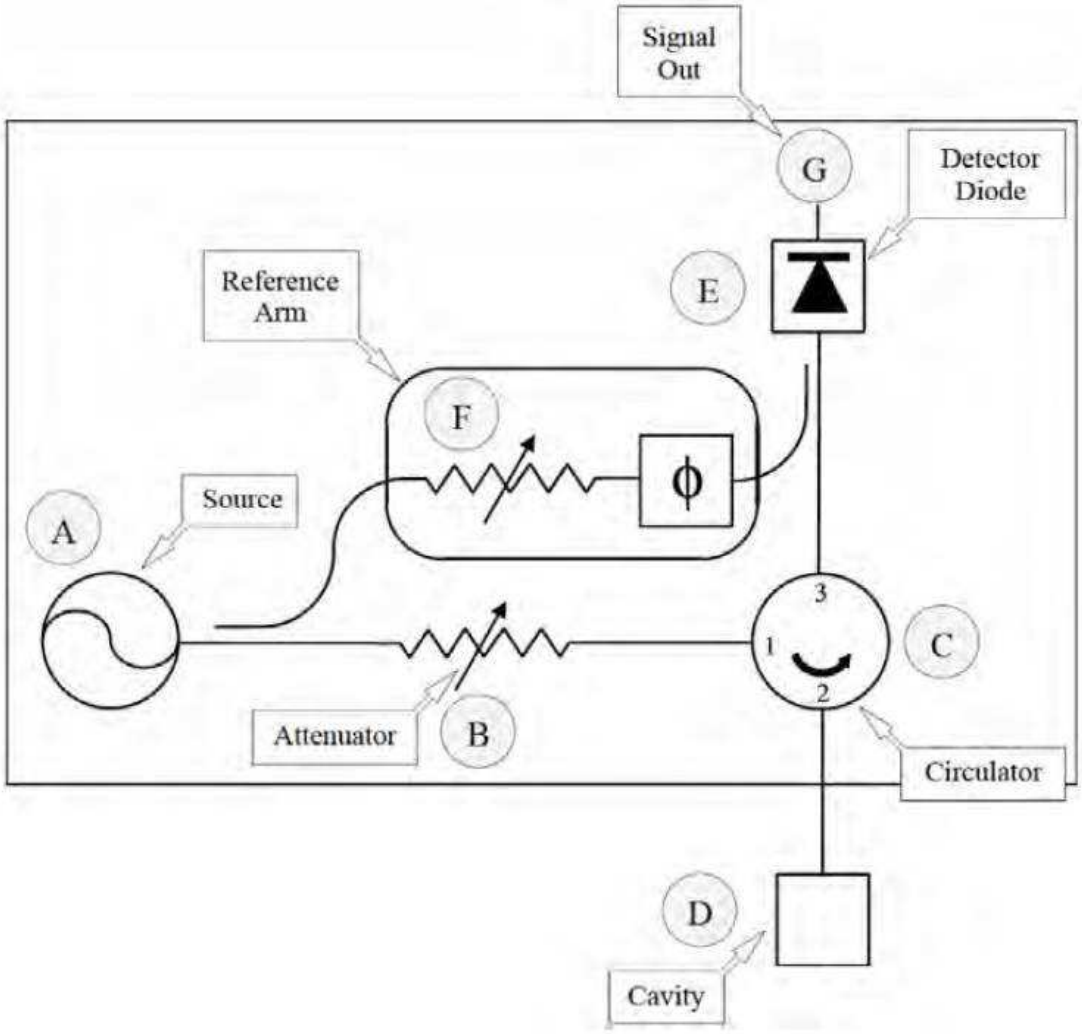

Figure 3.3. Block diagram of a microwave bridge used for EPR measurements.

3.1.1 EPR sample cavity

The EPR sample cavity used in the Bruker EMX spectrometer and referenced in Figure 3.2 is a cylindrical metal cavity. The dimensions of the cavity ensure the microwaves are capable of forming standing waves inside the chamber resulting in an impedance match. Each microwave cavity has its own resonant frequency and a measure of the effectiveness is the quality factor, Q. This Q factor describes how effectively the cavity stores energy and it is predefined for the system used in this dissertation. The standing electromagnetic waves in the sample chamber have their electric and magnetic fields 90° out of phase with each other and perpendicular to the applied static magnetic field. Positioning sample height within cavity minimizes the degradation of Q and also maximizes EPR signals [33]. The choice of sample rod can also affect the detection of signals. Rods with Teflon sample holders in some experiments have been shown to produce less intense EPR signals than those mounted on glass rods for identical spectrometer settings and sample placement. The small change in the dielectric constant between sample holders may slightly compress the electromagnetic field lines in the vicinity of the sample yielding more intense signals with glass rods.

Microwaves are impedance matched to the cavity through an iris. The Teflon iris screw adjusts the aperture size at the back of sample cavity allowing better coupling of the microwave energy to the cavity. Tuning the cavity is analogous to the mechanics involved in the standing waves of a pipe organ. Reflections that are not submultiples of the cavity dimensions result in destructive interference, while at approximately one half of the wavelength of the cavity is the fundamental mode. Screwing the iris in or out, assists in minimizing reflections, thus increasing coupling and tuning the cavity. When the reflections are minimized or eliminated, the cavity is considered "critically coupled".

The EPR sample cavity is designed so that the magnetic fields of the microwaves and static applied field are perpendicular. The oscillating microwave magnetic field induces the EPR transition (i.e., a small absorption of energy) resulting in an impedance mismatch, which reflects energy back through the waveguide and into the detector [33].

3.1.2 Phase sensitive detection

Phase sensitive detection for the EPR spectrometer used in this dissertation enables detection of paramagnetic defects with concentrations as low as 5×10^{10} cm^{-3} at 10 K. Estimates for S $= \frac{1}{2}$ defect concentrations can be calculated using [65]

$$\mathrm{N} = \left(5 \times 10^{10}\right) (\Delta B)^2 \left(\frac{S}{N}\right) L \left(\frac{T}{10}\right) V^{-1} \quad \left[\mathrm{cm}^{-3}\right] \tag{3.1}$$

where ΔB is the line width measured in Gauss, S/N is the signal-to-noise ratio, L is the total number of hyperfine lines, T is the temperature measured in Kelvin, and V the sample volume. The S/N ratio in the above equation, can also include in the effects of multiple scans over the same magnetic field region and requires an adjustment of $\sqrt{\text{number of scans}}$. An empirical relationship does not yet exist for the estimating defect concentrations with S $> \frac{1}{2}$. For these defects, transition probabilities between spin states create additional complications in developing a single equation.

Microwaves entering the sample cavity are absorbed by many defects in the bulk single crystal. The small quantity of reflected energy makes accurate detection difficult because spurious signals have the potential to override absorptions of interest. Phase sensitive detection employs the use of lock-in amplifiers to eliminate noise from background absorptions. A small 100 kHz modulation amplitude of the magnetic field, $\mathbf{B_m}$ imposed over the static applied magnetic field, $\mathbf{B}$ has become the standard field modulation frequency.

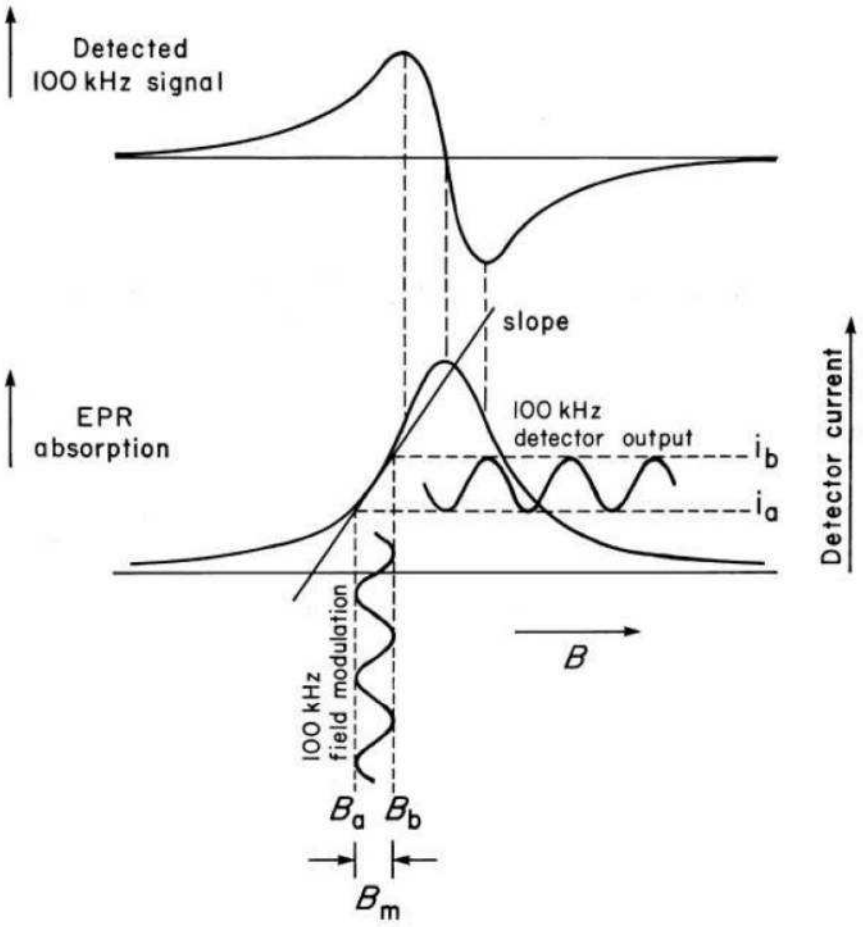

Figure 3.4. Effect of small-amplitude 100 kHz field modulation on the detector output current. In the lower portion of the figure, modulation of the static magnetic field, B occurs between the limits of B_a and B_b. The corresponding detector currents oscillates between limits of i_a and i_b. Shown in the upper portion, the recorded rectified 100 kHz signal as a function on B. Reprinted with permission from [33].

As the applied static magnetic field is slowly varied, this smaller modulation sweeps through a small range of magnetic field values B_a to B_b of the absorption signal, shown in Figure 3.4. The reflected signal from the microwave energy, and field modulation have the same frequency. The absorption signal transforms into a detected sine wave that is displayed as the first derivative with an amplitude that is proportional to the slope of the absorption. If the absorption signal is not approximately linear through the modulation, the detected signal appears distorted on either the peak or trough indicating non-ideal spectrometer settings. A reference signal of the same frequency and phase as the modulation field is provided by the phase sensitive detector. To eliminate extraneous signals, this reference signal combines with the EPR signal creating a DC current that is proportional to the amplitude of the modulated EPR signal. Any signals that differ from the frequency of the DC current are rejected.

Modulation of the magnetic field is provided by a small pair of embedded Helmholtz coils in the walls of the microwave cavity. The choice of modulation frequency is balanced by tradeoffs between the frequency f of the detected signal ('$1/f$' noise, where f is the relevant frequency) and penetrating the microwave cavity inter-walls from the exterior. As a general rule, settling on a 100 kHz modulation frequency has the broadest applicability to EPR problems, and this was the frequency of modulation used in this dissertation.

3.2 FTIR Spectrometer

The principles of optical absorption discussed previously in Chapter 2 are measured using a Fourier transform infrared (FTIR) spectrometer which contains a Michelson interferometer, a light source, and a detector. Figure 3.5 illustrates the relevant

components of a FTIR spectrometer and Michelson interferometer.[1] Light incident from the source can be transmitted, reflected, or absorbed by the bulk single crystals or point defects. Absorption causes attenuation of the light proportional to the sample thickness and is described by Beer's law,

$$I(z) = I_0 e^{-\alpha z} \tag{3.2}$$

where α is the absorption coefficient with units [cm^{-1}] and z (or l) is the sample thickness through which light passes. The absorption coefficient is directly dependent on the incident wavelength and thickness. Often, absorption spectra are expressed in units of optical density (O.D.), or alternatively 'absorbance', which includes sample thickness,

$$O.D. = \log_{10} \frac{I_0}{I(l)} = \frac{\alpha l}{\ln(10)} \tag{3.3}$$

with l the thickness of the sample along the direction of light propagation [39, 66].

To measure the absorption, light from the source travels through the beam-splitter. The beam-splitter sends approximately half the light to a fixed mirror and the other half to a moveable mirror. Adjusting the position of the moveable mirror changes the optical path difference of the two initial beams. This results in light recombining either destructively or constructively. Recombined light travels through the sample and onto a detector [41, 66]. Varying the optical path difference for light produces an interferogram signal at the detector that is a mixture of numerous sine waves. FTIR spectrometers perform a Fourier transform of the interferogram via software packages resulting in an absorption curve reported in wavenumber [cm^{-1}].

The ThermoScientific Nicolet 8700 FTIR spectrometer used in this dissertation has the Ohnic software package for translating the interferogram. Nitrogen purge

[1] A Michelson interferometer uses a beamsplitter, one moving mirror, and a single fixed mirror.

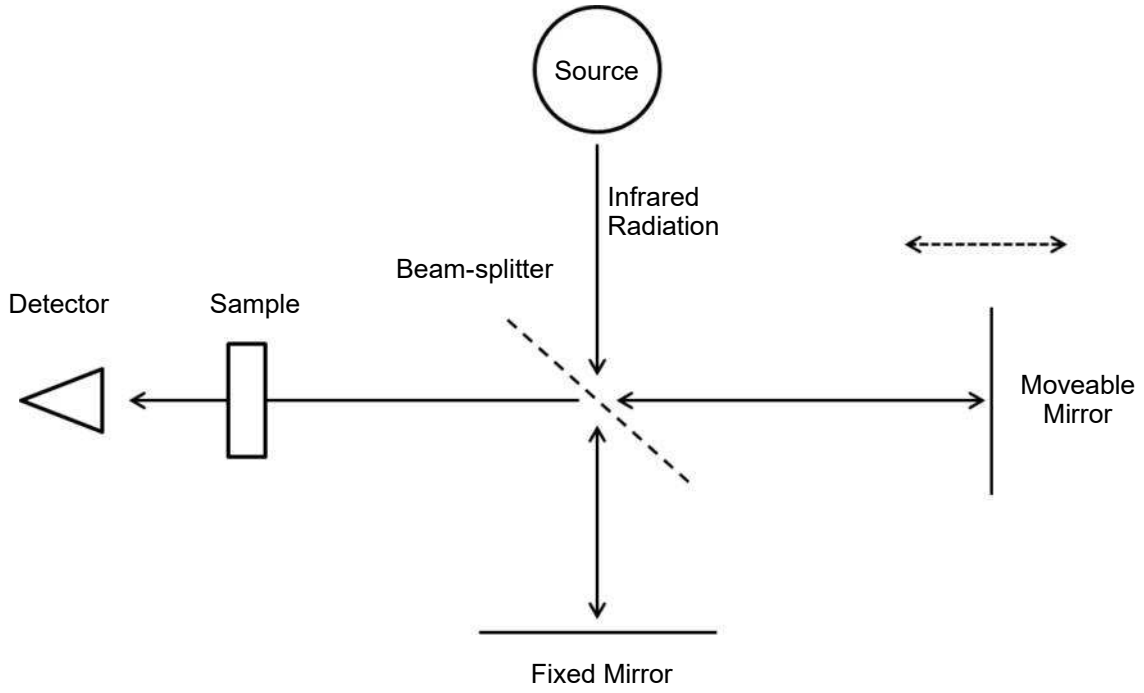

Figure 3.5. Diagram of Fourier-transform infrared spectrometer.

gas flows through the system minimizing infrared atmospheric absorption. The ThermoScientific Nicolet 8700 has a DTGS (deuterated triglycine sulfate) and a CaF_2 beam-splitter and a white light (QTH) source. The DTGS detector has an operational range from 7000 to 350 cm^{-1}, and the QTH light source has a spectral output from 27000 to 2000 cm^{-1}. Polarization of the light was adjusted with an ultra-broadband (250 nm to 4 μm) fused silica wire-grid polarizer from Thorlabs.

Low temperature measurements sharpen absorption curves and were performed using a small, portable dewar. CryoIndustries model ND 110H dewar contains a copper plate "cold-finger" and reservoir for liquid nitrogen. The dewar has two sets of windows which are either SiO_2 or sapphire which are transparent to UV, visible, and infrared light. The copper plate contains two equal apertures: one for the sample mount and the other for low temperature background measurements. A vacuum pump evacuates moisture and air inside in the dewar prior to using liquid nitrogen. The temperature of the "cold-finger" is monitored by a Lakeshore 335 Temperature

Controller, and has an operational range of 80 K - 300 K.

3.3 Thermoluminescent Dosimeter Reader

The instrument used to measure TL is a Harshaw 3500 thermoluminescent dosimeter (TLD) reader, shown in the generic block diagram in Figure 3.6. Samples are

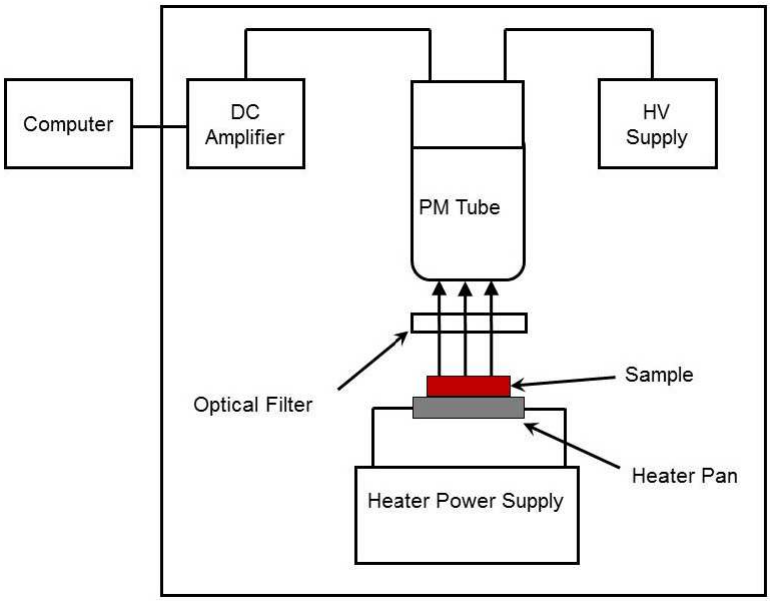

Figure 3.6. Simplified block diagram for a thermoluminescent dosimeter reader.

placed on a resistive heating element connected to a power supply. As the power increases, the temperature of the heating element rises, and light emitted from the sample is directed into a photomultiplier tube (PMT). Light incident on the PMT creates electrons at the photocathode, which are then accelerated and multiplied across dynodes before entering the anode [67]. At the anode, they are converted into a current, which undergoes amplification and is then measured. Measured current is directly proportional to sample light emission, and therefore proportional to the radiation dose absorbed by the sample.

The reported TL data in this dissertation appears as intensity versus temperature, but the Harshaw 3500 software has a limited resolution of 200 channels/bins. Software on the Harshaw 3500 allows adjustments to the starting temperature, T_i, final temperature, T_f, and the total time, δt to ramp from T_i to T_f. The heating rate, β can also be specified, but is interdependent and must be matched with δt. The temperature range corresponding to TL recorded in each channel has the simple expression,

$$\Delta \mathrm{T}_{\mathrm{channel}} = \frac{T_f - T_i}{200} \tag{3.4}$$

This makes comparison of total light intensity for samples with different 'reset' temperatures difficult. Reset temperatures are experimentally determined for individual samples. A sample is considered 'reset' when the effects of radiation or illumination have reversed, returning the sample to its 'as-received' state for defect concentrations from the crystal grower. For this reason, all TL curves are presented as normalized intensity rather than raw or measured intensity.

Due to the sensitivity of the PMT, the detector is shielded internally within the Harshaw 3500 to prevent ambient light from entering the photocathode and causing damage through overexcitation of the photocathode. As an additional protective measure, the Harshaw 3500 is equipped with a neutral density (ND) filter placed between the sample and PMT to reduce incident light intensity [68, 69].

3.4 Wavelength-dependent TL

While the principles and underlying physics of TL outlined in Chapter 2 remain unchanged, an alternate method of radiative recombination detection exists. The more standard method discussed in Section 3.3 only identifies that a radiative recombination center exists for a given temperature, but yields no information on wavelength(s) emitted by the center(s). Combining usage of a heating plate and

spectrograph, obtaining wavelength dependence for a radiative recombination center is possible.

The available heating stage for this work is the INSTEC model HCS621V. The core of the HCS621V is a single stage made of pure silver, due to its thermal conductivity and anti-corrosive properties, upon which samples are placed. The single Ag stage is a 8.5Ω resistive heat stage capable of producing temperatures from ambient up to 600±0.2°C above 100°C. Additionally, the HCS621V can be purged with nitrogen gas to reduce effects of spurious signals resulting from heated air, similar to the Harshaw 3500. Silica fused quartz windows 1.0 mm thick on the top of the HCS621V allow light to escape from the sample and enter the spectrograph via an optical fiber [70].

Measurement of the wavelengths from radiative recombination use the Shamrock 193i spectrograph and iDus420 charge-coupled device (CCD). The internal components of the Shamrock 193i spectrograph are shown in Figure 3.7. Light from the sample on the INSTEC heating stage is collected through a lens at the end of fiber optic cable entering the spectrograph through a side port. Light from the side port is directed by several mirrors, shown as A, before impinging on a diffraction grating, B. The diffraction grating disperses the incoming light onto the focusing mirror, C, which directs the light towards the CCD, shown as D [71]. The Shamrock 193i contains two different diffraction gratings: 150 l/mm and 600 l/mm. In this dissertation, the primary grating used in measurements is 150 l/mm.

The detector in the laboratory configuration is the iDus420 camera which is a silicon based detector with a two-dimensional array of pixels 1024×255. The CCD has thermal-electric cooling reducing detector dark noise over the range of wavelengths $200 - 1100$ nm. The software configuration allows binning the pixels in either the horizontal or vertical directions. While it is possible to use the two-dimensional array for imaging purposes, by vertically binning the pixel, this effectively increases CCD

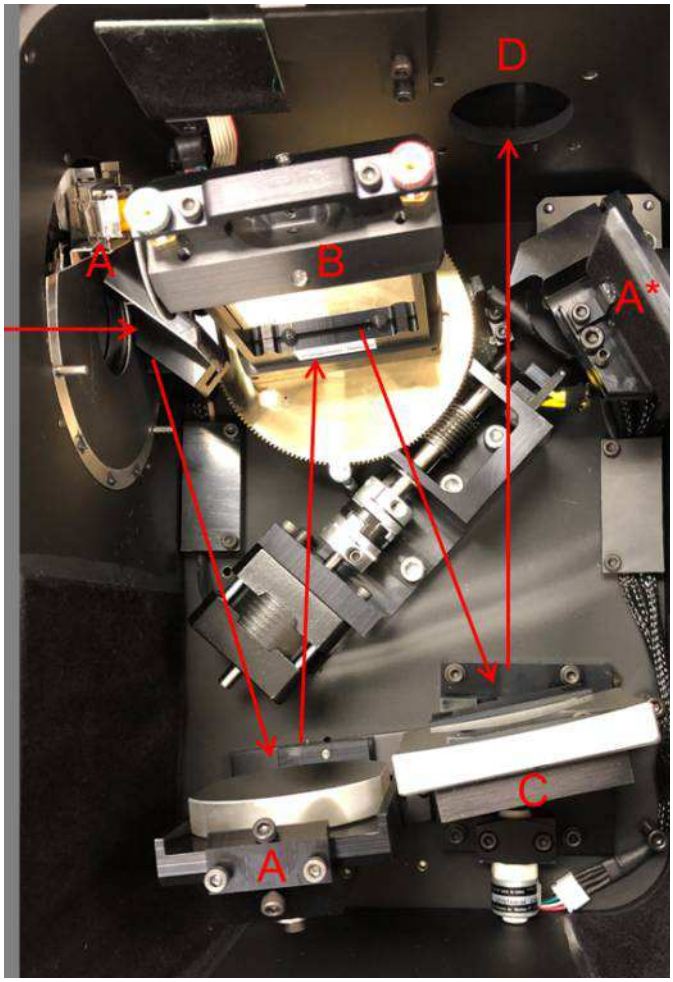

Figure 3.7. Internal components of the Shamrock 193i spectrograph. Light from the side port is directed by several mirrors, shown as A, before impinging on a diffraction grating, B. The diffraction grating disperses the incoming light onto the focusing mirror, C, which directs the light towards the CCD, shown as D.

wavelength dependent efficiency, and maintains a high wavelength resolution when combined with the proper diffraction grating selection. Only vertical binning is used in this dissertation. The exterior window of the camera is UV-grade, AR coated, fuzed silica minimizing light loss due to lens absorption [72].

4. Lithium and Gallium Vacancies in $LiGaO_2$

4.1 Abstract

Lithium gallate ($LiGaO_2$) is a wide-band-gap semiconductor with an optical gap greater than 5.3 eV. When alloyed with ZnO, this material offers broad functionality for optical devices that generate, detect, and process light across much of the ultraviolet spectral region. In the present paper, electron paramagnetic resonance (EPR) is used to identify and characterize neutral lithium vacancies (V_{Li}^0) and doubly ionized gallium vacancies (V_{Ga}^{2-}) in $LiGaO_2$ crystals. These S = 1/2 native defects are examples of acceptor-bound small polarons, where the unpaired spin (i.e., the hole) is localized on one oxygen ion adjacent to the vacancy. Singly ionized lithium vacancies (V_{Li}^-) are present in as-grown crystals, and are converted to their paramagnetic state by above-band-gap photons (x rays are used in this study). Because there are very few gallium vacancies in as-grown crystals, a post-growth irradiation with high-energy electrons is used to produce the doubly ionized gallium vacancies (V_{Ga}^{2-}). The EPR spectra allow establishment of detailed models for the two paramagnetic vacancies. Anisotropy in their g matrices is used to identify which of the oxygen ions adjacent to the vacancy has trapped the hole. Both spectra also have resolved structure due to hyperfine interactions with ^{69}Ga and ^{71}Ga nuclei. The V_{Li}^0 acceptor has nearly equal interactions with Ga nuclei at two Ga sites adjacent to the trapped hole, whereas the V_{Ga}^{2-} acceptor has an interaction with Ga nuclei at only one adjacent Ga site.

4.2 Introduction

Lithium gallate ($LiGaO_2$) is an ultrawide-band-gap semiconductor [15, 73] with a wurtzite-like crystal structure. Its optical absorption edge is in the 5.3-5.7 eV range [19, 74–77]. This material is a ternary analogue of ZnO. Replacing half the

Zn^{2+} ions with Li^{+} ions and half with Ga^{3+} ions in an ordered arrangement gives $LiGaO_2$. Alloying $LiGaO_2$ with ZnO is expected to produce crystals appropriate for ultraviolet optical applications [16, 78, 79]. As suitable shallow donors and acceptors are identified, [80] the $LiGaO_2$ -ZnO mixed materials system will allow laser diodes and photodetectors to be fabricated that operate across much of the ultraviolet region. $LiGaO_2$ is also a candidate for phosphor and radiation-detector applications [14, 81–84]. This ternary material has both monovalent (Li^{+}) and trivalent (Ga^{3+}) cation sites and thus provides a variety of doping possibilities. These include transition-metal ions and rare-earth ions, Group I and Group III isovalent impurities, and Group II and Group IV donors and acceptors. These many doping choices offer broad functionality for diverse applications of $LiGaO_2$ and its alloys with ZnO.

In this work, electron paramagnetic resonance (EPR) is used to investigate native acceptors in $LiGaO_2$ crystals. Similar studies have been reported for $LiAlO_2$ crystals [85, 86]. Spectra from both lithium vacancies and gallium vacancies are observed in the $LiGaO_2$ crystals. In both cases, the hole is localized on one oxygen ion adjacent to the vacancy, in a small-polaron configuration [87, 88]. Anisotropy in the g matrices allows determination of which oxygen ion traps the hole. The V_{Li}^{0} and V_{Ga}^{2-} spectra in $LiGaO_2$ have resolved hyperfine structure due to interactions of the trapped hole with the adjacent ^{69}Ga and ^{71}Ga nuclei. Nearly equal interactions with nuclei at two gallium sites are seen in the V_{Li}^{0} spectrum, whereas interactions with nuclei at only one gallium site are observed in the V_{Ga}^{2-} spectrum. These different hyperfine patterns easily allow the V_{Li}^{0} and V_{Ga}^{2-} spectra to be individually recognized. Although their spectra are obtained at low temperature, the paramagnetic charge states of both vacancies are stable at room temperature. Information about the small-polaron characteristics and the thermal stabilities of these native defects will be useful when searching for acceptor dopants for $LiGaO_2$. Lithium diffusion studies will also benefit

from a spectroscopic method that monitors the presence of lithium vacancies [89,90].

4.3 Experimental

The undoped $LiGaO_2$ crystals used in this study were obtained from the MTI Corporation (Richmond, CA). They were grown by the Czochralski method. Observable concentrations of lithium vacancies were present in some, but not all, of the as-grown $LiGaO_2$ crystals supplied by MTI. By trapping a hole on an adjacent oxygen ion, an irradiation with x rays (60 kV, 30 mA) at room temperature converted the nonparamagnetic lithium vacancies in the as-grown crystals to a paramagnetic charge state that could be observed at low temperature with EPR. The as-grown crystals had very few, if any, gallium vacancies. To investigate this latter defect, a $LiGaO_2$ crystal was irradiated near room temperature with high-energy electrons (1 MeV, 5 μA) from a Van de Graff accelerator at Wright State University. During the irradiation, the crystal was in contact with a water-cooled heat sink to minimize heating by the electron beam. Momentum-conserving displacement events, initiated by the high-energy electrons, produced large numbers of gallium vacancies in the $LiGaO_2$ crystal. The EPR spectra reported in this paper represent approximate defect concentrations of 2.3×10^{18}cm^3 for the V_{Li}^0 acceptors and 1.8×10^{17}cm^3 for the V_{Ga}^{2-} acceptors.

$LiGaO_2$ crystals are orthorhombic (space group $Pna21$), with lattice constants a = 5.402 Å, b = 6.372 Å, and c = 5.007 Å, at room temperature [91]. Figure 4.1 is a ball-and-stick representation of the crystal. The relative x, y, z positions of the ions in Figure 4.1 are given in Table 4.1. In this material, each oxygen ion has two lithium neighbors and two gallium neighbors, each lithium ion has four oxygen neighbors, and each gallium ion has four oxygen neighbors. The Li^+ sites are all equivalent and the Ga^{3+} sites are all equivalent. Oxygen ions occupy two crystallographically inequivalent sites (these are labeled O_I and O_{II} in Fig. 4.1). The two oxygen sites are

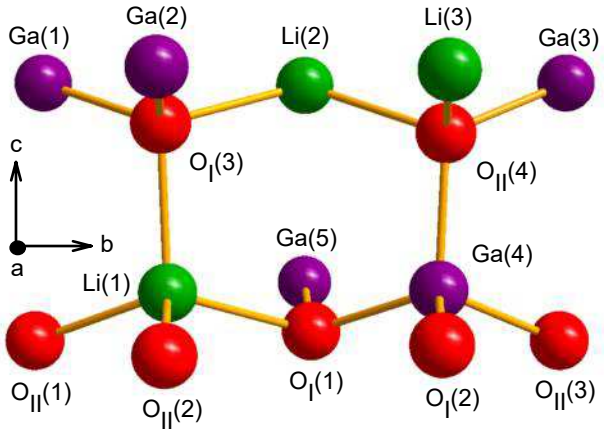

Figure 4.1. Schematic representation of the $LiGaO_2$ crystal structure. Lithium ions are green, gallium ions are purple, and oxygen ions are red. The two inequivalent oxygen sites are labeled O_I and O_{II}. Each lithium and gallium ion has four oxygen neighbors and each oxygen ion has two lithium and two gallium neighbors. Reprinted with permission [38].

most easily distinguished by which cation, a Li^+ or a Ga^{3+} , is the nearest neighbor along the c axis (i.e., the [001] direction). The O_I ions have an adjacent lithium ion in the c direction and the O_{II} ions have an adjacent gallium ion in the c direction. Bonding in $LiGaO_2$ is predominantly ionic allowing application of CFT as discussed in Chapter 2.

The EPR spectra were taken with a Bruker EMX spectrometer operating near 9.40 GHz. A Bruker NMR teslameter was used to measure the static magnetic field and an Oxford helium-gas flow system controlled the sample temperature. The isotropic Cr^{3+} signal (g = 1.9800) in an MgO crystal was used to make corrections for the small differences in magnetic field at the NMR probe tip and the sample position.

4.4 Neutral Lithium Vacancy V^0_{Li}

Figure 4.2 shows the EPR spectrum from the neutral lithium vacancy (V^0_{Li}) in $LiGaO_2$. This spectrum, taken at 55 K with the magnetic field along the c axis, was obtained after an as-received crystal was irradiated at room temperature with

Table 4.1. Relative positions (in units of Å) of ions in $LiGaO_2$, based on the room-temperature lattice parameters reported by Marezio (Reference [92]). The ion labeling scheme in Figure 4.1 is used.

Ion	x	y	z
Li(1)	3.1294	5.5647	4.9750
Li(2)	2.2726	7.1793	7.4785
Li(3)	4.9736	8.7507	7.4785
Ga(1)	2.2575	3.9908	7.5105
Ga(2)	4.9585	5.5672	7.5105
Ga(3)	2.2575	10.3628	7.5105
Ga(4)	3.1445	8.7532	5.0070
Ga(5)	0.4435	7.1768	5.0070
Ga(6)	5.8455	7.1768	5.0070
Ga(7)	4.9585	5.5672	2.5035
$O_I(1)$	2.1965	7.2564	4.4697
$O_I(2)$	4.8975	8.6736	4.4697
$O_I(3)$	3.2055	5.4876	6.9732
$O_{II}(1)$	2.3245	3.9003	4.3601
$O_{II}(2)$	5.0255	5.6577	4.3601
$O_{II}(3)$	2.3245	10.2723	4.3601
$O_{II}(4)$	3.0775	8.8437	4.3601

x rays. Singly ionized lithium vacancies (V_{Li}^{-}) in the as-grown crystal are converted to their paramagnetic neutral charge state (V_{Li}^{0}) during the irradiation. Many of the free electrons and holes created by the x rays quickly recombine. A small portion of the holes, however, are trapped on oxygen ions adjacent to lithium vacancies, thus forming the V_{Li}^{0} centers. A corresponding number of electrons are trapped at unidentified defects (possibly oxygen vacancies or impurities). Heating the crystal above 150 °C destroys the V_{Li}^{0} spectrum and returns the crystal to its pre-irradiated state. A related thermoluminescence (TL) peak is observed near 110 °C in the x-ray irradiated $LiGaO_2$ crystals. This TL peak and its spectral dependence are discussed in detail in Section 4.6.

The $S = \frac{1}{2}$ spectrum from the neutral lithium vacancies (V_{Li}^{0}) consists of a sym-

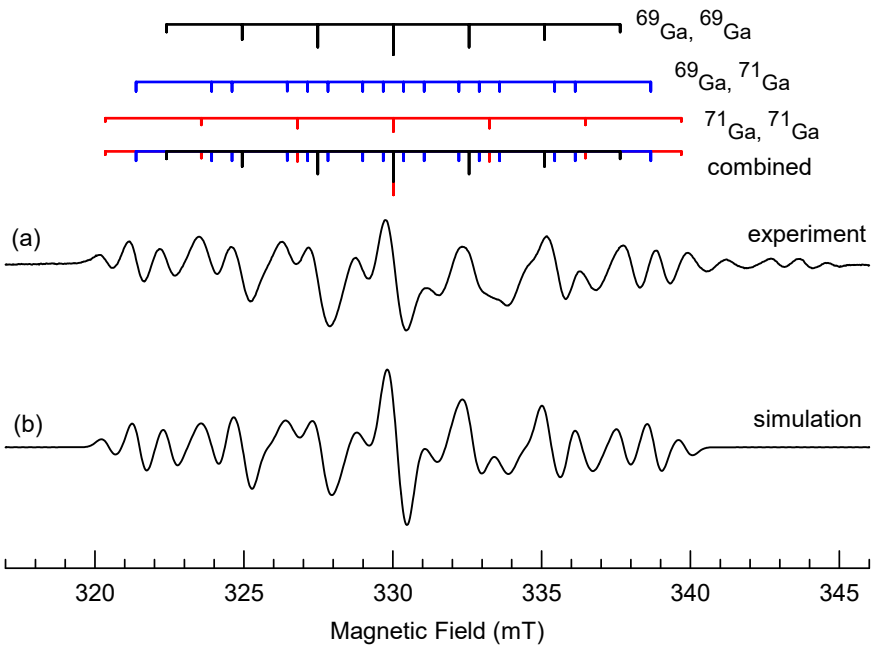

Figure 4.2. (a) EPR spectrum of the neutral lithium vacancy (V_{Li}^{0}) in $LiGaO_2$. The crystal was irradiated at room temperature with x rays, then the spectrum was taken at 55 K with the magnetic field along the *c* direction. The microwave frequency was 9.406 GHz. Stick diagrams illustrate the separate hyperfine contributions from the ^{69}Ga and ^{71}Ga nuclei. (b) Simulated spectrum produced with the SimFonia computer program. Reprinted with permission [38].

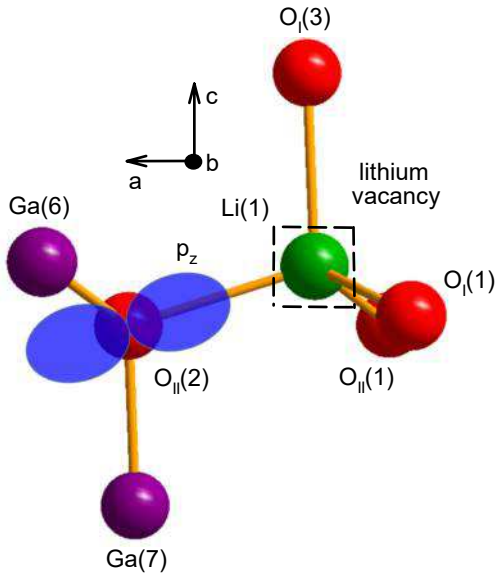

Figure 4.3. Model of the neutral lithium vacancy (V^0_{Li}) in $LiGaO_2$. The trapped hole (shown in blue) is localized in a *p* orbital on the $O_{II}(2)$ oxygen ion with the lithium vacancy at the Li(1) position. Resolved hyperfine from the ^{69}Ga and ^{71}Ga nuclei at the Ga(6) and Ga(7) sites are responsible for the observed hyperfine. Reprinted with permission [38].

metrical pattern of resolved hyperfine lines with differing intensities caused by interactions with ^{69}Ga and ^{71}Ga nuclei. Both isotopes have I = $\frac{3}{2}$ nuclear spins and they are 60.1% and 39.9% abundant, respectively. Their nuclear magnetic moments are $^{69}\mu = +2.0166\beta_n$ and $^{71}\mu = +2.5623\beta_n$. [93] The complicated V^0_{Li} spectrum in Figure 4.2 is explained by having nearly equal hyperfine interactions with Ga nuclei at two gallium sites adjacent to the trapped hole. This is consistent with the defect model since each oxygen ion in $LiGaO_2$ has two Li^+ ions and two Ga^{3+} ions as nearest neighbors. Thus, one Li^+ vacancy, one Li^+ ion, and two Ga^{3+} ions are adjacent to the trapped hole on the oxygen ion. Hyperfine lines from the ^{7}Li nucleus are not resolved in the V^0_{Li} spectrum, whereas lines from the ^{69,71}Ga nuclei are well resolved. This agrees with the model, as atomic calculations [94, 95] predict that the isotropic ^{7}Li hyperfine parameters will be approximately a factor of 30 smaller than the isotropic ^{69,71}Ga parameters when similar amounts of unpaired s-like spin density are on the Li and Ga ions.

With two adjacent sites for Ga, there are three combinations of the two Ga isotopes that contribute to the observed hyperfine pattern in Figure 4.2. These are (i) two ^{69}Ga nuclei, (ii) one ^{69}Ga nucleus and one ^{71}Ga nucleus, and (iii) two ^{71}Ga nuclei. The relative distributions of these three combinations are 36.1%, 48.0%, and 15.9%, respectively. In Figure 4.2, each combination is represented by a stick diagram above the experimental spectrum. Although the hyperfine interactions at the two Ga sites are not exactly equal, the stick diagrams are drawn for equal interactions. The relative lengths of the vertical lines in these diagrams reflect the natural abundances of the two Ga isotopes. The uppermost stick diagram illustrates the seven lines (with relative intensities of 1:2:3:4:3:2:1) that are produced when the unpaired spin interacts equally with two ^{69}Ga nuclei. The lowest stick diagram in Figure 4.2 is the sum of the three upper stick diagrams and should be directly compared to the experimental spectrum. An EPR spectrum with a hyperfine pattern very similar to the V_{Li}^{0} spectrum has been recently reported for the doubly ionized gallium vacancy (V_{Ga}^{2-}) in a β-Ga_2O_3 crystal [5].

Evidence that the hyperfine interactions with the nuclei at the two neighboring Ga sites, although similar, are not equal is found in the relative intensities of the lines in the experimental spectrum in Figure 4.2. If the two Ga sites have equal interactions, the intensity of the middle line in the spectrum should be a factor of 14.3 greater than the intensity of the lowest-field line. The experimental ratio in Figure 4.2, however, is only about 8.5. This observed lower ratio suggests that the center line is slightly split due to inequivalent interactions at the neighboring Ga sites. This splitting is not resolved in the spectrum, but it does significantly reduce the intensity of the center line. The lowest-field line does not split when the two Ga sites have inequivalent interactions. Thus, unlike the center line, its intensity is unaffected by the inequivalency.

The experimental EPR spectrum in Figure 4.2 has a set of underlying weak lines that slightly distort the V_{Li}^0 signals in the magnetic field region above 331.5 mT. This distortion possibly represents a second hole trap site of lower abundance and stability than the dominant V_{Li}^0 oxygen site. Immediately after x ray irradiation, this spectrum severely distorts the EPR spectrum in Figure 4.2. Consequently, Ga hyperfine parameters that describe the c-axis V_{Li}^0 spectrum were obtained from the undistorted low-field side after waiting 30 minutes post x ray irradiation. The lowest line and the middle line in Figure 4.2 are separated by 9.675 mT. According to the ^{71}Ga-^{71}Ga stick diagram, the averaged value of $A_c(^{71}Ga)$ for these nuclei at the two Ga sites is equal to one-third of this separation. [Here, A_c represents the hyperfine interaction for each nucleus when the magnetic field is along the c direction.] This gives an averaged value of 3.22 mT for $A_c(^{71}Ga)$. A corresponding averaged value of 2.53 mT for $A_c(^{69}Ga)$ is obtained using the ratio of magnetic moments. A simulated c-axis spectrum, produced with the SimFonia program from Bruker, is shown in Figure 4.2. In this simulation, the hyperfine interactions at the two neighboring gallium sites are 4% different. The ^{69}Ga and ^{71}Ga parameters used in the simulation were 2.59 and 3.29 mT for one gallium site and 2.49 and 3.16 mT for the other gallium site.

Table 4.2. Parameters describing the EPR spectra of the neutral lithium vacancy (V_{Li}^0) in a $LiGaO_2$ crystal. The oxygen ion trapping the hole has two slightly inequivalent Ga neighbors. A *g* value and the average of the hyperfine parameters for the ^{69,71}Ga nuclei at the two sites were obtained when the magnetic field was along each of the three crystallographic axes. The estimated error is ± 0.0005 for the *g* values and ± 0.05 mT for the hyperfine values.

		Averaged hyperfine parameters (mT)	
Direction of magnetic field	*g* value	^{69}Ga	^{71}Ga
a crystal axis	2.0088	2.43	3.09
b crystal axis	2.0205	2.50	3.18
c crystal axis	2.0366	2.53	3.22

Averaged hyperfine values for the ^{71}Ga-^{71}Ga nuclei at the two Ga sites adjacent to

the trapped hole were also obtained for the V_{Li}^0 acceptor when the magnetic field was aligned along the a and b directions in the crystal. Results for the three directions (a, b, and c) are listed in Table 4.2. For these high-symmetry directions, all crystallographically equivalent orientations of the defect are also magnetically equivalent, and the EPR spectra have their simplest form. Nearly identical hyperfine patterns were observed for each of the three directions of magnetic field, thus establishing the isotropic nature of the Ga interactions. The results in Table II provide direct evidence for the small-polaron model of the acceptor. Specifically, small values for the strength of the Ga hyperfine interactions indicate that only 1.1% of the unpaired spin is in $4s$ orbitals on the two Ga neighbors [93]. This leaves nearly all the remaining unpaired spin density in a p orbital on the oxygen ion. CFT supports this interpretation indicating a nearly complete ionic model/treatment for the localization of spin.

The g values in Table 4.2 were obtained from measurements of the position of the center line in the V_{Li}^0 spectrum when the static magnetic field was along the a, b, and c directions. The small and positive g shifts observed for the V_{Li}^0 acceptor are also consistent with a model that has the unpaired spin (i.e., the hole) located in a p orbital on one oxygen ion adjacent to the lithium vacancy. Acceptor-bound small polarons of this type have been extensively investigated in oxide crystals. [5,85,87,88] The oxygen trapping the hole is an O^- ion with a $2p5$ configuration ($2p_x^2 2p_y^2 2p_z$). The local crystalline electric field removes the threefold orbital degeneracy of this ^{2}P state ($L = 1$, $S = \frac{1}{2}$) and forms three energy levels (E_1, E_2, and E_3). In this simplified picture, E_1 is the ground state with the hole in the p_z orbital and E_2 and E_3 are excited states with the hole in the p_x and p_y orbitals of the ion. The spin-orbit interaction then mixes these excited states with the ground state and gives the following first-order

expressions for the principal g values. [33]

$$g_1 = g_e \tag{4.1}$$

$$g_2 = g_e - \frac{2\lambda}{E_2 - E_1} \tag{4.2}$$

$$g_3 = g_e - \frac{2\lambda}{E_3 - E_1} \tag{4.3}$$

The principal direction corresponding to the g_1 principal value is parallel to the unique axis of the p_z orbital. In these equations, the spin-orbit coupling constant λ for an O^- ion [95] is -135 cm^{-1} and g_e is 2.0023. The positive g shifts (i.e., values greater than 2.0023) reported in Table 4.2 for the V_{Li}^0 acceptor are a result of the negative sign for λ.

The value of 2.0088 for g_a in Table 4.2 is close to 2.0023, which suggests that the p_z orbital containing the unpaired spin is oriented near the a direction in the crystal. Figure 4.3 illustrates the proposed model for the V_{Li}^0 acceptor. The lithium vacancy is at the Li(1) position and the hole is localized on the adjacent $O_{II}(1)$ ion. Nuclei at the Ga(6) and Ga(7) sites are responsible for the resolved hyperfine seen in the EPR spectra. Before lattice relaxation, the Li(1) and $O_{II}(2)$ sites are 1.995 Å apart and the line joining them makes an angle of 18.2° with the a axis of the crystal. The p_z orbital representing the hole, shown in blue in Figure 4.3, is pointing toward the center of the Li vacancy. This orientation of the p_z orbital corresponds to the minimum for the energy of the ground state of the neutral acceptor and establishes the importance of the electrostatic attraction between the positive hole and the "effective" negative charge of the lithium vacancy. The difference between the value of 2.0088 for g_a and an anticipated g_1 value nearer 2.0023 is explained by the relatively small 18.2° angle that the unique axis of the p_z orbital (and thus the principal direction for g_1) makes with the a direction in the crystal. In other words, the measured value of g_a is

slightly greater than 2.0023 because the a direction, although close, is not a principal direction of the g matrix for the V_{Li}^{0} acceptor.

4.5 Doubly Ionized Gallium Vacancy V_{Ga}^{2-}

Figure 4.4(a) shows the EPR spectrum from the doubly ionized gallium vacancy (V_{Ga}^{2-}) in $LiGaO_2$. This spectrum was taken at 93 K with the magnetic field along the c axis. There are six resolved hyperfine lines and g_c is 2.0032. These paramagnetic V_{Ga}^{2-} acceptors were produced by a "knock-on" process in the crystal during an irradiation near room temperature with 1 MeV electrons. A subsequent exposure to ionizing radiation was not needed, as the doubly ionized charge state of the gallium vacancy was thermally stable at room temperature in our crystal.

Similar to the V_{Li}^{0} acceptor, the V_{Ga}^{2-} acceptor has a hole localized on one oxygen ion adjacent to the vacancy. With fewer hyperfine lines than the V_{Li}^{0} spectrum, the experimental V_{Ga}^{2-} spectrum in Figure 4.4(a) is explained by interactions with ^{69}Ga and ^{71}Ga nuclei at only one neighboring Ga site. This is consistent with the defect model since each oxygen ion in the $LiGaO_2$ crystal has two Li^+ ions and two Ga^{3+} ions as nearest neighbors. With one of the gallium ions missing, the oxygen ion with the trapped hole has two neighboring Li^+ ions and one neighboring Ga^{3+} ion. Hyperfine interactions with the adjacent ^{7}Li nuclei are not resolved in the spectrum, whereas interactions with the ^{69,71}Ga nuclei at the one neighboring Ga site are easily observed.

Each Ga isotope has an $I = \frac{3}{2}$ nuclear spin and produces four equally spaced hyperfine lines, as illustrated by the stick diagrams above the experimental spectrum in Figure 4.4(a). Only six lines are resolved in this spectrum because of the strong overlap of the middle lines within each set of four. The difference in the separation of hyperfine lines in the two sets is directly related to the ratio of the nuclear magnetic moments for ^{69}Ga and ^{71}Ga. From the line positions in Figure 4.4(a), it is found

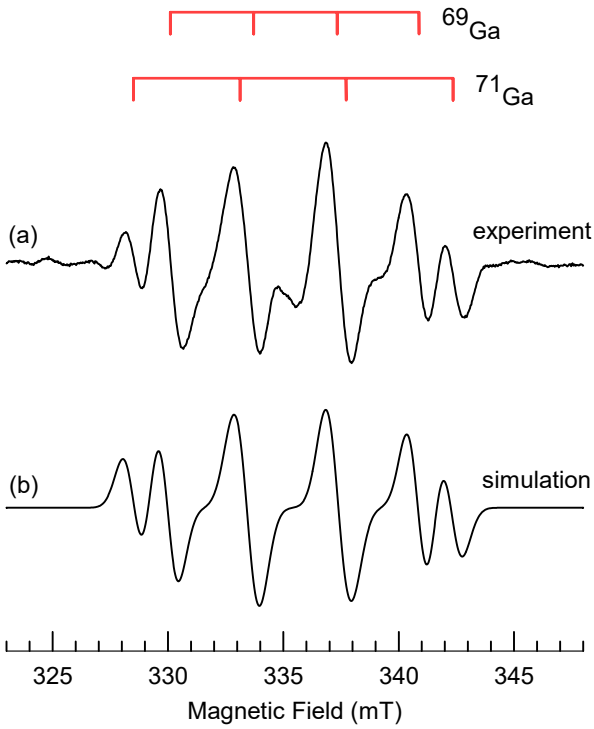

Figure 4.4. (a) EPR spectrum of the doubly ionized gallium vacancy (V_{Ga}^{2-}) in $LiGaO_2$. The crystal was irradiated near room temperature with 1 MeV electrons, then the spectrum was taken at 93 K with the magnetic field along the *c* direction. The microwave frequency was 9.404 GHz. (b) A simulation spectrum produced with the SimFonia computer program. Reprinted with permission [38].

Table 4.3. Parameters describing the EPR spectra of the doubly ionized gallium vacancy (V_{Ga}^{2-}) in a $LiGaO_2$ crystal. The oxygen ion trapping the hole has one Ga neighbor. A g value and the average of the hyperfine parameters for the $^{69,71}Ga$ nuclei at the one site were obtained when the magnetic field was along each of the three crystallographic axes. The estimated error is ± 0.0005 for the g values and ± 0.05 mT for the hyperfine values.

		Averaged hyperfine parameters (mT)	
Direction of magnetic field	g value	^{69}Ga	^{71}Ga
a crystal axis	2.0155	3.75	4.76
b crystal axis	2.0551	3.74	4.75
c crystal axis	2.0032	3.59	4.60

that $A_c(^{69}Ga) = 3.59$ mT and $A_c(^{71}Ga) = 4.60$ mT for the acceptor. Using these results, the simulated c-axis spectrum shown in Figure 4.4(b) was produced with the SimFonia program. Table 4.3 contains the experimental g values and hyperfine parameters for the V_{Ga}^{2-} acceptor when the magnetic field is along the a, b, and c directions. These results show that the ^{69}Ga and ^{71}Ga hyperfine matrices for the V_{Ga}^{2-} acceptor are nearly isotropic.

The anisotropy of the g matrix is used to construct a model for the V_{Ga}^{2-} acceptor. When a hole is trapped on one oxygen ion next to a gallium vacancy, Equations 4.1-4.3 predict that one principal value of the g matrix will be very near 2.0023 and the other two principal values will have small, but positive, g shifts. The value of 2.0032 that is measured for g_c is very close to 2.0023, whereas the values for g_a and g_b are 2.0155 and 2.0551, respectively. This strongly suggests that the p_z orbital containing the unpaired electron spin is aligned along the c direction in the crystal. The model for the V_{Ga}^{2-} acceptor in $LiGaO_2$ is shown in Figure 4.5. The gallium vacancy is at the Ga(4) site and the hole is localized on the adjacent $O_{II}(4)$ ion. Nuclei at the Ga(3) site are responsible for the resolved hyperfine seen in the EPR spectra.

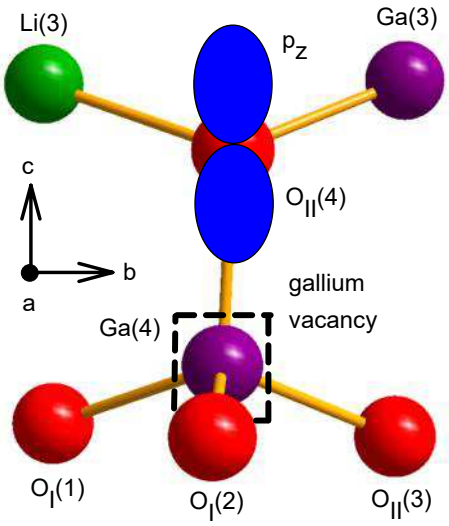

Figure 4.5. Model of the doubly ionized gallium vacancy (V_{Ga}^{2-}) in $LiGaO_2$. The trapped hole (shown in blue) is localized in a *p* orbital on the $O_{II}(4)$ oxygen ion with the gallium vacancy at the Ga(4) position. Resolved hyperfine from the ^{69}Ga and ^{71}Ga nuclei at the Ga(3) site are responsible for the observed hyperfine. Reprinted with permission [38].

4.6 Thermoluminescence Analysis

The TL from irradiating $LiGaO_2$ for 3 min at 30 mA and 60 kV is shown in Figure 4.6. A minimum of four traps are responsible for the two distinct TL peaks and low temperature shoulder.

Fitting of the largest TL peak is accomplished using general order kinetics discussed in Chapter 2.6. An initial assumption for the activation energy, ΔE_a of the main peak at 380° K can be found using a relationship from thermally stimulated current (TSC) studies. In this quasi-equilibrium approach from TSC, several assumptions are necessary:

1. Recombination occuring in the material involves retrapping of emitted carriers by the level under investigation.

2. Initially the level is completely filled.

3. Equilibrium is assumed between the conduction band and the charge trap defin-

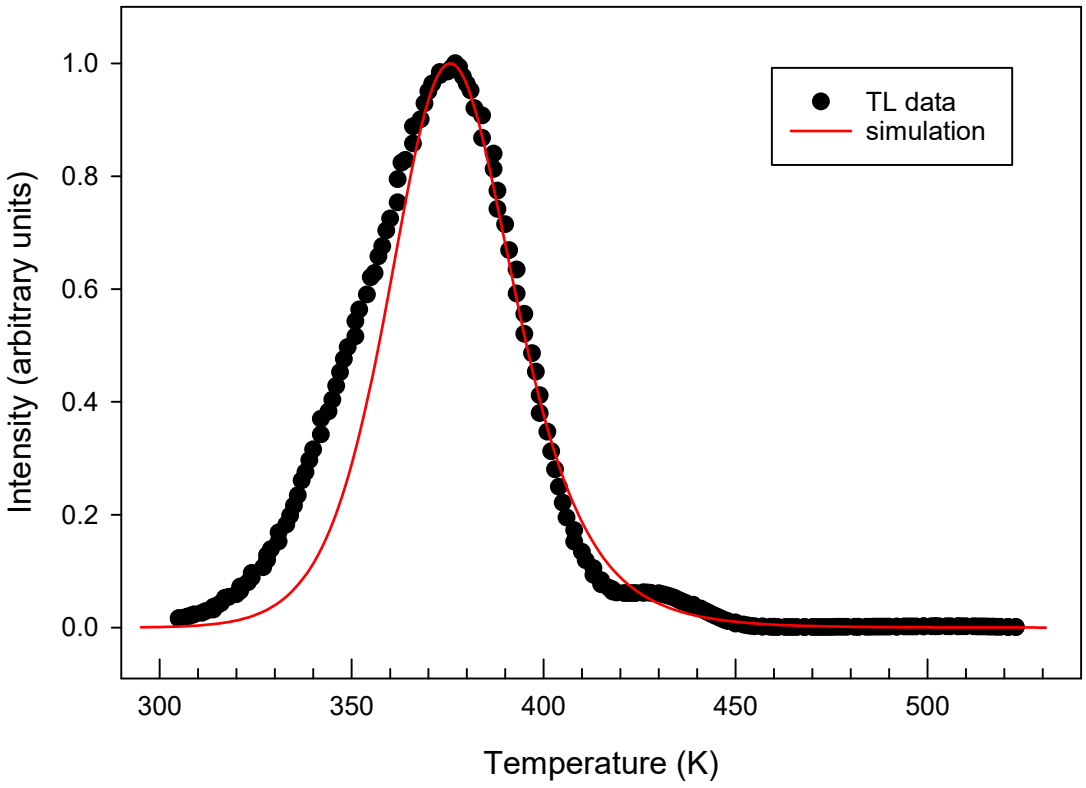

Figure 4.6. Thermoluminescence from $LiGaO_2$ after exposure to 3 min of room temperature x rays at 30 mA and 60 kV, with $\beta = 1.0$ C/s. Simulated TL curve is produced using s $= 10^{12}s^{-1}$, b ≈ 1.99, and $E_a = 1.05$ eV. Reprinted with permission [38].

ing a Fermi level throughout the temperature rise.

4. Peak current is achieved when the Fermi level crosses the trap level.

Using these assumptions, ΔE_a is given by.

$$\Delta E_a = k_B T_m \ln \left[\frac{N_c(T_m)}{n^m} \right] \tag{4.4}$$

where k_B is Boltzmann's constant, T_m is the temperature of peak conductivity, N_c is the effective density of states in the conduction band at T_m, and n^m is the electron concentration at T_m. The relation in this form is not well suited for comparison to TL analysis. Assumptions 2 and 4 are also problematic in that they may not be true for a given system and ΔE_a can be found independent of 4. Removing these assumptions and using an approximation temperature-independent capture cross of 10^{-14} cm^{-2} for n^m of a typical semiconductor reduces the above expression [96]

$$\Delta E_a = 23 k_B T_m. \tag{4.5}$$

This expression is now suited to TL analysis by equating T_m from TSC to where T_m is the temperature at the TL peak's maximum. No information regarding the trap cross sections is experimentally available and to account for a range of possible values from 10^{-12} to 10^{-18} cm^{-2}, the coefficient in front of $k_B T_m$, assumes values 21 - 28. This yields an initial estimate for fitting of $\Delta E_a = 0.8 \pm 0.15$ eV. An iterative approach varies parameters E_a, s, and b from the equation 2.28. The simulated curve shown in Figure 4.6 is produced using $E_a = 1.05$ eV, s = 10^{12}, and b = 1.99.

The spectral dependence of the TL 'glow curve' is shown in Figure 4.7. Luminscence peaks strongly at 375 nm and has a second broader peak from 500 to 800 nm. Small structured features at longer wavelengths have a 100 nm spacing and may represent additional recombination centers.

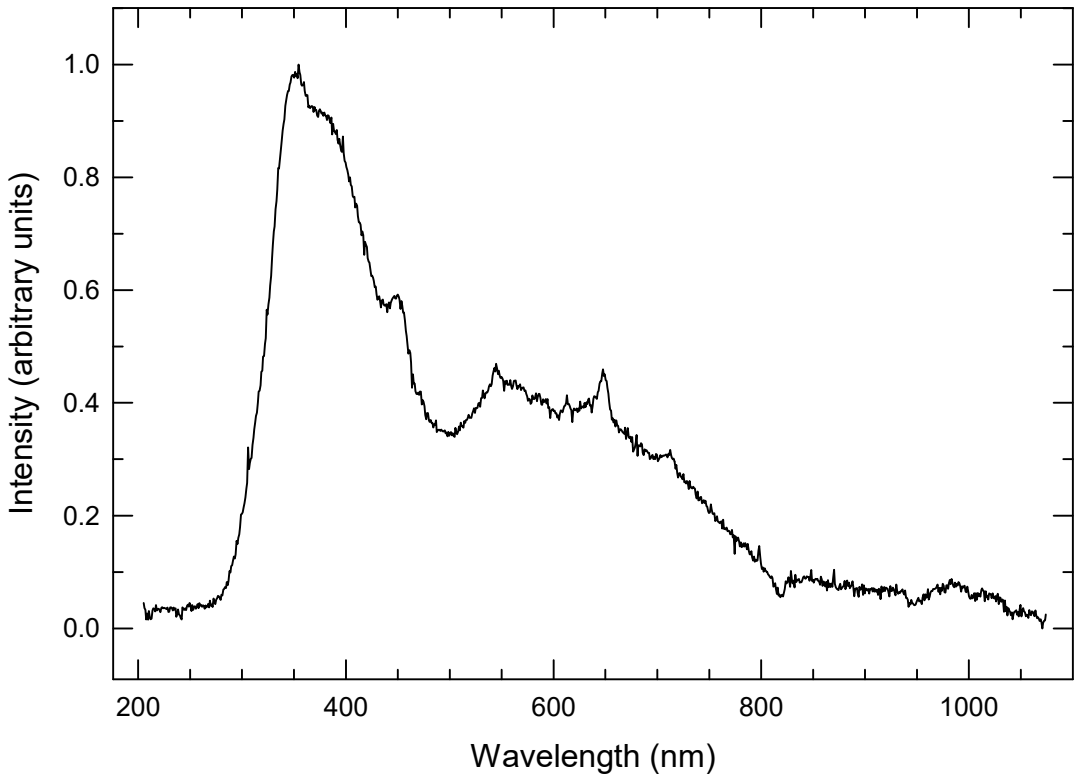

Figure 4.7. Spectral dependence of TL from $LiGaO_2$ after exposure to 3 min of room temperature x rays at 30 mA and 60 kV. The heating rate on the INSTEC remained linear at $\beta = 1.0°$ C/s over a long exposure of 250 s. Several unidentified recombination centers and possible phonon replicas are present in the spectrum.

Deviations between the simulated and measured TL curve shown in Figure 4.6 are explained by considering the data from the wavelength dependence. Data shown in Figure 4.7 is characteristic of at least two recombination centers with different spectral behavior. Parameters from the general order kinetics assume a single electron and hole trap. The simulated 'glow curve' achieves reasonably good agreement on the higher temperature side. A possible explanation for this is a separate weaker TL peak on the lower temperature portion of the spectrum.

As stated earlier, heating the crystal above 150° C destroys the V_{Li}^{0} spectrum and returns the crystal to its pre-irradiated state. self-trapped excitons (STE) have been observed in Ga_2O_3 in the energy range 3.26 to 3.35 eV (370 - 380 nm) [97–100]. In Ga_2O_3 STEs recombine on oxygen sites resulting in blue luminescence. Although it is not clear from the data whether the trapped hole or electron becomes mobile, the similarity in crystal structure provides a possible explanation for the observed luminescence in $LiGaO_2$. The primary TL may result from the release of charge from the trapped electrons recombining on holes trapped next to V_{Li}^{0} . The wavelengths are approximately the same and the dominant recombination center in $LiGaO_2$. Slight distortions of the 375 nm TL peak may be the result of recombination on two different oxygen sites next to V_{Li}^{0} as shown in EPR spectrum in Figure 4.2. The recombination on two different oxygen sites with similar spectral dependence but slightly different activation energies provides an explanation of the differences between the TL data and simulation combined with the ANDOR data. The broader TL peak from 500 to 800 nm is most likely the result of recombination on an unidentified transition metal ion impurity and the source of the weak TL peak at 430 K.

TL and spectral analysis was not performed for the sample containing the V_{Ga}^{2-} EPR spectrum. At present, more than 20 samples of $LiGaO_2$ are in the inventory of the AFIT Condensed Matter Physics EPR laboratory, but only one contains the V_{Ga}^{2-}

spectrum. The effects of heating the sample above room temperature or subjecting it to further radiation are not known. Additionally, the electron irradiation facility at Wright State University used to produce the V_{Ga}^{2-} is no longer available. The V_{Ga}^{2-} is a deep acceptor and its preservation in the sample over years suggests an activation energy > 2 eV below the conduction band minimum. In order to preserve the sample for future studies, TL and spectral analysis should not be conducted until a reliable method for producing multiple samples containing the defect are found.

4.7 Summary

Electron paramagnetic resonance (EPR) has been used to identify and characterize native acceptors in wurtzite-like $LiGaO_2$ crystals. Neutral lithium vacancies (V_{Li}^{0}) and doubly ionized gallium vacancies (V_{Ga}^{2-}) are observed. These defects provide clear examples of acceptor-bound small polarons, where the unpaired spin (i.e., the hole) is localized on one oxygen ion adjacent to the vacancy. Resolved hyperfine structure from neighboring ^{69,71}Ga nuclei and anisotropy in the g matrices are used to construct specific models for these acceptors. In both defects, the hole is located at an O_{II} ion, as it forms the shortest bond with neighboring lithium and gallium ions.

The thermal stability of the paramagnetic charge states of these cation vacancies at room temperature is days for V_{Li}^{0} and more than one year for V_{Ga}^{2-}. This suggests that they are deep levels, as expected for acceptor-bound polarons in oxide crystals. If acceptors such as Mg can be placed on a Ga site in Li-rich, Ga-poor material, their neutral state may also be deep, and thus not useful for devices, because of the formation of similar small polarons. In the search for suitable p-type dopants for $LiGaO_2$, nitrogen ions replacing oxygen ions may be a more likely solution.

5. Ir^{4+} ions in β-Ga_2O_3 An Unintentional Deep Donor

5.1 Abstract

Electron paramagnetic resonance (EPR) and infrared absorption are used to detect Ir^{4+} ions in β-Ga_2O_3 crystals. Mg and Fe doped crystals are investigated and concentrations of Ir^{4+} ions greater than 1×10^{18}cm^3 are observed. The source of the unintentional deep iridium donors is the crucible used to grow the crystal. In the Mg-doped crystals, the Ir^{4+} ions provide compensation for the singly ionized Mg acceptors, and thus contribute to the difficulties in producing p-type behavior. The Ir^{4+} ions replace Ga^{3+} ions at the Ga(2) sites, with the six oxygen neighbors forming a distorted octahedron. A large spin-orbit coupling causes these Ir^{4+} ions to have a low-spin ($5d^5$, S = 1/2) ground state. The EPR spectrum consists of one broad line with significant angular dependence. Principal values of the g matrix are 2.662, 1.815, and 0.541 (with principal axes near the crystal a, b, and c directions, respectively). Ionizing radiation at 77 K decreases the Ir^{4+} EPR signal in Mg-doped crystals and increases the signal in Fe-doped crystals. In addition to the EPR spectrum, the Ir^{4+} ions have an infrared absorption band representing a $d - d$ transition within the t_{2g} orbitals. At room temperature, this band peaks near 5153 cm^{-1} (1.94 μm) and has a width of 17 cm^{-1}. The band is highly polarized: its intensity is a maximum when the electric field E is parallel to the b direction in the crystal and is nearly zero when E is along the c direction.

5.2 Introduction

Ritter et al. [101] have recently reported the presence of Ir^{4+} ions in β-Ga_2O_3 crystals doped with Mg acceptors. In the present paper, electron paramagnetic resonance (EPR) and infrared absorption are used to further characterize this important

impurity in Mg and Fe doped crystals [12,102–108]. The iridium ions are an unintentional deep donor in bulk β-Ga_2O_3 crystals grown with iridium crucibles, by either the Czochralski method or the edge-defined film-fed growth method [109–111]. In n-type crystals, the iridium is present as Ir^{3+} ions. In crystals with a lower Fermi level (e.g., Mg or Fe doped), a portion of the iridium will also be present as Ir^{4+} ions. In semiconductor terms, the Ir^{3+} and Ir^{4+} ions are neutral donors (D^0) and singly ionized donors (D^+), respectively. Based on the similar radii of Ga^{3+}, Ir^{3+}, and Ir^{4+} ions in sixfold coordinated sites, [112] the iridium ions in β-Ga_2O_3 crystals are expected to be located at the octahedral Ga(2) positions. The Ga(2) location of the Ir ions is also supported by computational studies [101].

The Ir^{4+} ions are unique and especially interesting in β-Ga_2O_3 . They have the $[Xe]4f^{14}5d^5$ configuration. In their distorted octahedral environment, a large spin-orbit coupling and a strong crystal field cause the Ir^{4+} ions to have a low-spin ($S = 1/2$) ground state, as the five d electrons are placed in the three t_{2g} orbitals ($\uparrow\downarrow\uparrow\downarrow\uparrow$) [31]. This gives rise to an anisotropic EPR signal and also produces an infrared absorption signal when an electron is promoted from one orbital to another within the three t_{2g} orbitals. In contrast, the Ir^{3+} ($5d^6$) ions have no EPR signal as there are three sets of paired d electrons in the t_{2g} orbitals. In the early years of paramagnetic resonance, EPR spectra from Ir^{4+} ions played an important role when the conceptual understanding of low-spin d^5 octahedral complexes and the sharing of spin density (i.e., covalency) with neighboring ions was being developed [59,62,113,114]. Recently, the study of Ir^{4+} ions in iridate compounds such as Sr_2IrO_4 have revealed new and unusual properties of matter caused by the combined effects of strong spin-orbit and Coulomb interactions [55–58].

Iridium is a significant donor in β-Ga_2O_3 crystals grown in iridium crucibles, as this impurity provides a deep level that affects the electrical and optical properties of

the material. In the present paper, we investigate the EPR and infrared absorption properties of Ir^{4+} ions in this wide-band-gap semiconductor. The complete angular dependence of the S = 1/2 EPR spectrum is acquired, thus establishing the principal values and principal directions of the g matrix. The temperature dependence and polarization properties of the 5153 cm^{-1} infrared absorption band are also determined. Correlations of the intensities of the EPR spectrum and the infrared absorption band in both Mg and Fe doped samples verify that these spectral features have a common origin. Combining the EPR and infrared results allows an oscillator strength to be estimated for the absorption band. A change in the concentration of Ir^{4+} ions occurs when a crystal is exposed to above-band-gap photons (i.e., ionizing radiation) while at or near 77 K. X rays are used in this study for convenience, but near-band-edge light from a lamp or a laser is expected to be equally effective. The ionizing radiation at 77 K causes the Ir^{4+} EPR signal to decrease in Mg-doped crystals and to increase in Fe-doped crystals. Subsequent warming to near or slightly above room temperature, respectively, restores the pre-irradiated intensities.

5.3 Experimental

The bulk β-Ga_2O_3 crystals used in the present investigation were grown by the Czochralski technique with iridium crucibles. Crystals doped with Mg were obtained from Synoptics (a Northrop Grumman company in Charlotte, NC). The starting material contained approximately 0.20 mol.% of MgO. Crystals doped with Fe were provided by Kyma Technologies (Raleigh, NC) and had 0.01 mol.% of Fe_2O_3 added to the starting materials. The samples were rectangular b plates, approximately 3×4 mm^2 with thickness ranging from 0.36 to 1.4 mm. EPR and infrared absorption spectra were obtained from four samples (two Mg-doped and two Fe-doped), thus allowing a correlation study. An EPR spectrum from Fe^{3+} ions is present in all the

samples, very intense in the Fe-doped samples and smaller, yet easily detected, in the Mg-doped samples. The a, b, and c crystal directions for each sample were verified using the angular dependence of the Fe^{3+} EPR spectrum [115]. Errors in aligning the crystals in our experiments were less than 5°.

A Bruker EMX spectrometer operating near 9.39 GHz was used to take the EPR spectra. Magnetic fields were measured with a Bruker NMR teslameter and the temperature of the sample was controlled with an Oxford helium-gas flow system. Estimates of the concentration of defects contributing to an EPR spectrum, valid to within a factor of two, were based on comparisons to a standard pitch sample provided by Bruker. A Varian OEG-76H-Rh tube operating at 60 kV and 30 mA was used for the x-ray irradiations. Infrared absorption spectra were taken with a ThermoScientific Nicolet 8700 FTIR spectrometer. A white-light (QTH) source, a CaF_2 beam splitter, and a DTGS detector were used, along with an ultra-broad-band (250 nm to 4 μm) fused-silica wire-grid polarizer from Thorlabs (Model WP25M-UB). A liquid-nitrogen cryostat with sapphire windows from Cryo Industries (Model 110-637-DED) and a LakeShore (Model 335) controller were used to take the low-temperature infrared absorption data. Effects of surface losses have been removed from the absorption spectra shown in this paper.

5.4 EPR Results

Figure 5.1 shows the EPR spectrum obtained at 30 K from an Mg-doped β-Ga_2O_3 crystal. The magnetic field is along the b direction in the crystal and the microwave frequency is 9.393 GHz. Five intense lines are observed. The broad line at 369.9 mT is assigned to Ir^{4+} ions, while lines at 165.7, 305.1, 607.1, and 1341.8 mT are due to Fe^{3+} ions. Neutral Mg acceptors (Mg^0_{Ga}) are not present in the spectrum in Figure 5.1, as these acceptors [12] are all compensated and thus in their singly ionized

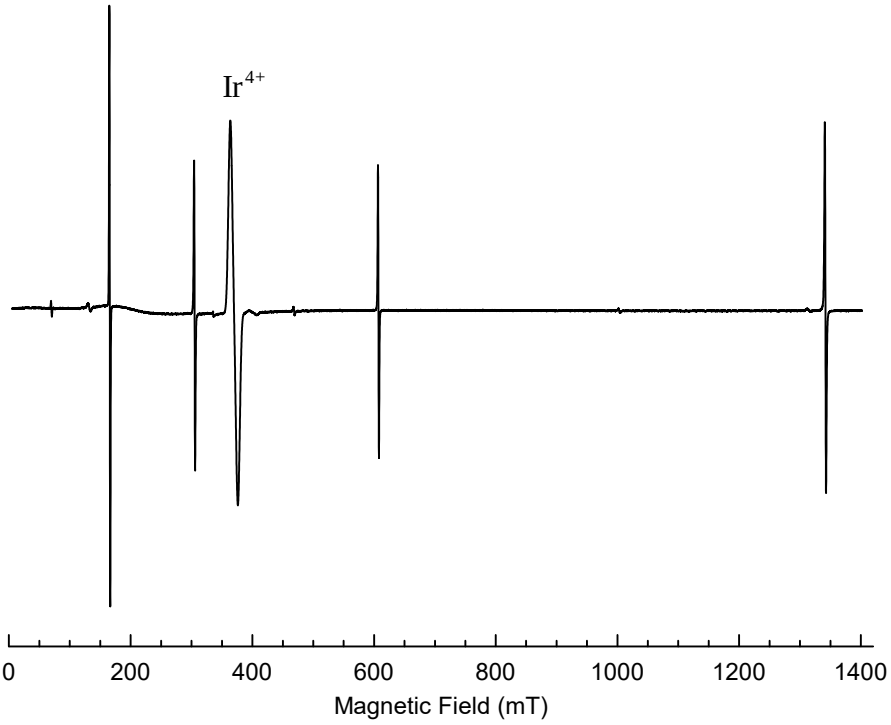

Figure 5.1. EPR spectrum taken at 30 K from an Mg-doped β-Ga_2O_3 crystal. The magnetic field is along the b direction and the microwave frequency is 9.393 GHz. The Ir^{4+} line is at 369.9 mT. The other four sharper lines are from the S = 5/2 Fe^{3+} ions. Reprinted with permission [36].

charge state (Mg_{Ga}^{-}). Large zero-field splittings, comparable in energy to our 9.39 GHz microwave photons, are responsible for the complex Fe^{3+} spectrum [115]. These Fe^{3+} ($3d^5$) ions have the high-spin S = 5/2 ground state, with the B2 and B4 coefficients for the Stevens operators in the monoclinic spin Hamiltonian having large values. This causes multiple Fe^{3+} lines, as the distinction between allowed and forbidden transitions is no longer valid. Also, significant shifts in the positions of lines occur when the direction of the magnetic field is changed. In contrast, the Ir^{4+} ($5d^5$) ions have the low-spin S = 1/2 ground state. As shown in Figure 5.1, the EPR spectrum of the Ir^{4+} ions in β-Ga_2O_3 crystals is much simpler with only an $M_S = +1/2$ to $-1/2$ transition. The concentration of ions responsible for the Ir^{4+} EPR signal in Figure 5.1 is estimated to be approximately $7.0 \times 10^{18}cm^3$. [Note that the linewidth of the Ir^{4+} signal is about 12.0 mT, whereas the linewidths of the Fe^{3+} signals are about 1.5 mT.] Above 115 K, the Ir^{4+} EPR signal broadens because of a short spin-lattice relaxation time. Below 20 K, a long spin-lattice relaxation time causes the Ir^{4+} line to show signs of saturation with increasing microwave power. During our study, we did not observe an EPR spectrum that could be assigned to Ir^{2+} ($5d^7$) ions. Spectra from Ir^{2+} ions, however, have been reported in other materials [116, 117].

Figure 5.2 shows the angular dependence of our Ir^{4+} EPR spectrum. The position of the line was measured at 5° intervals as the direction of the magnetic field was rotated in the $a - b$, $b - c$, and $c - a^*$ planes, where the b direction is normal to the mirror plane. Because a and c are 103.8° apart in these crystals, [3, 4] a^* and c^* directions are introduced (a^* is perpendicular to b and c whereas c^* is perpendicular to a and b) [35]. The space group for monoclinic β-Ga_2O_3 is C2/m, thus allowing for two distinct, crystallographically equivalent, orientations of the principal axes of the g matrix for point defects located at sixfold Ga(2) sites. There are two cases to be considered, since these two orientations of the g matrix may or may not be

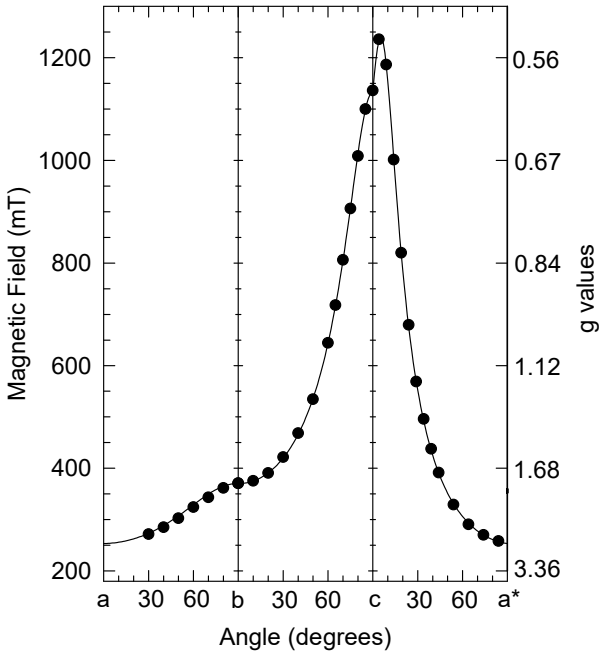

Figure 5.2. Angular dependence of the Ir^{4+} EPR spectrum in a β-Ga_2O_3 crystal. Data were taken in the $a-b$, $b-c$, and $c-a^*$ planes. The discrete points are experimental results, and the solid lines are computer-generated using the g values listed in Table 5.1. Magnetic field values along the left vertical axis correspond to a microwave frequency of 9.401 GHz. Reprinted with permission [36].

magnetically equivalent. In the first case, where the principal axes of the g matrix are along arbitrary directions, the two orientations of the g matrix will be magnetically equivalent when the magnetic field is aligned along the a, b, or c directions and at all angles in the $a-c$ plane (i.e., the mirror plane) and will not be magnetically equivalent when rotating in the $a-b$ and $b-c$ planes. This results in a single line in the $a-c$ plane and two distinct lines in the $a-b$ and $b-c$ planes. Site splitting of this type in a monoclinic material has been seen in the angular dependence of Sb^{2+} ($5s^2 5p^1$) impurity ions at Sn sites in photorefractive $Sn_2P_2S_6$ crystals [118]. In the second case, where the principal axes of the g matrix are along the a, b, and c directions, the two orientations of the g matrix are always magnetically equivalent and a single line will be observed in all three planes of rotation. Our experimental results in Figure 5.2, with no detectable splittings in the $a-b$ and $b-c$ planes, correspond to this second case, thus indicating that the principal-axis directions of the g matrix for the Ir^{4+} ions must be near the crystals a, b, and c directions.

As illustrated by the angular dependence in Figure 5.2, the Ir^{4+} ions have a highly anisotropic g matrix. The EPR line moves from a low magnetic field of 253 mT to a high field of 1235 mT during the rotations. Turning points near a and c identify two of the principal-axis directions of the g matrix, with the third principal axis along the b direction (i.e., perpendicular to the mirror plane). A spin Hamiltonian with an electron Zeeman term ($H = \beta \mathbf{S} \cdot \mathbf{g} \cdot \mathbf{B}$) describes the angular dependence and allows the four parameters that define the g matrix to be determined. In the a, b, c^* coordinate system, these parameters are the three diagonal elements and one off-diagonal element. The 45 discrete points in Figure 5.2, along with their corresponding microwave frequencies, were used as input data for a "least-squares" fitting procedure. The energy eigenvalues of the 2×2 spin Hamiltonian matrix were repeatedly calculated as the g-matrix parameters were systematically varied during

the fitting process. Best-fit values for the four parameters are given in Table 5.1. Final principal g values and principal-axis directions (X, Y, Z) were obtained when the upper matrix in Table 5.1 was diagonalized. The solid curves in Figure 5.2 were generated using these final parameters. Our g values for the Ir^{4+} ions in β-Ga_2O_3 crystals are similar to those reported for Ir^{4+} ions in TiO_2 (see Table 5.1) [119].

Table 5.1. Parameters describing the g matrix for Ir^{4+} in β-Ga_2O_3 crystals. The g matrix is first given in the a, b, c^* coordinate system, and then in its diagonal form. Principal-axis directions are specified by a polar angle Θ and an azimuthal angle Φ. The polar angle Θ is defined relative to the c^* direction and the azimuthal angle Φ is defined relative to the a direction with positive rotation from a toward b in the c^* plane.

		g matrix (in a, b, c^* coordinate system)	
	2.644	0	-0.195
		1.815	0
			0.559
		Principle values	
	g_{xx}	g_{yy}	g_{zz}
	2.662	1.815	0.541
		Principle directions	
	X	Y	Z
Θ	95.3°	90.0°	5.3°
Φ	0°	90.0°	0°
	g matrix (principle values) for Ir^{4+} ions in rutile TiO_2 (from [119])		
	2.397	1.707	0.418

The average of our three principal g values for Ir^{4+} in β-Ga_2O_3 is 1.673. Sharing of the Ir^{4+} d electrons with the six neighboring oxygen ions (and also with the Ga ions beyond these six oxygen ions) is responsible for this averaged g value being considerably less than the free spin value of 2.0023 [31, 59, 62, 113, 114]. If an Ir^{4+} ion is located at the center of a perfect (i.e., cubic) octahedron, the g matrix will be isotropic. The observed anisotropy in the g matrix with large shifts of the three principal values from the averaged value indicates that, as expected, the oxygen octahedron surrounding the Ir^{4+} ion is significantly distorted in the monoclinic β-

Ga_2O_3 crystal. The following equations describe the g values of an Ir^{4+} ion in a low symmetry site [31, 114, 120, 121].

$$g_z = \cos^2\theta\left\{g_e \sin^2\alpha - (g_e + 2k)\cos^2\alpha\right\} + (2k - g_e)\sin^2\theta \tag{5.1}$$

$$\frac{1}{2}(g_x + g_y) = -\cos^2\theta\left\{g_e \sin^2\alpha + 2\sqrt{2}k\cos\alpha\sin\alpha\right\} \tag{5.2}$$

$$\frac{1}{2}(g_x - g_y) = \sin 2\theta\left\{g_e\cos\alpha + \sqrt{2}k\sin\alpha\right\} \tag{5.3}$$

$$\tan(2\alpha) = \frac{2\sqrt{2}\lambda}{\lambda - 2\Delta} \tag{5.4}$$

In equations (5.1 to 5.3), k is the orbital reduction factor (an indicator of covalency) and α and θ describe the linear combination of d orbitals that form the ground state doublet of the Ir^{4+} ion. In equation (5.4), λ is the spin-orbit coupling constant and Δ is the infrared absorption energy. As discussed in reference [114], there are two choices for the relative signs of g_x, g_y, and g_z. [Note that these signs are not experimentally determined.] We find that the following relative signs ($g_x = -2.662$, $g_y = -1.815$, and $g_z = +0.541$) give realistic values for the three Ir^{4+} parameters k, α, and θ in β-Ga_2O_3 . Our best-fit results using equations (5.1-5.3) are:

$$k = 0.646; \quad \alpha = 58.5^\circ; \quad \theta = -6.7^\circ$$

The small value for k reinforces our expectation that there is significant sharing of the d electrons with the six neighboring oxygen ions. Equation (5.4) provides a connection between the EPR spectrum and the infrared absorption peak position and allows us to determine a value for λ. Using $\alpha = 58.5^\circ$ and $\Delta = 5153\text{cm}^{-1}$ from Section 5.5 gives $\lambda = 4215\text{cm}^{-1}$. This value for λ is within the range of 3000 to 4500 cm^{-1} often invoked for Ir^{4+} ions [119, 122, 123].

Many of the EPR spectra reported for Ir^{4+} ions in various materials have resolved

hyperfine structure from the ^{191}Ir and ^{193}Ir nuclei [124–127]. These isotopes have I = 3/2 nuclear spins and similar nuclear magnetic moments [91]. Their natural abundances are 37.3% and 62.7%, respectively. In all reported cases, the hyperfine matrices are nearly isotropic, with principal values (in energy units) near 25×10^{-4}cm^{-1}. The EPR line in Figure 5.1 from the Ir^{4+} ions is very broad, approximately 12.5 mT, with no resolved hyperfine structure from ^{191}Ir and ^{193}Ir nuclei. This lack of resolved hyperfine lines in the β-Ga_2O_3 Ir^{4+} spectrum is not surprising. In addition to a broadening of the four expected lines as a result of superhyperfine interactions with the nearest ^{69,71}Ga nuclei, the nuclear electric quadrupole interactions for the ^{191,193}Ir nuclei must also be considered. Large nuclear electric quadrupole moments for the ^{191,193}Ir nuclei [91] and a large electric field gradient at the Ga(2) sites in this low-symmetry crystal will cause the Ir^{4+} ions in β-Ga_2O_3 to have a complex hyperfine pattern consisting of strongly overlapping allowed and forbidden lines. This, together with the Ga superhyperfine interactions, produce the observed broad, nearly structureless EPR line. We attribute the very slight distortion at the mid-point of the Ir^{4+} EPR line, when the magnetic field is along the b direction, to underlying hyperfine structure (see Figure 5.6 and 5.7). The EPR spectra from Ir^{4+} ions in MgO and CaO crystals have been fully analyzed and the effects of large nuclear quadrupole interactions have been clearly illustrated [124]. We anticipate that future electron-nuclear double resonance (ENDOR) experiments will provide similar complete sets of ^{191,193}Ir hyperfine parameters for Ir^{4+} ions in β-Ga_2O_3 crystals.

5.5 Infrared Absorption Results

Figure 5.3 shows the infrared absorption spectrum from Ir^{4+} ions in an Mg-doped β-Ga_2O_3 crystal. This infrared band, first observed by Ritter et al., [101] is a $d-d$ transition within the t_{2g} orbitals of the low-spin Ir^{4+} ions. Similar sharp absorption

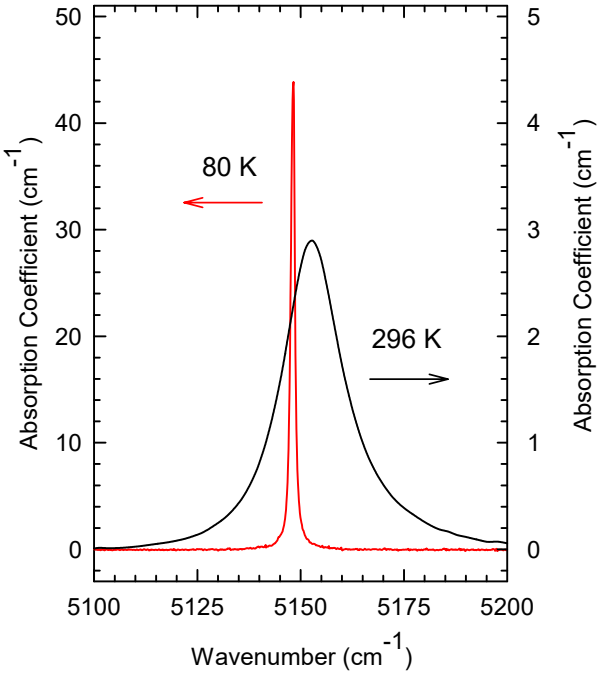

Figure 5.3. Infrared absorption band from Ir^{4+} ions in an Mg-doped β-Ga_2O_3 crystal. Spectra were obtained at room temperature (black curve) and at 80 K (red curve). Light propagated along the b direction with the electric field vector E along the a direction. Reprinted with permission [36].

bands in the 4500 to 5300 cm^{-1} region have been reported in the past for Ir^{4+} ions in various host crystals [119, 122, 125, 128, 129]. As illustrated in Figure 5.3, the width and thus the intensity of this band in β-Ga_2O_3 is strongly temperature dependent. At room temperature, the band peaks at 5153 cm^{-1} (1.94 μm) and its FWHM is 17 cm^{-1}. The band sharpens as the temperature is lowered. At 80 K, the peak shifts to 5148.1 cm^{-1} and the FWHM reduces to 1.2 cm^{-1}. In Figure 5.3, the right vertical scale goes with the room temperature spectrum and the left vertical scale goes with the 80 K spectrum. The Ir^{4+} absorption band in Figure 5.3 has a Lorentzian shape and represents a weakly allowed electronic transition. Vibronic structure near the main peak was not observed.

Figure 5.4 shows that the 5153 cm^{-1} infrared absorption band is polarized. The maximum intensity occurs when the electric field vector E of the incident light is parallel to the b direction in the crystal. With the electric field E near c^*, the intensity of this absorption band decreases to near zero. Figure 5.5 shows the change in the intensity of the infrared absorption band as the direction of the electric field is varied from a to c^*. The solid curve in Figure 5.4 is generated using $I(\theta) = A + Bcos2\theta$ for the intensity (i.e., the transition probability) of the absorption band, [42] where $\theta = 0^\circ$ when E is along a and $\theta = 90^\circ$ when E is along c^*.

Table 5.2. Correlation of the infrared absorption band and EPR signal from Ir^{4+} ions in β-Ga_2O_3 crystals. The Mg-doped crystals are labeled Mg1 and Mg2 and the Fe-doped crystals are labeled Fe1 and Fe2. Values are given for the thickness (i.e., optical path length), volume, absorption coefficient α of the infrared peak at room temperature for E along the a direction, and the concentration N obtained from the EPR signal.

sample	thickness (mm)	volume (mm^3)	absorption coefficient $\alpha(cm^{-1})$	concentration from EPR $N(10^{18}cm^{-3})$	N/α $(10^{18}cm^{-2})$
Mg1	1.19	14.5	2.90	7.0	2.4
Mg2	1.41	12.0	2.77	6.0	2.2
Fe1	0.36	4.6	0.46	1.2	2.7
Fe2	0.38	4.2	0.43	1.0	2.3
				average $N/\alpha = 2.4$	

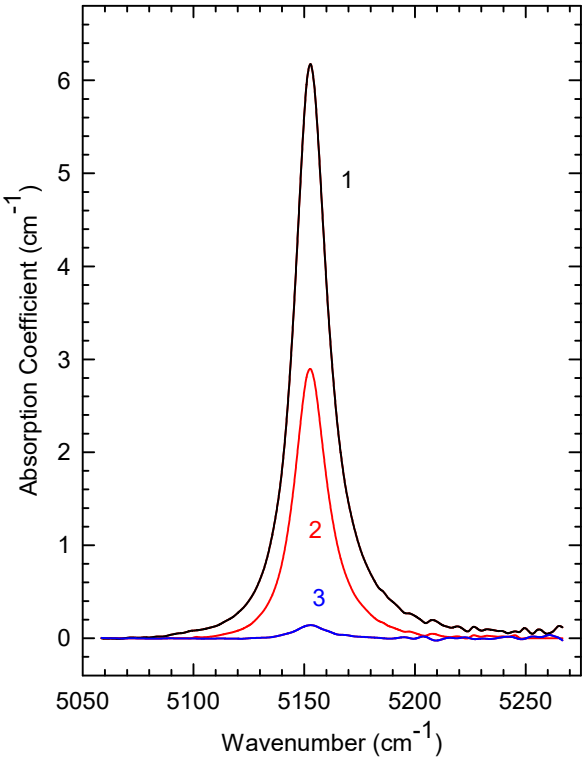

Figure 5.4. Polarization dependence of the infrared absorption band from Ir^{4+} ions in an Mg-doped β-Ga_2O_3 crystal. These spectra were taken with the electric field E along the b direction (spectrum 1), the a direction (spectrum 2), and the c direction (spectrum 3). Light propagated along the c direction for spectrum 1 and the b direction for spectra 2 and 3. Reprinted with permission [36].

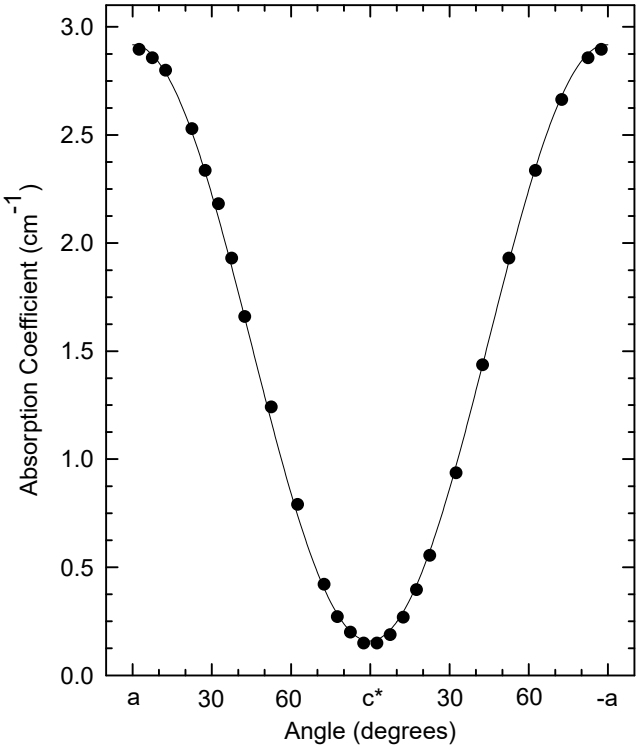

Figure 5.5. Intensity of the Ir^{4+} infrared absorption band in an Mg-doped β-Ga_2O_3 crystal when the direction of the electric field E is rotated from a to c^* in the crystal. The solid line represents a $\cos 2\theta$ dependence. Reprinted with permission [36].

A primary result of the present study is the correlation of the intensities of the EPR signal and the infrared absorption peak for Ir^{4+} ions in β-Ga_2O_3 . Data were obtained from four crystals. Two are Mg-doped (labeled Mg1 and Mg2) and two are Fe-doped (labeled Fe1 and Fe2). The results are presented in Table 5.2. The third column is the room-temperature absorption coefficient α for the 5153 cm^{-1} infrared band. These values were acquired with light propagating along the b direction and the electric field E along the a direction. The fourth column is the concentration N of Ir^{4+} ions obtained from EPR spectra taken at 40 K with the magnetic field along the b direction. Larger values of α and N are expected for the Mg-doped crystals since a greater portion of the iridium ions are in the 4+ charge state when Mg acceptors are present. In the fifth column of Table 5.2, the ratios of N and α for the four crystals are used to determine if a correlation exists. As can be seen, this ratio is very nearly the same for the four samples, thus providing evidence that the infrared absorption band and the EPR line are from the same defect. The deviations from the average value of $2.4 \times 10^{18} cm^{-2}$ for the N/α values in Table 5.2 are less than 9%. In future investigations, if one of the two quantities N or α is known, then the other can be estimated using the equation $N = [2.4 \times 10^{18} cm^{-2}]\alpha$.

Combining EPR and optical absorption data from the same crystal allows us to determine an oscillator strength f for the Ir^{4+} infrared absorption band. The EPR spectrum in Figure 5.1 and the room-temperature absorption spectrum in Figure 5.4 were taken from the same Mg-doped crystal (referred to as crystal Mg1 in Table 5.2). Smakula's equation, given in equation 5.5 for a Lorentzian line shape, relates the product of defect concentration N and oscillator strength f to the intensity and FWHM of the absorption band and the index of refraction n of the material [43, 130].

$$Nf = \left(1.29 \times 10^{17}\right) \frac{n}{(n^2+2)^2} \alpha_{\max} W \tag{5.5}$$

The concentration N of Ir^{4+} ions from the EPR spectrum in Figure 5.1 is 7.0×10^{18} cm^{-3}, and α_{max} and W from the maximum absorption data in Figure 5.4, taken with the electric field along the b direction, are 6.2 cm^{-1} and 2.2 meV, respectively. Near the 1.9 μm position of the peak, the index of refraction n of β-Ga_2O_3 is 1.9 [131]. Substituting these quantities into equation 5.5 gives an oscillator strength $f = 1.5 \times 10^{-5}$ for the Ir^{4+} infrared absorption band in β-Ga_2O_3 . If the refractive index and local field correction factors are ignored, f becomes 2.5×10^{-4}. These results for f are consistent with expected values of oscillator strengths for $d - d$ transitions [132].

5.6 Effects of Above-Band-Gap Photons

Ionizing radiation (i.e., above-band-gap photons) was found to change the concentration of Ir^{4+} ions in the Mg-doped and Fe-doped β-Ga_2O_3 crystals. We used x rays, but near-band-edge light from a lamp or a laser is also expected to produce similar effects. In our experiments, the above-band-gap photons form "free" electrons and holes. At 77 K, the majority of these electrons and holes immediately recombine, but some become trapped at existing deep donors and acceptors. These electrons and holes remain trapped for long periods of time when the crystal is kept at a sufficiently low temperature. Figure 5.6 shows the effects of a 77 K x-ray irradiation on an Mg-doped β-Ga_2O_3 crystal. These spectra were taken at 40 K with the magnetic field along the b direction. In Figure 5.6(a), the spectrum taken before the exposure to x rays shows EPR signals from Fe^{3+} and Ir^{4+} ions, but not from Mg acceptors. The Mg acceptors are not present in Figure 5.6(a) because they are all in their singly ionized nonparamagnetic charge state (Mg_{Ga}^{-}), compensated in large part by the Ir^{4+} ions. This is consistent with the large concentration of Ir^{4+} ions observed in Figure 5.1 and listed in Table 5.2. After the irradiation at 77 K with x rays, the Mg-doped

crystal was cooled to 40 K, with no intervening warming, and the EPR spectrum in Figure 5.6(b) was taken. The characteristic spectrum [12] from the neutral Mg acceptors (Mg^0_{Ga}) is now present and the intensities of the Fe^{3+} and Ir^{4+} signals have both decreased by 41% from their pre-irradiated values. The following is a possible explanation for these observations. During the 77 K irradiation of the Mg-doped crystal, the Fe^{3+} and Ir^{4+} ions trap electrons and become Fe^{2+} and Ir^{3+} ions while, at the same time, the singly ionized Mg acceptors (Mg^-_{Ga}) trap holes and become neutral acceptors (Mg^0_{Ga}).

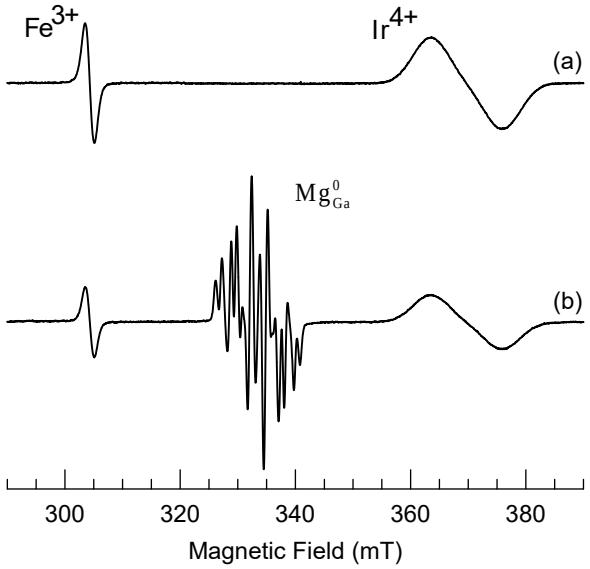

Figure 5.6. EPR spectra from an Mg-doped β-Ga_2O_3 crystal taken at 40 K before and after an irradiation at 77 K with x rays. Identical spectrometer settings were used when acquiring the two spectra. (a) Before the irradiation, only the Fe^{3+} and Ir^{4+} signals are present. (b) After the irradiation, and with no warming step, the Mg^0_{Ga} signal is present and the Fe^{3+} and Ir^{4+} signals have decreased. Reprinted with permission [36].

The effects of x rays are quite different for the Fe-doped β-Ga_2O_3 crystals. EPR spectra were taken at 40 K from an Fe-doped crystal before and after an irradiation at 77 K with x rays. These results are shown in Figure 5.7. Because of the large difference

in the intensities of the Fe^{3+} and Ir^{4+} signals (due to very different linewidths), the before and after Fe^{3+} spectra were taken with one set of spectrometer conditions and the before and after Ir^{4+} spectra were taken with a different set of spectrometer conditions. After the irradiation, the intensity of the Fe^{3+} EPR signal is reduced by a factor of 1.7 (i.e., the signal is 40% less than its pre-irradiated value) whereas the Ir^{4+} EPR signal is a factor of 3.2 larger than its pre-irradiated value. This decrease of the Fe^{3+} signal and increase of the Ir^{4+} signal is consistent with the Fe ions being acceptors [104, 106, 107] and the Ir ions being donors. Specifically, Fe^{3+} ions trap electrons during the irradiation and become Fe^{2+} ions while nonparamagnetic Ir^{3+} ions trap holes and become Ir^{4+} ions. The Fe^{3+} and Ir^{4+} ions slowly revert to their pre-irradiation concentrations when the crystal is returned to room temperature. This recovery was 60% complete after the crystal was held for five min at room temperature.

5.7 Conclusions

Large crystals of β-Ga_2O_3 are often grown by the Czochralski or edge-dened film-fed methods using iridium crucibles, and thus contain significant concentrations of isolated iridium ions. These unintentional deep donors are present as Ir^{3+} ($5d^6$) ions in n-type crystals. When the Fermi level is lower, Ir^{4+} ($5d^5$) ions will also be present. We use EPR and infrared absorption to observe these Ir^{4+} ions in Mg and Fe doped crystals. The Ir^{4+} ions occupy Ga(2) sites with the six oxygen neighbors forming a distorted octahedron. Because of a large spin-orbit interaction, these $5d^5$ ions have a low-spin S = 1/2 ground state. Principal g values of the resulting anisotropic EPR spectrum are 2.662, 1.815, and 0.541. Also, the Ir^{4+} ions have a room-temperature infrared absorption band peaking at 5153 cm^{-1}. This $d-d$ band has a small oscillator strength and is highly polarized. In the Mg-doped crystals, the Ir^{4+} ions are the

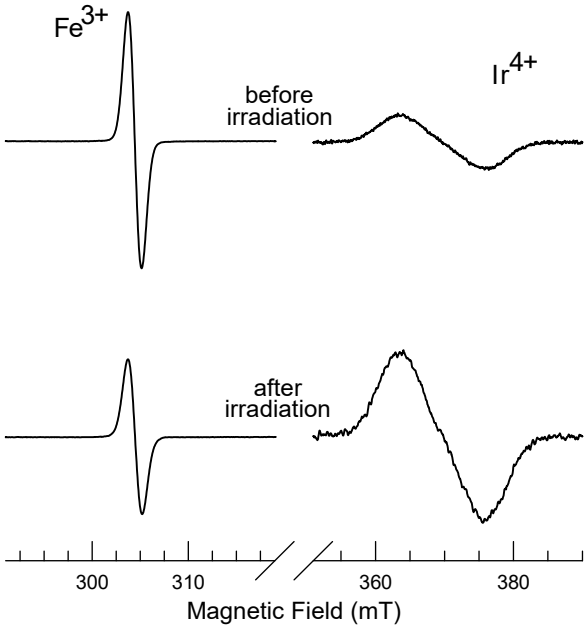

Figure 5.7. EPR spectra from an Fe-doped β-Ga_2O_3 crystal taken at 40 K before and after an irradiation at 77 K with x rays. The upper left (Fe^{3+}) and upper right (Ir^{4+}) spectra were taken before the irradiation. The lower left (Fe^{3+}) and lower right (Ir^{4+}) spectra were taken after the irradiation. One set of spectrometer operating conditions was used for the two Fe^{3+} spectra and a different set was used for the two Ir^{4+} spectra. The two Fe^{3+} spectra can be directly compared and the two Ir^{4+} spectra can be directly compared. Reprinted with permission [36].

primary source of compensation for the Mg acceptors. The presence of the iridium ions is expected to make p-type doping of bulk-grown crystals more difficult. Of special interest are the photon-induced changes in the charge state of the iridium donors. During an exposure at 77 K to ionizing radiation (x rays in our experiments), the concentration of Ir^{4+} ions decreased in Mg-doped crystals and increased in Fe-doped crystals. These results suggest that the Fe impurities behave as acceptors and prefer to be in the Fe^{3+} or Fe^{2+} states and the Ir impurities behave as donors and prefer to be in the Ir^{4+} or Ir^{3+} states.

6. Deep Donors and Acceptors in β-Ga_2O_3 Crystals: Determination of the $Fe^{2+/3+}$ Level by a Non-contact Method

6.1 Abstract

Electron paramagnetic resonance (EPR) and infrared absorption are used to determine the $Fe^{2+/3+}$ level in Fe-doped β-Ga_2O_3 crystals. With these noncontact spectroscopy methods, a value of 0.83 eV below the conduction band is obtained for this level. Our results clearly establish that the E2 deep level observed in DLTS experiments is due to the thermal release of electrons from Fe^{2+} ions. The crystals used in this investigation were grown by the Czochralski method and contained similar concentrations of deep Fe acceptors and deep Ir donors, along with trace amounts of Cr donors. Exposing a crystal at room temperature to 325 or 405 nm laser light converts a significant portion of the Fe^{3+} acceptors to the Fe^{2+} charge state and, at the same time, converts an equivalent number of Ir^{3+} donors to the Ir^{4+} charge state. The Fe^{3+} EPR spectrum slowly recovers after the light is removed, as electrons are thermally released from Fe^{2+} ions to the conduction band. These electrons recombine nonradiatively with holes at Ir^{4+} ions. Using a general-order kinetics model, the analysis of a set of isothermal recovery curves for the Fe^{3+} EPR signal taken between 295 and 315 K gives an activation energy of 0.83 $\pm$ 0.04 eV for the decay of the photoinduced Fe^{2+} ions. A weak thermoluminescence (TL) peak near 350 K is produced when a few of the electrons released from the Fe^{2+} ions recombine radiatively with holes at Cr^{4+} ions. Photoluminescence (PL) results verify that these crystals contain Cr ions.

6.2 Introduction

Single crystals of β-Ga_2O_3, in bulk and thin-film form, are presently being developed for applications extending from power electronics to solar-blind detectors

[102, 109, 133–138]. To support these device efforts, fundamental studies of the more common deep donors and acceptors in this material are needed. It is expected that these deep levels, when present, may influence the performance of the emerging optical and electronic devices. The acceptors and donors receiving the most attention, thus far, are Fe, Mg, Cr, H, and Ir [12, 35, 36, 101, 104, 106, 107, 139–141]. In this chapter, a description of using noncontact spectroscopy methods to characterize the behaviors of Fe acceptors and Ir and Cr donors is presented. Iron impurities appear at trace levels in many bulk β-Ga_2O_3 crystals (as a result of their unintentional presence in the starting materials used to grow the crystals). The Fe ions may also be deliberately added to the starting materials to produce Fe-doped semi-insulating β-Ga_2O_3 crystals suitable for use as substrates for film growth. Although usually at concentrations lower than those of the unintentional Fe ions, Cr ions are also introduced at trace levels into bulk β-Ga_2O_3 crystals because of slightly impure starting materials. In addition to the Fe and Cr ions, large concentrations of Ir ions are present in bulk β-Ga_2O_3 crystals that are grown using iridium crucibles [36, 101]. Electron paramagnetic resonance (EPR), infrared absorption, and thermoluminescence (TL) are used in the present study to determine the $Fe^{2+/3+}$ level in an Fe-doped β-Ga_2O_3 crystal. The use of EPR is an important part of this investigation as this experimental technique provides direct and unambiguous identification of specific charge states of many defects via the hyperfine and fine structure patterns appearing in their ground-state spectra.

6.3 Experimental

Bulk β-Ga_2O_3 crystals doped with Fe were obtained from Kyma Technologies (Raleigh, NC). They were grown by the Czochralski method and had 0.01 mol.% of Fe_2O_3 added to the starting materials. They also contained large concentrations of

Ir ions [36, 101] and trace amounts of Cr ions [35, 141], both substituting for sixfold Ga^{3+} ions and both unintentionally present. The samples used in this study were rectangular b plates, approximately 3×4 mm^2 with a thickness of 0.37 mm.

The EPR spectra of Fe^{3+} ions were obtained near room temperature using a Bruker EMX spectrometer operating at 9.393 GHz. Flowing nitrogen gas was used to control the temperature of the sample. The gas was contained within the glassware of an Oxford Instruments ESR-900 cryostat extending vertically through the center of the microwave resonator. To reach an equilibrium temperature in the 295 to 315 K range, the gas was preheated by passing through a small external furnace before reaching the crystal. Infrared absorption spectra of Ir^{4+} ions were taken with a ThermoScientific Nicolet 8700 FTIR spectrometer. A white-light (QTH) source (with a silicon wafer acting as a filter to remove wavelengths shorter than 1.1 μm), a CaF_2 beam splitter, and a DTGS detector were used, along with an ultra-broad-band (250 nm to 4 μm) fused-silica wire-grid polarizer from Thorlabs (Model WP25M-UB). Surface losses have been removed from the absorption spectra shown in this paper. The Fe^{2+}, Ir^{4+}, and Cr^{4+} charge states are produced near room temperature using a He-Cd laser (325 or 442 nm) or a diode laser (405 nm).

Photoluminescence (PL) spectra were obtained with an Horiba Fluorolog-3 spectrometer and using a long pass filter for wavelengths > 420 nm on the emission port. This spectrometer uses a xenon lamp as the excitation source, a Hamamatsu R928 photomultiplier as a detector, and two double-grating monochromators to measure emisson and excitation spectra. Thermoluminescence (TL) glow curves were taken with a Harshaw TLD-3500 reader. In this instrument, a photomultiplier tube monitors the total light output.

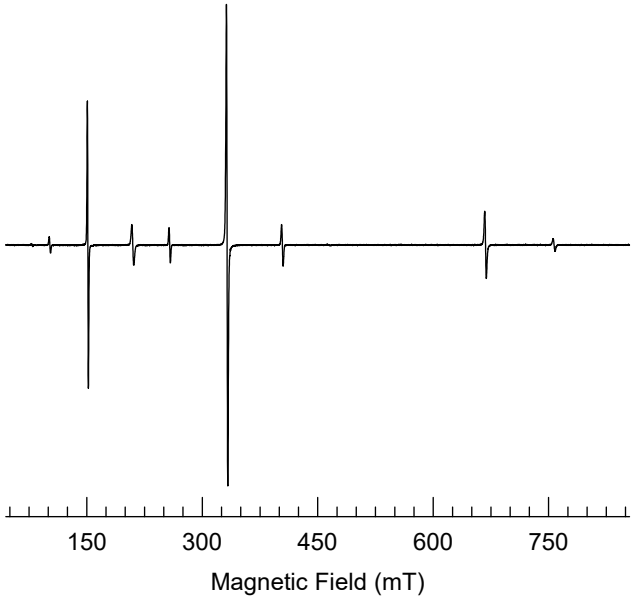

Figure 6.1. EPR spectrum taken at 296 K from an Fe-doped β-Ga_2O_3 crystal. The magnetic field is along the c direction and the microwave frequency is 9.393 GHz. All eight lines are from Fe^{3+} ions occupying sixfold Ga^{3+} sites.

6.4 Production and Thermal Decay of Fe^{2+} and Ir^{4+} Ions

Figure 6.1 shows the EPR spectrum from Fe^{3+} ($3d^5$) ions in an Fe-doped β-Ga_2O_3 crystal. These data were obtained at room temperature ($\sim$296 K). The magnetic field was aligned near the c axis, the microwave frequency was 9.393 GHz, and no laser light was incident on the sample. Before acquiring the spectrum, the effects of previous illuminations were removed by holding the crystal at 250° C for several minutes. There are two dominant lines in Figure 6.1 at 150.0 and 332.3 mT and six less intense lines at 102.0, 209.7, 257.6, 404.0, 667.9, and 756.8 mT. These lines, representing both allowed and forbidden transitions, are assigned to Fe^{3+} ions at sixfold sites [115, 142]. The Fe^{3+} ions have the high-spin S = 5/2 ground state, with large zero-field splittings caused by the low-symmetry monoclinic crystal structure. As seen in Figure 6.1, zero-field splittings often result in complex nonsymmetrical patterns in the EPR spectra from transition-metal ions [31, 33]. During the present study, no evidence was found that Fe^{3+} ions occupy fourfold sites in Fe-doped β-Ga_2O_3 crystals grown by the Czochralski method [115]. Also, it is noted that no EPR spectrum has been reported thus far for Fe^{2+} ($3d^6$) ions in β-Ga_2O_3 crystals.

The Fe^{3+} EPR spectrum decreases in intensity when the Fe-doped β-Ga_2O_3 crystal is exposed at room temperature to below-band-gap laser light. Both 325 and 405 nm photons easily produce this effect, with reductions of approximately 30% typically observed. Although they are less efficient, 442 nm photons also reduce the Fe^{3+} concentration, whereas 532 nm photons have very little effect. A similar wavelength dependence has been reported for photocurrents in Fe-doped β-Ga_2O_3 crystals [143]. Figure 6.2 shows the rapid decrease in the intensity of the Fe^{3+} spectrum when 405 nm laser light is applied and the subsequent slow recovery of the Fe^{3+} spectrum when the laser light is removed. These data were acquired at 297 K with the magnetic field set at the upper peak of the line at 150.0 mT in Figure 6.1. The EPR spectrometer

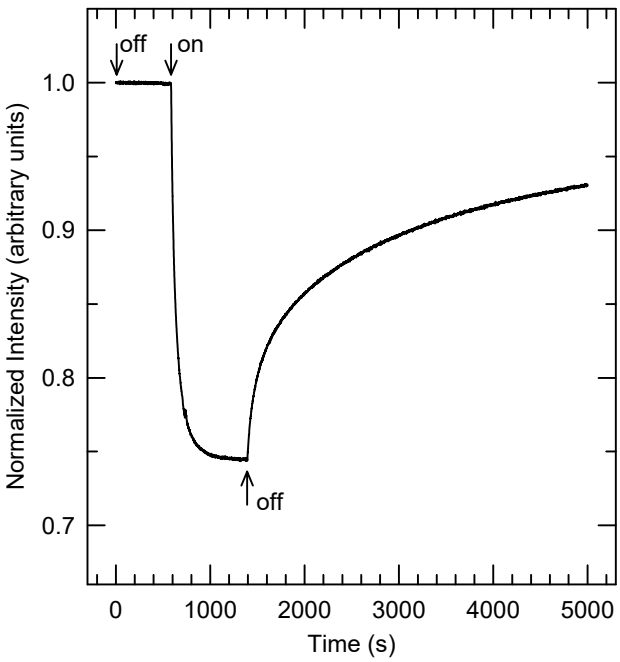

Figure 6.2. Monitoring the intensity of the Fe^{3+} EPR line at 150.0 mT in Figure 6.1 before, during, and after exposure to 325 nm laser light. The temperature is 297 K. The Fe^{3+} signal decreases when the light forms Fe^{2+} ions. When the light is removed, the Fe^{3+} signal slowly recovers as the Fe^{2+} ions thermally convert back to Fe^{3+} ions by releasing an electron.

was operated in a kinetics mode (i.e., a time sweep) with a fixed magnetic field, thus allowing the production and/or decay of a specific EPR line (representing one charge state of a defect) to be monitored.

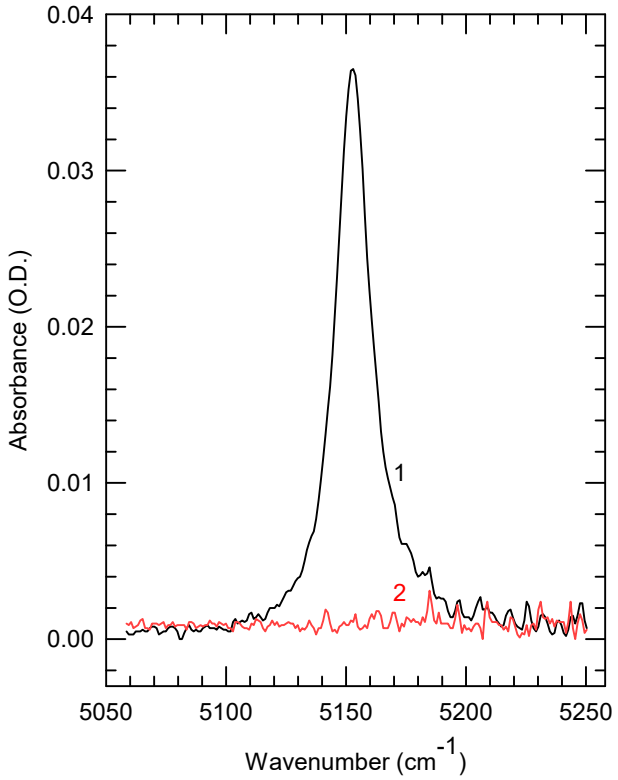

Figure 6.3. Infrared absorption from Ir^{4+} ions in an Fe-doped β-Ga_2O_3 crystal. These spectra were obtained at room temperature. The spectrometer's light propagated along the b direction of the crystal with the electric field vector E along the a direction. Sample thickness (i.e., optical path length) is 0.37 mm. The lower (red curve) was taken before exposure to 405 nm laser light and the upper (blue curve) was taken during exposure to the 405 nm laser light.

Exposure of an Fe-doped β-Ga_2O_3 crystal at room temperature to below-band-gap laser light also affects the charge states of the iridium donors. Figure 6.3 shows the infrared optical absorption spectra taken at 296 K before and during an illumination with 405 nm laser light. The band peaking at 5153 cm^{-1} (1.94 μm), with a half-width near 17 cm^{-1}, has been assigned to Ir^{4+} ($5d^5$) ions at sixfold Ga^{3+} sites [36,101]. This band represents a $d-d$ transition within the set of t_{2g} orbitals. The lower red curve

(labeled '2') in Figure 6.3 shows that Ir^{4+} ions are not present before the illumination. At this stage, all of the iridium is present as neutral Ir^{3+} donors. A large number of Ir^{4+} ions, however, are produced by the laser light (upper blue curve labeled '1' in Figure 6.3). These Ir^{4+} ions begin to thermally decay immediately after the light is removed. The empirical relationship between concentration and peak absorption coefficient, $N = (2.4 \times 10^{18}\ \text{cm}^2)\alpha$, from References [36, 42] is used to determine the maximum concentration of Ir^{4+} ions formed by the laser light in the Fe-doped crystal. A value of $\alpha = 2.19\ \text{cm}^{-1}$ from Figure 6.3 gives a concentration $N = 5.3 \times 10^{18}\ \text{cm}^{-3}$ for the Ir^{4+} ions.

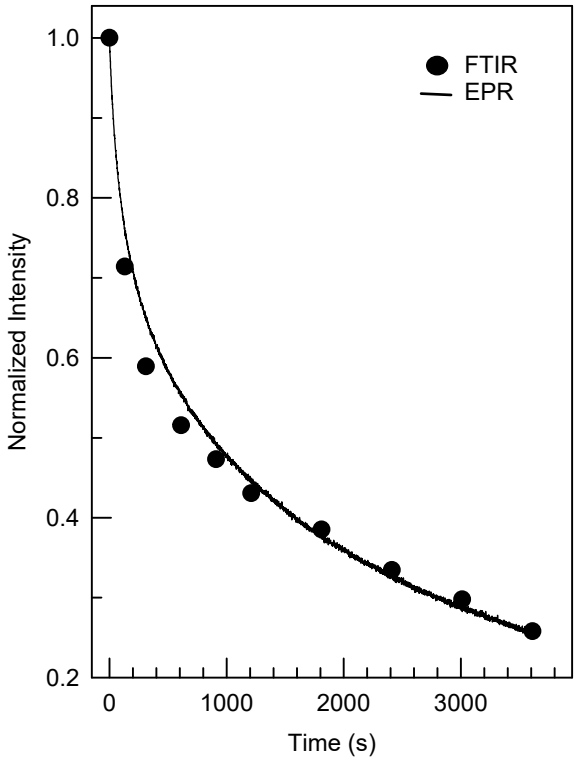

Figure 6.4. The decay of the Ir^{4+} ions and the recovery of the Fe^{3+} ions at 297 K after the laser light is removed. To allow a direct comparison, the inverse of the Fe^{3+} recovery is plotted (i.e., the decay of photoinduced Fe^{2+}).

The photoinduced results in Figures 6.2 and 6.3 demonstrate that the iridium

ions lose electrons and the iron ions gain electrons during an illumination at room temperature. Specifically, laser light converts neutral Ir^{3+} donors to singly ionized Ir^{4+} donors and, at the same time, converts neutral Fe^{3+} acceptors to singly ionized Fe^{2+} acceptors. This behavior suggests that the $Ir^{4+/3+}$ level is below the $Fe^{3+/2+}$ level in β-Ga_2O_3. Figure 6.4 shows the decay of the Ir^{4+} ions and the recovery of the Fe^{3+} ions at 297 K after the laser light is removed. To allow a direct comparison, the inverse of the Fe^{3+} recovery is plotted in Figure 6.4. The decay of the Ir^{4+} absorption band (the discrete points) occurred after an illumination with 405 nm laser light, while the recovery of the Fe^{3+} EPR spectrum (the solid curve) followed an illumination with 325 nm laser light. The similarity of the two curves in Figure 6.4 shows that the decay of the Ir^{4+} ions and the recovery of the Fe^{3+} ions are correlated. Although the two sets of data in Figure 6.4 were acquired in quite different experiments (optical absorption versus EPR), the agreement is good.

Two possible mechanisms by which laser light produces the Ir^{4+} and Fe^{2+} ions in the Fe-doped β-Ga_2O_3 crystals are (1) excitation of electrons from the valence band to the Fe^{3+} ions with the holes left in the valence band being trapped on Ir^{3+} ions or (2) excitation of electrons from Ir^{3+} ions to the conduction band with the subsequent trapping of the electrons by Fe^{3+} ions. It is likely that both optical absorption processes may be contributing to the observed photoinduced effects. Independent of the method of production, the decay mechanism that restores the crystal to its pre-illuminated state is the thermally activated release of electrons from the Fe^{2+} ions. The thermoluminescence results, reported in Section 6.6, also provides evidence that the recovery of the Fe^{3+} ions occurs when electrons are thermally released from the Fe^{2+} ions.

Isothermal recovery curves for the Fe^{3+} EPR signal in an Fe-doped β-Ga_2O_3 crystal were obtained at 300.5, 305.0, 310.0, and 315.0 K, after illumination with 325

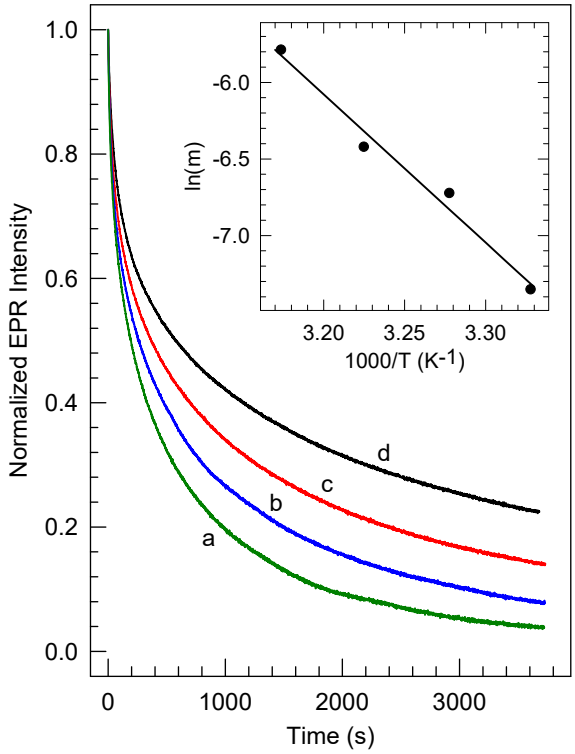

Figure 6.5. Isothermal recovery curves for the Fe^{3+} EPR signal in an Fe-dopedβ-Ga_2O_3 crystal were obtained at d) 300.5, c) 305.0, b) 310.0, and a) 315.0 K, after illumination with 325 nm laser light. Recovery of the Fe^{3+} ions corresponds to the decay of the photoinduced Fe^{2+} ions, thus the data are plotted as decay curves. The inset shows the plot of $\ln m$ versus 1/T used to obtain the activation energy E_a.

nm laser light. The recovery of the Fe^{3+} ions corresponds to the decay of the photoinduced Fe^{2+} ions, thus the data are plotted as decay curves in Figure 6.5. These data were obtained by monitoring the intensity of the Fe^{3+} EPR line at 150.0 mT when the magnetic field is along the c direction (see Figure 6.1). Prior to recording a recovery curve, the crystal was exposed to 325 nm laser light until a reduced equilibrium concentration was established for the Fe^{3+} ions (approximately 4-5 min). Then the intensity of the EPR line was monitored as a function of time after removing the laser light. This is the procedure illustrated in Figure 6.2. While acquiring a recovery curve, the temperature varied by less than 0.1 K. The kinetics model and process used to extract an activation energy from the set of decay curves in Figure 6.5 is described in Section 6.5.

The approximate initial concentrations of Fe^{3+} were 1.6×10^{19} $cm^{-3} \pm 1.5\%$ at 300.5, 305, 310, and 315 K, respectively. Monitoring the EPR Fe^{3+} signal at 150.0 mT for these temperatures shows a decreasing intensity proportional to $1/T$. These initial concentrations of Fe^{3+} centers represent a population in thermal equilibrium. The relative concentration values corresponding to the four temperatures are determined to within approximately 1.5% because they are directly compared to the defects EPR spectrum taken with the same spectrometer settings and only slightly different temperatures. The absolute value of the spin concentration at 300.5 K was determined by comparing the change of the EPR spectrum from the Fe^{3+} defect with FTIR absorption data for the Ir^{4+}. The total concentration of the Ir^{4+} is estimated from Smakula's formula and proportional to the photoinduced change in the Fe^{3+}. This process is an estimate and considered precise to within a factor of two.

6.5 Analysis of Thermal Decay Curves

A general-order kinetics model [40,48,50,51,54] is used to analyze the thermal decay results since the individual decay curves in Figure 6.5 are not single exponentials. First-order kinetics does not allow for the retrapping of released charge and thus is characterized by simple exponential decay curves [44,45]. The other extreme, referred to as second-order kinetics, occurs when retrapping dominates the decay process and gives decay curves with long "tails" [46].

First-order kinetics do not provide a good fit to the individual decay curves in Figure 6.5 (i.e., these curves are not single exponentials). Thus, a general-order kinetics model [40,48,144] is used that takes into account the retrapping of thermally released charge on the octahedral Fe^{3+} sites to determine an activation energy for the thermal decay of these photoinduced singly ionized Fe acceptors. This analysis starts with the following differential equation:

$$\frac{\mathrm{d}n}{\mathrm{d}t} = n^b s' e^{-\frac{E_a}{k_B T}} \tag{6.1}$$

Here, n is the concentration of photoinducted acceptors, t is the time, b is the parameter which describes the order of the kinetics, E_a is the activation energy, and T is the temperature. In this general order equation, the prefactor s does not have units of inverse seconds, and instead has units of $\mathrm{m}^{3(b-1)}\mathrm{s}^{-1}$. Integrating equation 6.1 has the time-dependent decay solution for $b > 1$,

$$n(t) = n_0 \left[1 + s' n_0^{b-1}(b-1) e^{-\frac{E_a}{k_B T}} t\right]^{\frac{1}{1-b}} \tag{6.2}$$

where n_0 represents the initial concentration of singly ionized Fe acceptors (when the

laser light is removed). Equation 6.2 is then rewritten in the following linear form:

$$\left(\frac{n}{n_0}\right)^{1-b} = \left[1 + s' n_0^{b-1}(b-1)e^{-\frac{E_a}{k_B T}}t\right] \tag{6.3}$$

Using the experimental data in Figure 6.5, the quantity $(n/n_0)^{1-b}$ was plotted versus time for each decay curve. For each of these plots, the value of b was adjusted until a straight line emerged. The four values of b obtained from this procedure were very similar and their average was $b = 1.85$. This value of b indicates that the kinetics is closer to the second order and consistent with strong retrapping of thermally released charge on Fe^{3+} sites. Each of the four straight lines has a different slope. From equation 6.3, these slopes are m_0

$$m_i^{'} = s' n_{0,i}^{b-1}(b-1)e^{-\frac{E_a}{k_B T}} \tag{6.4}$$

where the index $i = 1$ to 4 corresponds to the four different temperatures where decay curves were obtained. While it is possible to adjust for different starting concentrations, each decay curve has approximately the same value of n_0 for the same intensity and duration of exposure of excitation light. Thus, it can be written n_0, $i = c_i N_0$ where the values of c_i are 1.00 for all temperatures and, N_0 represents the initial concentration for the 300.5 K decay curve. Equation 6.4 then becomes

$$\mathrm{m_i} = \frac{m_i^{'}}{c_i^{b-1}} = s' N_{0,i}^{b-1}(b-1)e^{-\frac{E_a}{k_B T_i}} \tag{6.5}$$

By taking the natural logarithm of each side, equation can be rewritten in the following form

$$\ln(\mathrm{m_i}) = \ln\left[s' N_{0,i}^{b-1}(b-1)\right] - \frac{E_a}{k_B T_i} \tag{6.6}$$

The final step is to construct a plot of $\ln(\mathrm{m_i})$ versus 1/Ti (this plot contains four

points, one for each decay curve, and is shown in the inset of Figure 6.5). The slope of the best-fit straight line in the inset is E/k. Based on the thermal decay data in Figure 6.5, the general-order kinetics analysis gives an activation energy of $E_a = 0.83 \pm 0.04$ eV.

Now it is prudent to discuss the physical meaning of this activation energy. The effect of the 325, 405, or 442 nm light removes electrons from donor Ir^{3+} making Ir^{4+} and traps electrons on Fe^{3+} acceptors producing (Fe^{2+}) through either or both production pathways described earlier. Upon removal of the light, these electrons and holes recombine and the restoration rate of the original distribution of charge depends on the temperature. There are two possible recombination processes 1) it may be initiated by the thermal release of holes from Ir^{4+} or 2) the thermal release of electrons from Fe^{3+}. Experimentally, it is often difficult to determine whether the measured activation energy is associated with the hole release or the electron release. DLTS, Van der Pauw, and Hall measurements have suggested that the E2 trap with an activation energy 0.78 to 0.86 eV is from the release of electrons based on voltage bias and the signs of coefficients [104, 106, 107, 145, 146]. In the following section, it is suggested that the activation energy of 0.83 eV describes the thermal release of an electron from Fe^{2+} and not mobile holes releasing from Ir^{4+}, which is consistent with previous experimental measurements.

6.6 Luminescence Results

An uncorrected PL spectrum from Ga_2O_3 using 265 nm excitation light is shown in Figure 6.6. The two sharp lines at 691 and 697 nm are the characteristic R-lines from Cr^{3+} ($3d^3$) in β-Ga_2O_3 resulting from the $^4T_2 \rightarrow ^4A_2$ and $^4E_2 \rightarrow ^4A_2$ transitions where the $^4T_2$ dominates at room temperature [141]. Photoluminescence was performed using 5 nm increments of excitation light from 250 to 650 nm with no other PL

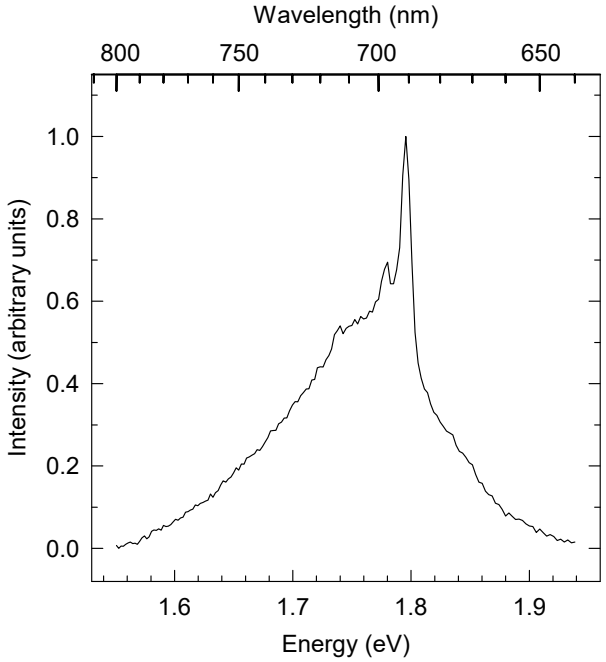

Figure 6.6. Photoluminescence spectrum taken at room temperature from an Fe-doped β-Ga_2O_3 crystal. The excitation wavelength was 265 nm. The emission is from the $^4T_2 \rightarrow {}^4A_2$ and $^4E_2 \rightarrow {}^4A_2$ transitions of Cr^{3+} ions. The spectrum is uncorrected.

spectrum being found from 270 to 800 nm. Additionally, multiple samples of Fe-doped Ga_2O_3 , including scrap from the boule, were analyzed and found to have varying concentrations of Cr^{3+} based on PL measurements. Many samples had little to no Cr^{3+} indicating that incorporation of Cr into the crystal is not uniform. Based on the PL measurements, Cr^{3+} is the only luminescent center in Fe-doped Ga_2O_3 despite the much larger concentrations of Fe^{3+} and Ir^{3+} present in these crystals.

Figure 6.7 shows the TL spectrum of Fe-doped Ga_2O_3 after exposure to either 325 or 405 nm light. The sample was heated from 28° to 200° C with a heating rate of 1°C/s. A single weak TL peak was observed with a peak temperature of 76° C. Attempts to measure the spectral dependence of the TL peak through the use of ANDOR and the InsTec heating stage were not successful due to the low intensity of the peak and the loss of collection sensitivity between the PMT on the Harshaw system and CCD on the ANDOR. The simulated TL glow curve is constructed from

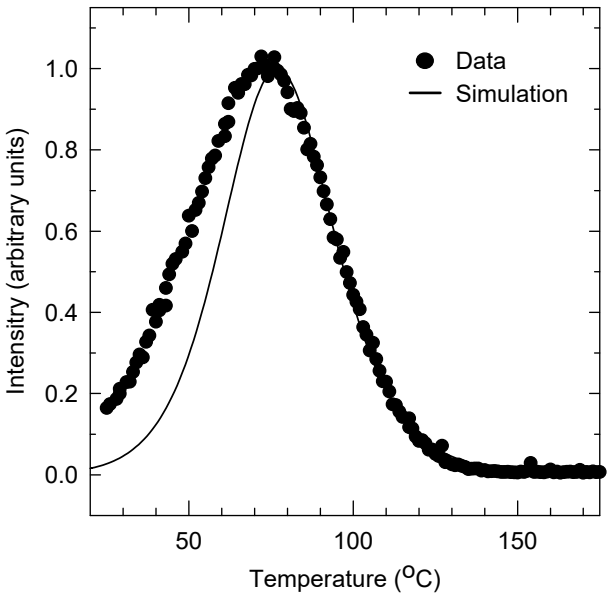

Figure 6.7. Thermoluminescence spectra of Fe-doped β-Ga_2O_3 using a 1° C/s heating rate. The simulated TL glow curve is constructed from the parameters of the isothermal decay of Fe^{2+} measured by EPR shown in Figure 6.5 using general order decay with $b = 1.85$, $\beta = 1$, and $s = 1.95 \times 10^{11}$.

the parameters of the isothermal decay of Fe^{2+} measured by EPR using general order decay with $b = 1.85$, $\beta = 1$, and $s = 1.95 \times 10^{11}$. There is good agreement between the measured and simulated TL suggesting that the release of photoinduced trapped charge is responsible for observed TL peak. Furthermore, since Cr^{3+} is the only identified luminescent center, it is suggested that Cr^{3+} is the responsible for the weak observed TL peak.

As stated earlier, there are two possible recombination processes to describe the activation energy that resets all the observed defects in the crystal: the release of electrons from Fe^{2+} or the release of holes from Ir^{4+}.[1] The latter will be considered first. If holes are mobile and released from Ir^{4+}, they travel predominantly to Fe^{2+} sites with only a small portion returning to Cr sites and recombining. After illumination, EPR confirms a small decrease in Cr^{3+} concentration indicating it has changed charge state. To recover the Cr^{3+} concentration, Cr must be in the 2+ charge state and accept the mobile holes leaving from Ir^{4+} to form Cr^{3+}. Using mobiles as the recombination process, the resultant recombination on Cr sites does not create an electron in an excited state 3+ state to have the $^4T_2 \rightarrow {}^4A_2$ and $^4E_2 \rightarrow {}^4A_2$ transitions. This recombination process disagrees with the experimental data. If electrons are mobile and released from Fe^{2+}, they will travel predominantly to holes trapped on Ir^{4+} and a small fraction will travel to Cr sites and recombine. Under this model, Cr must be in the 4+ charge state, and recombination leaves Cr^{3+} and mobile electrons in an excited state. This process is consistent with observations [104, 106, 107] and this experimental data.

[1]Other explanations outside of these two possibilities for luminescence involve invoking unseen EPR defects before or after irradiation and are unlikely.

6.7 Summary

Large single crystals of intentionally Fe doped Ga_2O_3 grown in iridium crucibles contain significant concentrations of isolated Fe^{3+} ($3d^5$) and the unintentional deep donor Ir^{3+} ($5d^6$) impurity ions. Both Fe^{3+} and Ir^{4+} occupy the Ga(2) sites with six oxygen ligands forming a distorted octahedral. These substrates are semi-insulating indicating a low-Fermi level and compensation of the Si shallow donor. EPR, infrared absorption, photoluminescence, and thermoluminescence are used to observe the roles and change of charge states of Fe, Cr, and Ir. Exposure to 325 or 405 nm light simultaneously removes electrons from Cr and Ir donors forming Cr^{4+} and Ir^{4+} and traps the electrons on Fe acceptors creating Fe^{2+}. Removal of light allows the electrons to be released from Fe^{2+}, recombining non-radiatively on Ir^{4+} sites. FTIR measurements monitor the formation and decay of Ir^{4+} and confirming it as the predominant deep donor. Subsequent heating of the crystal produces a weak TL peak at 76° C when a small number of electrons from the Fe^{2+} combine on Cr^{4+}. Thermal decay of the $Fe^{2+/3+}$ is monitored by EPR at four different temperatures, and using a general order kinetics model, the activation energy for this transition is calculated to be 0.83 ± 0.04 eV.

7. Summary and Conclusions

7.1 $LiGaO_2$ Summary

Intrinsic cation point defects have been identified and characterized for the first time in $LiGaO_2$ through the use of radiation and EPR measurements. In some samples, large concentrations of lithium vacancies are present in as-grown substrates that serve as stable hole traps after ionizing radiation. These holes trapped on oxygen ligands are paramagnetic, stable for days, and have an activation energy of approximately 1.05 eV below the conduction band minimum. The paramagnetic spectrum resulting from lithium vacancies is characteristic of nearly equal interaction with two gallium neighboring ions. Thermal decay of lithium vacancies produces luminescence with several broad peaks when heated above 150° C. Gallium vacancies have also been found and partially characterized after electron irradiation, and have been found in as-grown substrates. This defect is also paramagnetic with holes localizing on a single oxygen ligand causing significant lattice relaxation resulting in a paramagnetic defect that is stable for years. EPR spectra for gallium vacancies in $LiGaO_2$ are from the interaction with a single gallium neighboring ion. The activation energy of this defect is estimated to be at least 2.5 eV below the conduction band minimum. Both defects in $LiGaO_2$ are examples of acceptor-bound small polarons, and the spin density on the surrounding ions confirms the validity of the ionic model from CFT for developing an understanding of the fundamental nature of these cation vacancies.

7.2 β-Ga_2O_3 Summary

Two important extrinsic point defects have been identified and characterized in β-Ga_2O_3 for the first time. Single crystals of Ga_2O_3 grown in iridium crucibles have been shown to incorporate significant concentrations of Ir^{3+} ($5d^6$) ions onto the octahedral

Ga(2) sites. This impurity acts as an unintentional deep donor, remaining as Ir^{3+} in n-type material, and as Ir^{4+} ($5d^5$) in lower Fermi crystals. Ir^{4+} has been observed in both Mg and Fe doped Ga_2O_3 crystals through FTIR measurements. Large spin-orbit interactions cause Ir^{4+} to have a low-spin S = 1/2 ground state configuration. This impurity has a large degree of covalency highlighting some of the shortfalls of CFT in accurately describing a defect model. Unpaired spin in the t_{2g} orbitals is IR active, resulting in a $d-d$ transition within the t_{2g} levels that is highly polarized and peaking at 5153 cm^{-1} at room temperature. The unintentional presence of iridium in bulk single crystals makes accurate assessment of suitable shallow acceptors more difficult.

The thermal activation of the $Fe^{2+/3+}$ level in β-Ga_2O_3 has also been determined using a novel non-contact method. Fe^{3+} ($3d^5$) is incorporated into Ga_2O_3 on the octahedral Ga(2) sites acting as a deep acceptor. Using general order kinetics, the acceptor level is found to have an energy of 0.83 $\pm$ 0.04 eV below the conduction band minimum. Iron is incorporated into crystals either through deliberate doping with Fe_2O_3 powders or as a impurity from the starting material of gallium powders. Iron lowers the Fermi level of as-grown crystals making the material semi-insulating by compensating the Si shallow donors. In Fe-doped Ga_2O_3 , electrons can be excited off of Ir^{3+} making them Ir^{4+} and trapped at Fe^{3+} sites forming Fe^{2+} using sub-band-gap light with wavelengths shorter than 442 nm. Combining FTIR measurements with the observed changes in EPR signal intensity allows estimation of the total concentrations of Ir^{4+} formed and Fe^{3+} incorporated into the crystal through the growth process within a factor of two.

7.3 Additional Intrinsic Point Defects: Finding Oxygen Vacancies

In both $LiGaO_2$ and β-Ga_2O_3, oxygen vacancies remain undiscovered and uncharacterized. Lithium gallate remains a relatively unexplored material despite its widespread use as a substrate. No calculations are available to suggest their depth or role in the material. However, given the similarity to Ga_2O_3, analogies of oxygen vacancies between the two materials should be considered. For Ga_2O_3, current indications within the solid state community have concluded that oxygen vacancies are deep donors and unsuitable for device applications. However, the role exhibited by, and existing concentrations in as-grown crystals of these vacancies is yet to unambiguously be determined.

Neutron irradiation of both crystals provides a possible path forward for uncovering oxygen vacancies and their role. To date, neutron irradiation at the Ohio State University reactor has been performed on only two Ga_2O_3 crystals. Both of these crystals were as-grown UID single crystals and originally n-type. While gallium vacancy EPR signals were present in both, only one is suitable for detailed study. This indicates that neutron flux, and therefore dose, in addition to finding a suitable sample is important for accurate and detailed studies. It is possible that the Fermi level is not yet low enough in neutron irradiated crystals to detect oxygen vacancies. For β-Ga_2O_3, samples doped with Fe or Mg already having low Fermi levels should be considered candidates for neutron irradiation. This may assist in uncovering and characterizing deeper levels not seen in the as-grown doped crystals. For $LiGaO_2$, no neutron irradiation experiments have been performed. If neutron irradiation creates oxygen vacancies in these crystals, it may provide important information and clues on how to create and monitor oxygen vacancies in Ga_2O_3.

7.4 Extrinsic Point Defect Studies: Doping and Diffusion

Significant challenges remain in finding suitable extrinsic shallow acceptors for β-Ga_2O_3. At present only three extrinsic defects have been intentional doped and reported in the literature for Ga_2O_3: Fe, Mg, Cr. Two of these defects are known to be acceptors: Mg and Fe. The role of Cr is unclear. Also, the role of copper and lithium in β-Ga_2O_3 remain unexplored. Although expected to be a deep acceptor from its position on the periodic table, Cu with a ground state configuration of $[Ar]3d^{10}4s^1$ has the potential to enter the crystal in either the 2+, 3+, or 4+ charge state. With this variety of charge states, Cu may act as either an acceptor or a donor, or both. It is also possible, that Cu may form more weakly coupled S = 1 which opens up the possibility of reducing the activation energy. Lithium, with a ground state configuration of $[He]2s^1$, is expected to be an acceptor entering the crystal in the 1+ charge state. Lithium also carries the possibility of forming weakly coupled S = 1 defects which may be shallow. Diffusion experiments in air and with flowing nitrogen should be perform on suitable n-type bulk Ga_2O_3 crystals.

Lithium gallate is largely unexplored for extrinsic defect studies and remains a potential alternative to β-Ga_2O_3. Unintentionally present silicon in Ga_2O_3 has been identified as the shallow donor and should explored through doping or diffusion studies for $LiGaO_2$. Similarly, Mg doping or diffusion should also be explored. Suitable shallow donors and acceptors may prove easier to identify in this ternary compound and have broad functionality given the two different cation sites. Additionally, $LiGaO_2$ has not been shown to form self-trapped holes, a serious drawback in device application for β-Ga_2O_3.

7.5 Applications Beyond $LiGaO_2$ and Ga_2O_3

The materials explored in this work have broad functionality and interest for the power electronics and optoelectronics communities. Significant research remains for these two materials to characterize the fundamental intrinsic and the role of other extrinsic point defects for specific applications. Developments in understanding the role of point defects in these materials has built a foundation to explore other next-generation materials for lasers capable of operating at wavelength longer than 6 μm including $LiGaS_2$, $LiGaSe_2$, $BaGa_4S_7$, $BaGa_4Se_7$, and the quaternary chalcogenides $BaGa_2GeS_6$, and $BaGa_2GeSe_6$ and to improve bulk crystal growth for the United States. These next generation materials are of immediate and future interest to the Air Force, Department of Defense, Department of Energy, and United States commercial industry.

Appendix A. Spin Hamiltonian for Systems with S > 1/2

The generic spin Hamiltonian for any spin system can be written as,

$$H = \beta \mathbf{S} \cdot \mathbf{g} \cdot \mathbf{B} + \mathbf{S} \cdot \mathbf{D} \cdot \mathbf{S} + \mathbf{I} \cdot \mathbf{A} \cdot \mathbf{S} + \mathbf{I} \cdot \mathbf{Q} \cdot \mathbf{I} - g_n \beta_n \mathbf{I} \cdot \mathbf{B} \tag{A.1}$$

where β is the Bohr magneton, **S** is the spin operator, **g** is the g matrix, **B** is the magnetic field, **I** is the nuclear spin operator, **A** is the hyperfine matrix, **D** is the fine structure matrix, **Q** is the nuclear electric quadrapole matrix, g_n is the nuclear g factor, and β_n is the nuclear magneton. [31, 33]. However, for Cr^{3+} in Ga_2O_3 not all of these terms are needed based on the observed spectrum, shown in Figure A.1 [35]. The observed spectrum contains only two lines which result from the fine structure

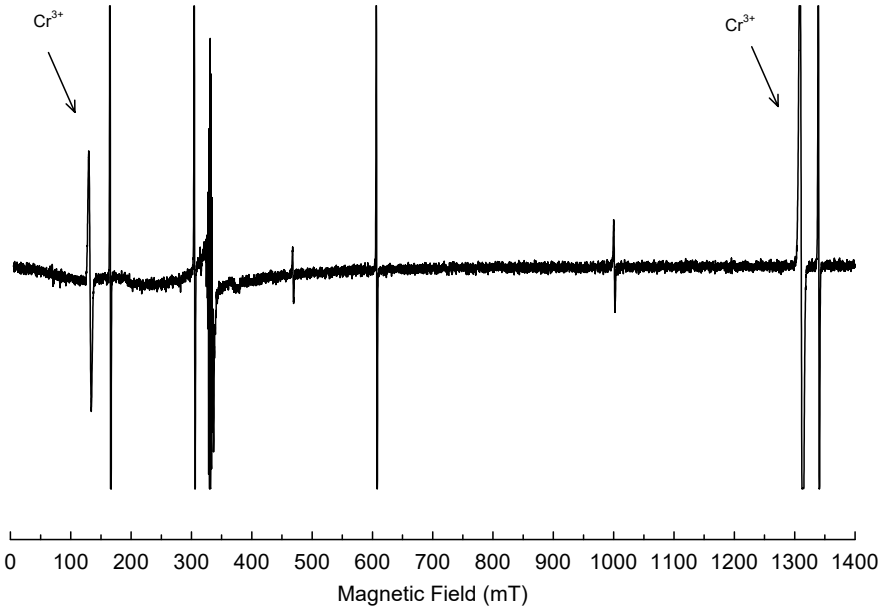

Figure A.1. Observed Cr^{3+} EPR spectrum in neutron irradiated β-Ga_2O_3 at 40 K with a microwave frequency $\nu = 9.40$ GHz, from 9 scans across the magnetic field values. The magnetic field B applied is along the crystallographic b-axis.

splitting and their associated transitions. Since, hyperfine lines are not observed for this paramagnetic defect, only electron Zeeman and fine structure terms need consideration. This simplifies the above expression to,

$$H = H_Z + H_{ZFS} \tag{A.2}$$

with H_z the electron Zeeman term and H_{ZFS} the zero-field splitting term. The zero-field splitting terms are determined by the crystallographic structure of the material, in this case monoclinic, and incorporated through the use of Stephen's operators [147, 148]. Since Ga_2O_3 is a low symmetry crystal, with a single crystallographic symmetry axis, the b axis, the zero-field splitting term will contain both higher and lower symmetry Stephen's operators [34, 147–153]. The zero-field splitting term is broken in an orthorhombic and a monoclinic portion,

$$H_{ZFS} = H_{ZFS}^{ortho} + H_{ZFS}^{mono} \tag{A.3}$$

which, for Cr^{3+} with $S = \frac{3}{2}$ in Ga_2O_3 , have Stephen's operators of second rank

$$H_{ZFS}^{ortho} = B_2^0 O_2^0 + B_2^2 O_2^2 \tag{A.4}$$

$$H_{ZFS}^{mono} = B_2^1 O_2^1 \tag{A.5}$$

where the Stephen's operators are defined as,

$$O_2^0 = 3S_z - S(S+1) \tag{A.6}$$

$$O_2^1 = \frac{1}{4}\left[S_z\left(S_+ + S_-\right) + \left(S_+ + S_-\right)S_z\right] \tag{A.7}$$

$$O_2^2 = \frac{1}{2}\left[S_+^2 + S_-^2\right] \tag{A.8}$$

The expression for the monoclinic terms included in the zero field splitting, arise from the selection of the symmetry axis for a given crystal with its relation to the magnetic field. In this example, the y-axis has been chosen as the axis of symmetry, and negates the use of negative Stephen's operators and coefficients.

Simplifying equation A.3, an isotropic **g** is assumed, transforming the electron Zeeman term into,

$$H_Z = \mathbf{g} \cdot \beta \left[S_x B_x + S_y B_y + S_z B_z \right] \tag{A.9}$$

with

$$B_x = B \sin\theta \cos\phi \tag{A.10}$$

$$B_y = B \sin\theta \sin\phi \tag{A.11}$$

$$B_z = B \cos\theta \tag{A.12}$$

$$S_x = \frac{1}{2} \left(S_+ + S_- \right) \tag{A.13}$$

$$S_y = \frac{1}{2i} \left(S_+ - S_- \right) \tag{A.14}$$

and S_z is the spin of the system, defined as $\frac{3}{2}$. Substituting in the the various terms, equation A.5 becomes,

$$\begin{aligned} H_Z = \mathbf{g}\beta B \Bigg[& S_z \cos\theta + \frac{1}{2} \left(\sin\theta \cos\phi - i \sin\theta \sin\phi \right) S_+ \\ & + \frac{1}{2} \left(\sin\theta \cos\phi + i \sin\theta \sin\phi \right) S_- \Bigg] \end{aligned} \tag{A.15}$$

As a first approximation, the constant term $S(S+1)$ is dropped from O_2^0 and **g** is reduced to a scalar quantity when combining the electron Zeeman and zero field

splitting terms,. The resulting form of the spin Hamiltonian becomes,

$$\begin{aligned} H = & g\beta B S_z \cos\theta + \frac{1}{2} g\beta B \sin\theta \left(\cos\phi - i\sin\phi\right) S_+ \\ & + \frac{1}{2} g\beta B \sin\theta \left(cos\phi - i\sin\phi\right) S_- + 3B_2^0 O_2^0 \\ & + \frac{1}{4} B_2^1 \left(S_z S_+ + S_z S_- + S_+ S_z + S_z S_-\right) + \frac{1}{2} B_2^2 \left(S_+^2 + S_-^2\right) \end{aligned} \tag{A.16}$$

Now, the spin Hamiltonian can be setup as a matrix with each element describing the energy of a given transition for m_s. Since the spin of the Cr^{3+} defect is $S = \frac{3}{2}$, the basis set uses $\mid m_s\rangle$ with $m_s = {}^{+}\frac{3}{2}, {}^{+}\frac{1}{2}, {}^{-}\frac{1}{2}, {}^{-}\frac{3}{2}$

	$+\frac{3}{2}$	$+\frac{1}{2}$	$-\frac{1}{2}$	$-\frac{3}{2}$
$+\frac{3}{2}$	$a_{1,1}$			
$+\frac{1}{2}$	$a_{2,1}$	$a_{2,2}$		
$-\frac{1}{2}$	$a_{3,1}$	$a_{3,2}$	$a_{3,3}$	
$-\frac{3}{2}$	0	$a_{4,2}$	$a_{4,3}$	$a_{4,4}$

To solve for each of the individual elements, the raising and lowering operators are calculated using,

$$S_+ \mid m_s\rangle = \left[S(S+1) - m(m+1)\right]^{\frac{1}{2}} \mid m+1\rangle \tag{A.17}$$

$$S_- \mid m_s\rangle = \left[S(S+1) - m(m-1)\right]^{\frac{1}{2}} \mid m-1\rangle \tag{A.18}$$

which then yield the following values for S_+ and S_- for the various transitions,

$$\begin{aligned} S_+ \mid^{+}\tfrac{1}{2}\rangle &= \sqrt{3} \mid^{+}\tfrac{3}{2}\rangle & \qquad S_- \mid^{+}\tfrac{3}{2}\rangle &= \sqrt{3} \mid^{+}\tfrac{1}{2}\rangle \\ S_+ \mid^{-}\tfrac{1}{2}\rangle &= 2 \mid^{+}\tfrac{1}{2}\rangle & \qquad S_- \mid^{+}\tfrac{1}{2}\rangle &= 2 \mid^{-}\tfrac{1}{2}\rangle \\ S_+ \mid^{-}\tfrac{3}{2}\rangle &= \sqrt{3} \mid^{-}\tfrac{1}{2}\rangle & \qquad S_- \mid^{-}\tfrac{1}{2}\rangle &= \sqrt{3} \mid^{-}\tfrac{3}{2}\rangle \end{aligned}$$

With these values, the individual elements can calculated,

$$a_{1,1} = \frac{3}{2} g\beta B \cos\theta + \frac{27}{4} B_2^0 \tag{A.19}$$

$$a_{2,2} = \frac{1}{2} g\beta B \cos\theta + \frac{3}{4} B_2^0 \tag{A.20}$$

$$a_{3,3} = -\frac{1}{2} g\beta \cos\theta + \frac{3}{4} B_2^0 \tag{A.21}$$

$$a_{4,4} = -\frac{3}{2} g\beta \cos\theta + \frac{27}{4} B_2^0 \tag{A.22}$$

$$a_{2,1} = \sqrt{3} g\beta B A_1 \sin\theta + \frac{\sqrt{3}}{2} B_2^1 \tag{A.23}$$

$$a_{3,1} = \sqrt{3} B_2^2 \tag{A.24}$$

$$a_{3,2} = 2 g\beta B A_1 \sin\theta \tag{A.25}$$

$$a_{4,2} = \sqrt{3} B_2^2 \tag{A.26}$$

$$a_{4,3} = \sqrt{3} g\beta B A_1 \sin\theta - \frac{\sqrt{3}}{2} B_2^1 \tag{A.27}$$

$$a_{1,2} = a_{2,1}^* \tag{A.28}$$

$$a_{1,3} = a_{3,1}^* \tag{A.29}$$

$$a_{2,3} = a_{3,2}^* \tag{A.30}$$

$$a_{2,4} = a_{4,2}^* \tag{A.31}$$

$$a_{3,4} = a_{4,3}^* \tag{A.32}$$

where in above equations,

$$A_1 = \frac{1}{2} \left(\cos\theta + i \sin\phi \right) \tag{A.33}$$

With an expression for the energy of each transition and a set of real values along the diagonal, it is now possible to solve the system of equations for their respective eigenvalues at a given magnetic field for specified angles of θ and ϕ. Computing the energy at discrete magnetic values will produce a set of values for each transition, and for a given microwave frequency, a prediction can be made of where a transition (i.e.

absorption of microwave energy) is likely to be observed in an EPR spectrum, shown in Figure A.2. The calculated Cr^{3+} ion transitions with $\nu = 9.4$ GHz, assuming

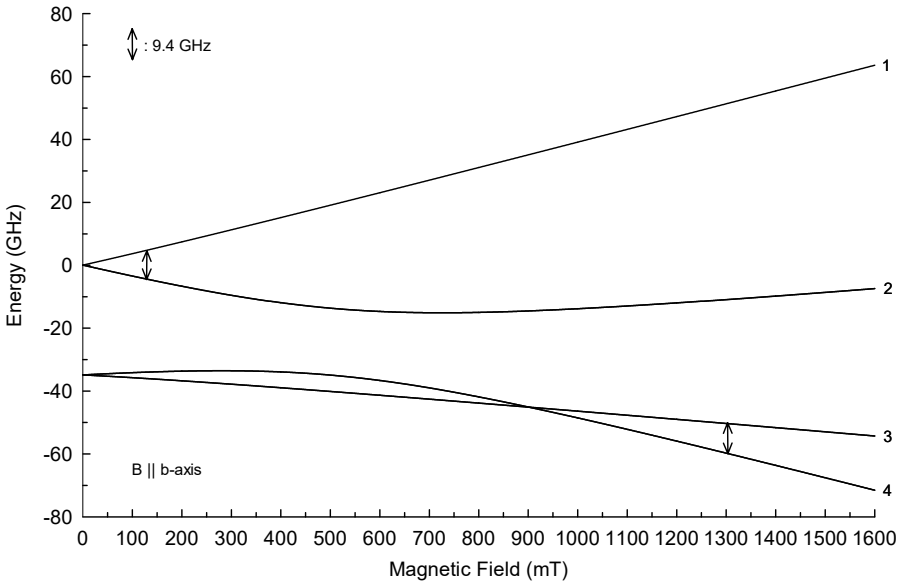

Figure A.2. Energy level of Cr^{3+} ion in β-Ga_2O_3 with magnetic field B aligned with crystallographic b axis with a microwave frequency $\nu = 9.40$ GHz. For this calculation, an isotropic g is assumed with a value of 1.97 [35]. The length of the arrows between the number transitions correspond to the microwave frequency.

an isotropic g, are represented by the arrows. These transitions coincide with the observed EPR tranistions of the Cr^{3+} lines shown in Figure A.1. Understanding key points of development of the spin Hamiltonian, generation of the energy level plots, and angular dependence modeling (a.k.a crystal roadmap) for Cr^{3+} , enables application of this algorithm to any spin system. At present, a similar development for the Cr^{2+} , Cr^{4+} , Fe^{2+} , Fe^{3+} , and Fe^{4+} spin systems are underway. A spin Hamiltonian for the Mn^{2+} (3d5) has already been developed and will be used as a guide for pursuing Fe^{3+} along with Meil'man's work [115, 142, 154]. Development of spin Hamiltonian analysis will aid in identification of the unknown signals seen in

β-Ga_2O_3 at low temperatures.

Bibliography

1. N. W. Ashcroft and N. D. Mermin, *Solid State Phyiscs*. W. B. Saunders Co., 1976.

2. A. Alkauskas, M. D. McCluskey, and C. G. Van de Walle, "Tutorial: Defects in semiconductors-combining experiment and theory," *Journal of Applied Physics*, vol. 119, no. 181101, 2016.

3. S. Geller, "Crystal structure of β-Ga_2O_3 ," *Journal of Chemical Physics*, vol. 33, p. 676, 1960.

4. J. Ahman, S. G., and J. Albertsson, "A reinvestigation of β gallium oxide," *Acta Crystallographica*, vol. C52, p. 1336, 1996.

5. B. E. Kananen, L. E. Halliburton, K. T. Stevens, G. K. Foundos, and N. C. Giles, "Gallium vacancies in β-Ga_2O_3 crystals," *Applied Physics Letters*, vol. 110, no. 202104, 2017.

6. E. G. Villora, K. Shimamaru, Y. Yoshikawa, T. Ujiie, and K. Aoki, "Electrical conductivity and carrier concentration control in β-Ga_2O_3 by Si doping," *Applied Physics Letters*, vol. 92, no. 202118, 2008.

7. N. T. Son, K. Goto, K. Nomura, Q. T. Thieu, R. Togashi, H. Murakami, Y. Kumagai, A. Kuramata, M. Higashiwaki, A. Koukitu, S. Yamakoshi, B. Monemar, and E. Janzen, "Electronic properties of the residual donor in unintentionally doped β-Ga_2O_3 ," *Journal of Applied Physics*, vol. 120, no. 235703, 2016.

8. A. T. Neal, M. Shin, R. Lopez, J. V. Li, D. B. Thomson, D. C. Chabak, and G. H. Jessen, "Incomplete ionization of a 110 meV unintentional donor in β-Ga_2O_3 and its effect on power devices," *Nature - Scientific Reports*, vol. 7, p. 13218, 2017.

9. M. Higashiwaki, K. Saski, H. Murakami, Y. Kumagai, A. Koukitu, A. Kuramata, T. Masui, and S. Yamakoshi, "Recent progress in Ga_2O_3 power devices," *Semiconductor Science and Technology*, vol. 31, no. 034001, 2016.

10. S. I. Stepanov, V. I. Nikolaev, V. E. Bougrov, and A. E. Romanov, "Gallium oxide: properties and applications - a review," *Reviews on Advanced Materials Science*, vol. 44, pp. 63–86, 2015.

11. J. B. Varley, J. R. Weber, A. Janotti, and C. G. Van de Walle, "Oxygen vacancies and donor impurities in β-Ga_2O_3 ," *Applied Physics Letters*, vol. 97, no. 142106, 2010.

12. B. E. Kananen, L. E. Halliburton, E. M. Scherrer, K. T. Stevens, G. K. Foundos, K. B. Chang, and N. C. Giles, "Electron paramagnetic resonance study of neutral Mg acceptors in β-Ga_2O_3 crystals," *Applied Physics Letters*, vol. 111, no. 072102, 2017.

13. B. E. Kananen, N. C. Giles, L. E. Halliburton, G. K. Foundos, K. B. Chang, and K. T. Stevens, "Self trapped holes in in β-Ga_2O_3 crystals," *Journal of Applied Physics*, vol. 122, no. 215703, 2017.

14. M. S. Holston, I. P. Gerguson, N. C. Giles, W. D. J. McClory, J. W., J. Jianfeng, F. A. Selim, and L. E. Halliburton, "Green luminescence from Cu-diffused $LiGaO_2$ crystals," *Journal of Luminescence*, vol. 170, p. 17, 2016.

15. T. Omata, H. Nagatani, I. Suzuki, and M. Kita, "Wurtzite-derived ternary I-III-O_2 semiconductors," *Science and Technology of Advanced Materials*, vol. 16, no. 024902, 2015.

16. T. Omata, K. Tanaka, A. Tazuke, K. Nose, and S. Otsuka-Yao-Matsuo, "Wide band gap semiconductor alloy: $x(LiGaO_2)_{\frac{1}{2}} - (1-x)ZnO$," *Journal of Applied Physics*, vol. 103, no. 083706, 2008.

17. T. Omata, M. Kita, K. Nose, T. K., and S. Otsuka-Yao-Matsuo, "Zn_2LiGaO_2 wurtzite-derived wide band gap oxide," *Japanese Journal of Applied Physics*, vol. 50, no. 031102, 2011.

18. N. C. Giles, C. Xu, M. J. Callahan, B. Wang, J. S. Neal, and L. A. Boatner, "Effect of phonon coupling and free carriers on band-edge emission at room temperature in *n*-type ZnO crystals," *Applied Physics Letters*, vol. 89, no. 251906, 2006.

19. C. Chen, C. A. Li, S. H. Yu, and M. M. C. Chou, "Growth and characterization of β- $LiGaO_2$ single crystal," *Journal of Crystal Growth*, vol. 402, p. 325, 2014.

20. T. Huang, S. Zhou, H. Teng, H. Lin, J. Wang, P. Han, and R. Zhang, "Growth and characterization of ZnO films on (001), (100), amnd (010) $LiGaO_2$ substrates," *Journal of Crystal Growth*, vol. 310, p. 3144, 2008.

21. M. M. C. Chou, C. Chen, C. Chang, and C. A. Li, "Growth and characterization of a-plane GaN films on (010) $LiGaO_2$ substrate by chemical deposition," *Journal of Crystal Growth*, vol. 363, p. 113, 2013.

22. J. E. Huheey, *Inorganic Chemistry: Principles and structure of reactivity*, 3rd ed. Harper and Row, 1983.

23. H. Bethe, "Termaufspaltung in Kristallen," *Annalen der Physik*, vol. 3, p. 251, 1929.

24. J. H. Van Vleck, "Theory of the Variations in Paramagnetic Anisotropy Among Different Salts of the Iron Group," *Physical Review*, vol. 41, p. 208, 1932.

25. ——, "Valence Strength and the Magnetism of Complex Salts," *Journal of Chemical Physics*, vol. 3, p. 807, 1935.

26. L. Pauling, *The Nature of the Chemical Bond*, 3rd ed. Cornell University Press, 1960.

27. P. A. Cox, *Transition metal oxides: An introduction to their electronic structure and properties*, 1st ed. Clarendon Press, 1995.

28. I. B. Bersuker, *Electronic structure and properties of transition metal compounds: Introduction to the theory*, 1st ed. John Wiley and Sons, Inc., 1996.

29. A. Abragam and B. Bleaney, *Electron Paramagnetic Resonance of Transition Metal Ions*, 1st ed. Clarendon Press, 1970.

30. J. Owen and J. H. M. Thornley, "Covalent bonding and magnetic properties of transition metal ions," *Reports on Progress in Physics*, vol. 29, p. 675, 1966.

31. A. Abragam and B. Bleaney, *Electron Paramagnetic Resonance of Transition Metal Ions*, 1st ed. Clarendon Press, 1970.

32. S. Gasiorowicz, *Quantum Physics*, 3rd ed. John Wiley and Sons, 2003.

33. J. A. Weil and J. R. Bolton, *Electron Paramagnetic Resonance: Elementary Theory and Practical Applications*, 2nd ed. John Wiley and Sons, Inc, 2007.

34. C. Rudowicz and P. Gnutek, "Modeling techniques for analysis and interpretation of electron magnetic resonance (EMR) data for transition ions at low symmetry sites in crystals - a primer for experimentalists," *Physica B*, vol. 404, pp. 3582–3593, 2009.

35. T. Yeom, I. G. Kim, S. Lee, S. H. Choh, and Y. M. Yu, "Electron paramagnetic resonance characterization of Cr^{3+} impurities in a β-Ga_2O_3 single crystal," *Journal of Applied Physics*, vol. 93, no. 6, pp. 3315–3319, 2003.

36. C. A. Lenyk, M. S. Holston, B. E. Kananen, L. E. Halliburton, and N. C. Giles, "Ir^{4+} ions in β-Ga_2O_3 crystals: an unintentional deep donor," *Journal of Applied Physics*, vol. 125, no. 045703, 2019.

37. L. E. Halliburton, Private Communication.

38. C. A. Lenyk, M. S. Holston, B. E. Kananen, L. E. Halliburton, and N. C. Giles, "Lithium and gallium vacancies in $LiGaO_2$ crystals," *Journal of Applied Physics*, vol. 124, no. 135702, 2018.

39. M. Fox, *Optical Properties of Solids*, 2nd ed. Oxford University Press, 2010.

40. S. W. S. McKeever, *Thermoluminescence of solids*. Cambridge University Press, 1988.

41. B. Henderson and G. F. Imbusch, *Optical Spectroscopy of Inorganic Solids*. Oxford University Press, 1989.

42. ——, *Optical Spectroscopy of Inorganic Solids*. Oxford University Press, 1989.

43. D. L. Dexter, "Absorption of light by atoms in solids," *Physical Review*, vol. 101, p. 48, 1956.

44. J. T. Randall and M. H. F. Wilkins, "Phosphorescence and electron traps I. The study of trap distributions," *Proceedings of the Royal Society A: Mathematical, Physical and Engineering Sciences*, vol. 184, pp. 366–389, 1945.

45. ——, "Phosphorescence and electron traps II. THe interpretation of long-period phosphorescence," *Proceedings of the Royal Society A: Mathematical, Physical and Engineering Sciences*, vol. 184, pp. 390–407, 1945.

46. G. F. J. Garlick and A. F. Gibson, "The electron trap mechanism of luminscence in sulphide and silicate phosphors," *Proceedings of the Physical Society*, vol. 60, pp. 574–590, 1948.

47. R. Chen, N. Kristianpoller, Z. Davidson, and R. Visocekas, "Mixed first and second order kinetics in thermally stimulated processes," *Journal of Luminescence*, vol. 23, pp. 293–303, 1981.

48. C. E. May and P. J. A., "Thermoluminescence kinetics of alpha-irradiated alkali halides," *Journal of Chemical Physics*, vol. 40, pp. 1401–1409, 1964.

49. R. Chen, "Glow curves with general order kinetics," *Journal of the Electrochemical Society: Solid State Science*, pp. 1254–1257, September 1969.

50. N. Takeuchi, K. Inabe, and H. Nanto, "Letter: Note on the isothermal decay method for determining trap depth from glow curves," *Journal of Materials Science*, vol. 10, p. 159, 1975.

51. R. Chen and W. S. McKeever, Stephen, *Theory of Thermoluminescence and Related Phenomena*. World Scientific Publishing, 1997.

52. M. S. Holston, "Characterization of Point Defects in Lithium Aluminate ($LiAlO_2$) Single Crystals," Ph.D. dissertation, Air Force Institute of Technology, 2015.

53. A. J. J. Bos, "Theory of Thermoluminescence," *Radiation Measurements*, vol. 41, p. S45, 2006.

54. M. S. Rasheedy, "On the general-order kinetics of the thermoluminescence glow peak," *Journal of Physics: Condensed Matter*, vol. 5, pp. 633–636, 1993.

55. N. A. Bogdanov, V. M. Katukuri, J. Romhnyi, V. Yushankhai, V. Kataev, B. Bchner, J. van den Brink, and L. Hozoi, "Orbital reconstruction in nonpolar tetravalent transition-metal oxide layers," *Nature Communications*, vol. 6, no. 7306, 2015.

56. K. S. Pederson, "Iridates from the molecular side," *Nature Communications*, vol. 7, no. 12195, 2016.

57. G. Cao and P. Schlottmann, "The challenge of spinorbit-tuned ground states in iridates: a key issues review," *Reports on Progress in Physics*, vol. 7, no. 042502, 2018.

58. S. Fuchs, T. Dey, G. Aslan-Cansever, A. Maljuk, S. Wurmehl, B. Bchner, and V. Kataev, "Unraveling the nature of magnetism of the $5d^4$ double perovskite Ba_2YIrO_6," *Physical Review Letters*, vol. 120, no. 237204, 2018.

59. J. H. E. Griffiths and J. Owen, "Complex hyperfine structures in microwave spectra of covalent iridium compounds," *Proceedings of the Royal Society of London Series A - Mathematical and Physical Sciences*, vol. 226, p. 96, 1954.

60. J. H. E. Griffiths, J. Owen, and P. J. G., "Exchanges interactions in antiferromagnetic salts of iridium 1. Paramagnetic resonance experiments," *Proceedings of the Royal Society of London Series A - Mathematical and Physical Sciences*, vol. 250, p. 84, 1959.

61. A. Abragam and B. Bleaney, *Electron Paramagnetic Resonance of Transition Metal Ions*, 1st ed. Clarendon Press, 1970.

62. J. H. M. Thornley, "Magnetic properties of $mathrm[IrX_6]^{2-}$ complexes," *Journal of Physics Part C Solid State Physics*, vol. 1, p. 1024, 1968.

63. C. P. J. Poole, *Electron Spin Resonance: A Comprehensive Treatise on Experimental Techniques*, 2nd ed. John Wiley and Sons, 1983.

64. "EMX Series User's Manual, Bruker BioSpin Corp," 2009.

65. S. Yang, "Paramagnetic Resonance Studies of Defects in Titanium Dioxide Crystals," Ph.D. dissertation, West Virginia University, 2010.

66. N. B. Colthup, L. H. Daly, and S. E. Wiberley, *Introduction to Infrared and Raman Spectroscopy*, 3rd ed. Academic Press, 1990.

67. G. F. Knoll, *Radiation Detection and Measurement*, 4th ed. John Wiley & Sons, Inc., 2010.

68. "Model 3500 Manual TLD Reader with WinREMS Operator's manual, Thermo Scientific," 2010.

69. "Model 3500 Manual TLD Reader Technical Service manual, Thermo Electron Corporation," 2002.

70. "Users manual for HCP621V/HCP622V/HCS621V/HCS622V, InsTech Inc." 2007.

71. "Shamrock 193i User Guide, ANDOR an Oxford Instruments Company," 2015.

72. "iDus Hardware Guide (Covering iDus models 401 and 420), ANDOR an Oxford Instruments Company," 2015.

73. I. Suzuki and T. Omata, "Multinary wurtzite-type oxide semiconductors: present status and perspectives," *Semiconductor Science and Technology*, vol. 32, p. 013007, 2017.

74. S. Tumnas, P. Mackonis, R. Nedzinskas, L. Trinkler, B. Berzina, V. Korsaks, L. Chang, and M. M. C. Chou, "Optical properties of lithium gallium oxide," *Applied Surface Science*, vol. 421, p. 837, 2017.

75. N. W. Johnson, J. A. McLeod, and A. Moewes, "The electronic structure of lithium metagallate," *Journal of Physics: Condensed Matter*, vol. 23, no. 445501, 2011.

76. A. Boonchun and W. R. L. Lambrecht, "First-principles study of the elasticity, piezoelectricity, and vibrational modes in $LiGaO_2$ compared with ZnO and GaN," *Physical Review B*, vol. 81, no. 079904, 2010.

77. S. N. Rashkeev, S. Limpijumnong, and W. R. L. Lambrecht, "Theoretical evaluation of $LiGaO_2$ for frequency upconversion to ultraviolet," *Journal of Optical Society of America B*, vol. 16, p. 2217, 1999.

78. T. Omata, M. M. Kita, K. Tachibana, and S. S. Otsuka-Yao-Matsuo, "Structural variation and optical properties of ZnO- $LiGaO_2$ pseudo-binary system," *Journal of Solid State Chemistry*, vol. 188, p. 92, 2012.

79. Q. F. Li and J. Kuo, "First-principles study of band gap engineering of ZnO by alloying with $LiGaO_2$ for ultraviolet applications," *Journal of Applied Physics*, vol. 114, no. 063715, 2013.

80. A. Boonchun and W. R. L. Lambrecht, "Electronic structure, doping and lattice dynamics of $LiGaO_2$," *Proceedings of SPIE*, vol. 7940, no. 79400N, 2011.

81. T. Yanagida, Y. Fujimoto, M. Koshimizu, N. Kawano, G. Okada, and N. N. Kawaguchi, "Comparative Studies of Optical and Scintillation Properties between $LiGaO_2$ and $LiAlO_2$ Crystals," *Journal of the Physical Society of Japan*, vol. 86, no. 094201, 2017.

82. L. Trinkler, A. Trukhin, B. Berzina, V. Korsaks, P. ajev, R. Nedzinskas, S. Tumnas, M. M. C. Chou, L. Chang, and C.-A. Li, "Luminescence properties of $LiGaO_2$ crystal," *Optical Materials*, vol. 69, p. 449, 2017.

83. S. Kck and S. Hartung, "Comparative study of the spectroscopic properties of Cr^{4+} -doped $LiAlO_2$ and $LiGaO_2$," *Chemical Physics*, vol. 240, p. 387, 1999.

84. G. J. Dirksen, A. N. J. M. Hoffman, T. P. Vandebout, M. P. G. Laudy, and G. Blasse, "Luminescence spectra of pure and doped $mathrmGaBO_3$ and $LiGaO_2$," *Journal of Materials Chemistry*, vol. 1, p. 1001, 1991.

85. M. S. Holston, J. W. McClory, N. C. Giles, and L. E. Halliburton, "Radiation-induced defects in $LiAlO_2$ crystals: Holes trapped by lithium vacancies and their role in thermoluminescence," *Journal of Luminescence*, vol. 160, p. 43, 2015.

86. M. S. Holston, I. P. Ferguson, J. W. McClory, N. C. Giles, and L. E. Halliburton, "Oxygen vacancies in $LiAlO_2$ crystals," *Physical Review B*, vol. 92, no. 144108, 2015.

87. A. M. Stoneham, J. Gavartin, A. L. Shluger, A. V. Kimmel, D. M. Ramo, H. M. Rnnow, G. Aeppli, and C. Renner, "Trapping, self-trapping and the polaron family," *Journal of Physics: Condensed Matter*, vol. 19, no. 255208, 2007.

88. O. F. Schirmer, "O^- bound small polarons in oxide materials," *Journal of Physics: Condensed Matter*, vol. 18, p. R667, 2006.

89. M. M. Islam, J. Uhlendorf, E. Witt, H. Schmidt, P. Heitjans, and T. Bredow, "Lithium Diusion Mechanisms in β-$LiMO_2$ (M = Al, Ga): A Combined Experimental and Theoretical Study," *Journal of Physical Chemistry C*, vol. 121, no. 27788, 2017.

90. C. V. Chandran, K. Volgmann, S. Nakhal, R. Uecker, E. Witt, M. Lerch, and P. Heitjans, "Local Ion Dynamics in Polycrystalline β-$LiGaO_2$: A Solid-State NMR Study," *International Journal of Research in Physical Chemistry and Chemical Physics*, vol. 231, p. 1443, 2017.

91. N. J. Stone, "Table of nuclear magnetic dipole and electric quadrupole moments," *Atomic Data and Nuclear Data Tables*, vol. 90, p. 75, 2005.

92. M. Marezio, "Crystal Structure of $LiGaO_2$," *Acta Crystallographica*, vol. 18, p. 481, 1965.

93. J. R. Morton and K. F. Preston, "Atomic parameters for paramagnetic resonance data," *Journal of Magnetic Resonance*, vol. 30, p. 577, 1978.

94. J. A. J. Fitzpatrick, F. R. Manby, and C. M. Western, "The interpretation of molecular magnetic hyperfine interactions," *Journal of Chemical Physics*, vol. 122, no. 084312, 2005.

95. R. H. Bartram, C. E. Swenberg, and J. T. Fournier, "R. H. Bartram, C. E. Swenberg, and J. T. Fournier," *Physical Review*, vol. 139, p. A941, 1965.

96. A. G. Milne, *Deep Impurities in Semiconductors*. John Wiley and Sons, 1973.

97. E. G. Villora, K. Hatanaka, H. Odaka, T. Sugawara, T. Miura, H. Fukumura, and T. Fukuda, "Luminescence of undoped β-Ga_2O_3 single crystals excited by picosecond x-ray and sub-picosecond UV pulses," *Solid State Communications*, vol. 127, pp. 385–388, 2003.

98. K. Shimamura, E. G. Villora, T. Ujiie, and K. Aoki, "Excitation and photoluminescence of pure and Si-doped β-Ga_2O_3 single crystals," *Applied Physics Letters*, vol. 92, no. 201194, 2008.

99. M. Yamaga, T. Kishita, E. G. Villora, and K. Shimamura, "Relationship between persistent phosphorescence and electric conductivity in transparent conducting oxide β-Ga_2O_3 ," *Optical Materials Express*, vol. 6, pp. 3135–3144, 2016.

100. S. Yamaoka, Y. Furukawa, and M. Nakayama, "Initial process of photoluminescence dynamics of self-trapped excitons in a β-Ga_2O_3 single crystal," *Physical Review B*, vol. 95, no. 195205, 2017.

101. J. R. Ritter, J. Huso, P. T. Dickens, J. B. Varley, K. G. Lynn, and M. D. McCluskey, "Compensation and hydrogen passivation of magnesium acceptors in β-Ga_2O_3 ," *Applied Physics Letters*, vol. 113, no. 052101, 2018.

102. S. J. Pearton, J. Yang, P. H. Cary, F. Ren, J. Kim, M. J. Tadjer, and M. A. Mastro, "A review of Ga_2O_3 materials, processing, and devices," *Applied Physics Review*, vol. 5, no. 011301, 2018.

103. M. H. Wong, A. Lin, C.-H. Kuramata, S. Yamakoshi, H. Murakami, Y. Kumagai, and M. Higashiwaki, "Acceptor doping of β-Ga_2O_3 by Mg and N implantations," *Applied Physics Letters*, vol. 113, no. 102103, 2018.

104. A. T. Neal, S. Mou, S. Rafique, H. Zhao, E. Ahmadi, J. S. Speck, K. T. Stevens, J. D. Blevins, D. B. Thomson, N. Moser, K. D. Chabak, and G. H. Jessen, "Donors and deep acceptors in β-Ga_2O_3 ," *Applied Physics Letters*, vol. 113, no. 062101, 2018.

105. J. L. Lyons, "A survey of acceptor dopants in β-Ga_2O_3 ," *Semiconductor Science and Technology*, vol. 33, no. 05LT02, 2018.

106. A. Y. Polyakov, N. B. Smirnov, I. V. Shchemerov, S. J. Pearton, F. Ren, A. V. Chernykh, and A. I. Kochkov, "Electrical properties of bulk semi-insulating β-Ga_2O_3 (Fe)," *Applied Physics Letters*, vol. 113, no. 142102, 2018.

107. M. E. Ingebrigtsen, J. B. Varley, A. Y. Kuznetsov, B. G. Svensson, G. Alfieri, A. Mihaila, U. Badstubner, and L. Vines, "Iron and intrinsic deep level states in Ga_2O_3 ," *Applied Physics Letters*, vol. 112, no. 042104, 2018.

108. Q. D. Ho, T. Frauenheim, and P. Deak, "Theoretical confirmation of the polaron model for the Mg acceptor in β-Ga_2O_3 ," *Journal of Applied Physics*, vol. 124, no. 145702, 2018.

109. M. Baldini, Z. Galazka, and G. Wagner, "Recent progress in the growth of β-Ga_2O_3 for power electronics applications," *Materials Science in Semiconductor Processing*, vol. 78, p. 132, 2018.

110. A. Kuramata, K. Koshi, S. Wanatabe, Y. Yamaoka, T. Masui, and S. Yamakoshi, "High quality β-Ga_2O_3 single crystals grown by edge-defined film-fed growth," *Japanese Journal of Applied Physics*, vol. 55, no. 1202A2, 2016.

111. L. Pidol, O. Guillot-Noel, M. Jourdier, A. Kahn-Harari, B. Ferrand, P. Dorenbos, and D. Gourier, "Scintillation quenching by Ir^{3+} impurity in cerium doped lutetium pyrosilicate crystals," *Journal of Physics D: Condensed Matter*, vol. 15, p. 7815, 2003.

112. R. D. Shannon, "Revised effective ionic radii and systemic studies of interatomic distances in halides and chalcogenides," *Acta Crystallographica*, vol. 32, p. 751, 1976.

113. J. H. E. Griffiths and O. J., "Paramagnetic resonance in palladium and platinum group compounds," *Proceedings of the Royal Society A.*, vol. 219, p. 526, 1953.

114. B. Bleaney and M. C. M. O'Brien, "Paramagnetic resonance in some complex cynanides of the iron group II. Theory," *Proceedings of the Royal Society B.*, vol. 69, p. 1216, 1956.

115. M. L. Meilman, "EPR of Fe^{3+} ions in β-Ga_2O_3 crystal," *Soviet Physics - Solid State*, vol. 11, no. 6, pp. 1403–1404, 1969.

116. A. Raizman, J. T. Suss, and W. Low, "Quadrapole interaction and static Jahn-Teller effect in the EPR spectra of Ir^{2+} in MgO and CaO," *Phyiscal Review B*, vol. 15, p. 5184, 1977.

117. J. M. Gaite and H. Rager, "Electron paramagnetic resonance study of iridium in forsterite," *Physics and Chemistry of Minerals*, vol. 30, p. 628, 2003.

118. A. T. Brant, L. E. Halliburton, S. Basun, A. A. Grabar, S. G. Odoulov, A. Shumelyuk, N. C. Giles, and D. R. Evans, "Photoinduced EPR study of Sb^{2+} ions in photorefractive $Sn_2P_2S_6$ crystals," *Physical Review B*, vol. 86, no. 134109, 2012.

119. K. W. Blazey and F. Levy, "EPR of rhodium, osmium, and iridium-doped rutile," *Solid State Communications*, vol. 59, p. 335, 1986.

120. X. F. Hu, S. Y. Wu, G. L. Li, Y. Q. Xu, C. C. Ding, and Z. H. Zhang, "Studies of the local lattice distortions for the various Rh^{3+} centres in AgX (X = Cl and Br)," *Polyhedron*, vol. 117, p. 14, 2016.

121. L. L. Li, S. Y. Wu, P. Xu, and S. X. Zhang, "Studies on the spin Hamiltonian parameters and local structure for Rh^{4+} and Ir^{4+} in TiO_2," *Physics and Chemistry of Minerals*, vol. 37, p. 497, 2010.

122. B. Andlauer, J. Schneider, and W. Tolksdorf, "Optical absorption, fluorescence, and electron spin resonance of Ir^{4+} on octahedral sites in $Y_3Ga_5O_{12}$," *Physica Status Solidi B*, vol. 78, p. 533, 1976.

123. J. P. Clancy, N. Chen, C. Y. Kim, W. F. Chen, K. W. Plumb, B. C. Jeon, T. W. Noh, and Y.-J. Kim, "Spin-orbit coupling in iridium-based 5*d* compounds probed by x-ray absorption spectrscopy," *Physical Review B*, vol. 86, no. 195131, 2012.

124. A. Raizman and J. T. Suss, "Electron paramagnetic resonance of Ir^{4+} ions in MgO and CaO," *Physical Review B*, vol. 22, p. 1141, 1980.

125. O. F. Schirmer, A. Forster, H. Hesse, M. Wohlecke, and S. Kapphan, "Paramagnetic resonance and near-infrared optical absorption of $SrTiO_3$:Ir^{4+}," *Journal of Physics C: Solid State Physics*, vol. 17, p. 1321, 1984.

126. E. Possenriede, O. F. Schirmer, H. J. Donnerberg, and B. Hellerman, "ESR investigation of transition metal defects in $KNbO_3$," *Journal of Physics: Condensed Matter*, vol. 1, p. 7267, 1989.

127. E. Possenriede, P. Jacobs, and O. F. Schirmer, "Paramagnetic defects in $BaTiO_3$ and their role in light-induced charge transport: I. ESR studies," *Journal of Physics: Condensed Matter*, vol. 4, p. 4719, 1992.

128. T. A. Keiderling, P. J. Stephens, S. B. Piepho, J. L. Slater, and P. N. Schatz, "Infrared absorption and magnetic circular dichroism of Cs_2ZrCl_6:Ir^{4+}," *Chemical Physics*, vol. 11, p. 343, 1975.

129. G. C. Allen, R. Al-Mobarak, G. A. M. El-Sharkawy, and K. D. Warren, "The electronic spectra of the hexahalo anions of osmium(IV) and iridium(IV)," *Inorganic Chemistry*, vol. 11, p. 787, 1972.

130. W. B. Fowler, *Electronic states and optical transitions of color centers: Physics of Color Centers*. Academic Press, 1968.

131. I. Bhaumik, R. Bhatt, S. Ganesamoorthy, A. Saxena, A. K. Karnal, P. K. Gupta, A. K. Sinha, and S. K. Deb, "Temperature-dependent index of refraction of monoclinic Ga_2O_3 single crystal," *Applied Optics*, vol. 50, p. 6006, 2011.

132. K. Saito, Y. Eishiro, Y. Nakao, H. Sato, and S. Sakaki, "Oscillator strength of symmetry forbidden $d - d$ absorption of octahedral transition metal complex: theoretical evaluation," *Inorganic Chemistry*, vol. 51, p. 2785, 2012.

133. S. J. Pearton, F. Ren, M. Tadjer, and J. Kim, "Perspective: Ga_2O_3 for ultra-high power rectifiers and MOSFETS," *Journal of Applied Physics*, vol. 124, no. 220901, 2018.

134. M. Higashiwaki and G. H. Jessen, "Guest Editorial: The dawn of gallium oxide microelectronics," *Applied Physics Letters*, vol. 112, no. 060401, 2018.

135. Z. Liu, P. G. Li, Y. S. Zhi, X. L. Wang, X. L. Chu, and W. H. Tang, "Review of gallium oxide based eld-effect transistors and Schottky barrier diodes," *Chinese Physics B*, vol. 28, no. 017105, 2019.

136. Y. Qin, H. Long, S. andDong, Q. He, G. Jian, Y. Zhang, P. Hou, X. andTan, Z. Zhang, Z. Lv, Q. Liu, and M. Liu, "Review of deep ultraviolet photodetector based on gallium oxide," *Chinese Physics B*, vol. 28, no. 018501, 2019.

137. X. H. Chen, F. F. Ren, S. L. Gu, and J. D. Ye, "Review of gallium-oxide-based solar-blind ultraviolet photodetectors," *Photonics Research*, vol. 7, p. 381, 2019.

138. M. J. Tadjer, J. L. Lyons, N. Nepal, J. A. Freitas, and G. M. Koehler, A. D. andFoster, "Review-Theory and Characterization of Doping and Defects in β-Ga_2O_3 ," *ECS Journal of Solid State Science and Technology*, vol. 8, p. Q3187, 2019.

139. R. Buscher and G. Lehman, "Correlation of zero-field splittings and site distortions. IX. Fe^{3+} and Cr^{3+} in β-Ga_2O_3 ," *Zeitschrift fr Naturforschung A*, vol. 42a, p. 67, 1987.

140. E. Farzana, M. F. Chaiken, T. E. Blue, A. R. Arehart, and S. A. Ringel, "Impact of deep level defects induced by high energy neutron irradiation in β-Ga_2O_3 ," *Applied Physics Letters Materials A*, vol. 7, no. 022502, 2019.

141. C. G. Walsh, J. F. Donegan, T. J. Glynn, G. P. Morgan, and G. F. Imbusch, "Luminescence from β-Ga_2O_3:Cr^{3+}," *Journal of Luminescence*, vol. 40 and 41, p. 103, 1988.

142. M. L. Meilman and G. I. A., "Low symmetry effects in EPR spectra," *Soviet Physics - Solid State*, vol. 11, no. 3, pp. 628–630, 1969.

143. A. Y. Polyakov, N. B. Smirnov, I. V. Schemerov, A. V. Chernykh, E. B. Yakimov, A. I. Kochkova, A. N. Tereshchenko, and S. J. Pearton, "Electrical properties, deep levels, and luminescence related to Fe in bulk semi-insulating β-Ga_2O_3 with Fe," *ECS Journal of Solid State Science and Technology*, vol. 8, p. Q3091, 2019.

144. E. M. Golden, S. A. Basun, D. R. Evans, A. A. Grabar, I. M. Stoika, and N. C. Giles, "Sn vacancies in photorefractive $Sn_2P_2S_6$ crystals: An electron paramagnetic resonance study of an optically active hole trap," *Journal of Applied Physics*, vol. 120, no. 133101, 2016.

145. A. R. Peaker, V. P. Markevich, and J. Coutinho, "Tutorial: Junction spectroscopy techniques and deep-level defects in semiconductors," *Journal of Applied Physics*, vol. 123, no. 161559, 2018.

146. D. Wickramaratne, C. E. Dreyer, B. Monserrat, J. X. Shen, J. L. Lyons, A. Alkauskas, and C. G. Van de Walle, "Defect identification based on first-principles calculations for deep level transient spectroscopy," *Journal of Applied Physics*, vol. 113, no. 192106, 2018.

147. K. W. H. Stevens, "Matrix elements and operator equivalents connected with the magnetic properties of rare earth ions," *Proceedings of the Physical Society - Section A*, vol. 65, pp. 209–215, 1952.

148. R. Orbach, "Spin-lattice relaxation in rare earth salts," *Proceedings of the Royal Society of London. Series A, Mathematical and Physical Sciences*, vol. 264, no. 1319, pp. 458–484, 1961.

149. S. K. Misra and C. Rudowicz, "Effect of monoclinic symmetry on the EPR spectra of Gd^{3+} -doped hydrated single crystals of rare-earth tricholorates," *Physica Status Solidi B*, vol. 147, pp. 677–684, 1988.

150. T. H. Yeom, C. Rudowicz, S. H. Choh, and D. G. McGavin, "Monoclinic spin Hamiltonian analysis of EPR spectra of Mn^{2+} in $BiVO_4$ single crystals," *Physica Status Solidi B*, vol. 198, pp. 839–851, 1996.

151. C. Rudowicz, "Relations between arbitrary symmetry spin-hamiltonian parameters B_k^q and b_k^q in various axis systems," *Journal of Magnetic Resonance*, vol. 63, 1984.

152. ——, "On standardization and algebraic symmetry of the ligand field Hamiltonian for rare earth ions at monoclinic symmetry sites," *Journal of Chemical Physics*, vol. 84, no. 9, pp. 5045–5058, 1986.

153. D. G. McGavin, "Symmetry constraints on EPR spin-Hamiltonian parameters," *Journal of Magnetic Resonance*, vol. 74, pp. 19–55, 1987.

154. I. G. Kim, T. Yeom, S. Lee, Y. M. Lee, H. W. Shin, and S. H. Choh, "Electron paramagnetic resonance studies of Mn^{2+} ions in β-Ga_2O_3 single crystal," *Journal of Applied Physics*, vol. 89, no. 5, pp. 4470–4475, 2001.

REPORT DOCUMENTATION PAGE

Form Approved
OMB No. 0704-0188

1. REPORT DATE *(DD-MM-YYYY)*	2. REPORT TYPE	3. DATES COVERED *(From - To)*
14-08-2019	PhD Dissertation	1 Sep 2016 - 13 Sep 2019

4. TITLE AND SUBTITLE
Point Defects in Lithium Gallate and Gallium Oxide

5a. CONTRACT NUMBER

5b. GRANT NUMBER

5c. PROGRAM ELEMENT NUMBER

6. AUTHOR(S)
Lenyk, Christopher A., Lt Col

5d. PROJECT NUMBER

5e. TASK NUMBER

5f. WORK UNIT NUMBER

7. PERFORMING ORGANIZATION NAME(S) AND ADDRESS(ES)
Air Force Institute of Technology
Graduate School of Engineering and Management (AFIT/EN)
2950 Hobson Way
Wright-Patterson AFB OH 45433-7765

8. PERFORMING ORGANIZATION REPORT NUMBER
AFIT-ENP-DS-19-S-023

9. SPONSORING/MONITORING AGENCY NAME(S) AND ADDRESS(ES)
Air Force Institute of Technology
Graduate School of Engineering and Management (AFIT/EN)
2950 Hobson Way
Wright-Patterson AFB OH 45433-7765

10. SPONSOR/MONITOR'S ACRONYM(S)
AFIT

11. SPONSOR/MONITOR'S REPORT NUMBER(S)

12. DISTRIBUTION/AVAILABILITY STATEMENT
Approved for Public Release. Distribution Unlimited

13. SUPPLEMENTARY NOTES
This material is declared work of the U.S. Government and is not subject to copyright protection in the United States.

14. ABSTRACT

Electron paramagnetic resonance (EPR), Fourier-Transform Infrared spectroscopy (FTIR), photoluminescence (PL), thermoluminescence (TL), and wavelength-dependent TL are used to identify and characterize point defects in lithium gallate and Ga2O3 doped with Mg and Fe acceptor impurities single crystals. EPR investigations of LiGaO2 identify fundamental intrinsic cation defects lithium and gallium vacancies. The defects' principle g values are found through angular dependence studies and atomic-scale models for these new defects are proposed. Thermoluminescence measurements estimate the activation energy of lithium vacancies at E_a = 1.05 eV and gallium vacancies at E_a > 2 eV below the conduction band minimum.
Mg and Fe doped Ga2O3 crystals are investigated with EPR and FTIR and concentrations of Ir^4+ ions greater than 10^{18} cm^3 are observed. The source of the unintentional deep iridium donors is the crucible used to grow the crystal. In the Mg-doped crystals, the Ir^4+ ions provide compensation for the singly ionized Mg acceptors contributing to the difficulties in producing p-type behavior in bulk single crystals. A large spin-orbit coupling causes Ir^4+ ions to have a low-spin (5d^5, S=1/2) ground state. The

15. SUBJECT TERMS
Point defects, electron paramagnetic resonance, lithium gallate, gallium oxide, FTIR, photoluminescence, thermoluminescence, isothermal decay, wide bandgap oxides, crystal field theory, activation energy^

16. SECURITY CLASSIFICATION OF:			17. LIMITATION OF ABSTRACT	18. NUMBER OF PAGES	19a. NAME OF RESPONSIBLE PERSON
a. REPORT	b. ABSTRACT	c. THIS PAGE			Dr. Nancy C. Giles, AFIT/EN
U	U	U	UU	163	19b. TELEPHONE NUMBER *(Include area code)* (937) 255-3636 x4601 nancy.giles@afit.edu

Reset

Standard Form 298 (Rev. 8/98)
Prescribed by ANSI Std. Z39.18

INSTRUCTIONS FOR COMPLETING SF 298

1. REPORT DATE. Full publication date, including day, month, if available. Must cite at least the year and be Year 2000 compliant, e.g. 30-06-1998; xx-06-1998; xx-xx-1998.

2. REPORT TYPE. State the type of report, such as final, technical, interim, memorandum, master's thesis, progress, quarterly, research, special, group study, etc.

3. DATES COVERED. Indicate the time during which the work was performed and the report was written, e.g., Jun 1997 - Jun 1998; 1-10 Jun 1996; May - Nov 1998; Nov 1998.

4. TITLE. Enter title and subtitle with volume number and part number, if applicable. On classified documents, enter the title classification in parentheses.

5a. CONTRACT NUMBER. Enter all contract numbers as they appear in the report, e.g. F33615-86-C-5169.

5b. GRANT NUMBER. Enter all grant numbers as they appear in the report, e.g. AFOSR-82-1234.

5c. PROGRAM ELEMENT NUMBER. Enter all program element numbers as they appear in the report, e.g. 61101A.

5d. PROJECT NUMBER. Enter all project numbers as they appear in the report, e.g. 1F665702D1257; ILIR.

5e. TASK NUMBER. Enter all task numbers as they appear in the report, e.g. 05; RF0330201; T4112.

5f. WORK UNIT NUMBER. Enter all work unit numbers as they appear in the report, e.g. 001; AFAPL30480105.

6. AUTHOR(S). Enter name(s) of person(s) responsible for writing the report, performing the research, or credited with the content of the report. The form of entry is the last name, first name, middle initial, and additional qualifiers separated by commas, e.g. Smith, Richard, J, Jr.

7. PERFORMING ORGANIZATION NAME(S) AND ADDRESS(ES). Self-explanatory.

8. PERFORMING ORGANIZATION REPORT NUMBER. Enter all unique alphanumeric report numbers assigned by the performing organization, e.g. BRL-1234; AFWL-TR-85-4017-Vol-21-PT-2.

9. SPONSORING/MONITORING AGENCY NAME(S) AND ADDRESS(ES). Enter the name and address of the organization(s) financially responsible for and monitoring the work.

10. SPONSOR/MONITOR'S ACRONYM(S). Enter, if available, e.g. BRL, ARDEC, NADC.

11. SPONSOR/MONITOR'S REPORT NUMBER(S). Enter report number as assigned by the sponsoring/ monitoring agency, if available, e.g. BRL-TR-829; -215.

12. DISTRIBUTION/AVAILABILITY STATEMENT. Use agency-mandated availability statements to indicate the public availability or distribution limitations of the report. If additional limitations/ restrictions or special markings are indicated, follow agency authorization procedures, e.g. RD/FRD, PROPIN, ITAR, etc. Include copyright information.

13. SUPPLEMENTARY NOTES. Enter information not included elsewhere such as: prepared in cooperation with; translation of; report supersedes; old edition number, etc.

14. ABSTRACT. A brief (approximately 200 words) factual summary of the most significant information.

15. SUBJECT TERMS. Key words or phrases identifying major concepts in the report.

16. SECURITY CLASSIFICATION. Enter security classification in accordance with security classification regulations, e.g. U, C, S, etc. If this form contains classified information, stamp classification level on the top and bottom of this page.

17. LIMITATION OF ABSTRACT. This block must be completed to assign a distribution limitation to the abstract. Enter UU (Unclassified Unlimited) or SAR (Same as Report). An entry in this block is necessary if the abstract is to be limited.